Distribution Agreement

In presenting this thesis or dissertation as a partial fulfillment of the requirements for an advanced degree from Emory University, I hereby grant to Emory University and its agents the non-exclusive license to archive, make accessible, and display my thesis or dissertation in whole or in part in all forms of media, now or hereafter known, including display on the world wide web. I understand that I may select some access restrictions as part of the online submission of this thesis or dissertation. I retain all ownership rights to the copyright of the thesis or dissertation. I also retain the right to use in future works (such as articles or books) all or part of this thesis or dissertation.

Signature:

_____ _____

Luka Matej Đevenica Date

Strongly-interacting Excitonic Phases in van der Waals Heterostructures of Two Dimensional Semiconductors

By

Luka Matej Đevenica
Doctor of Philosophy

Physics

Ajit Srivastava, Associate Professor
Advisor

Hayk Harutyunyan, Associate Professor
Committee Member

Connie Roth, Professor
Committee Member

Luiz Santos, Assistant Professor
Committee Member

Carlos Sa de Melo, Professor
Committee Member

Accepted:

Kimberly Jacob Arriola, Ph.D.
Dean of the James T. Laney School of Graduate Studies

Date

Strongly-interacting Excitonic Phases in van der Waals Heterostructures of Two Dimensional Semiconductors

By

Luka Matej Đevenica
B.A., Amherst College, MA, 2017

Advisor: Ajit Srivastava, Associate Professor

An abstract of
A dissertation submitted to the Faculty of the
James T. Laney School of Graduate Studies of Emory University
in partial fulfillment of the requirements for the degree of
Doctor of Philosophy
in Physics
2025

Abstract

Strongly-interacting Excitonic Phases in van der Waals Heterostructures of Two Dimensional Semiconductors
By Luka Matej Đevenica

Phenomena of spontaneous collective arrangement of strongly-interacting quantum particles have long been a fascinating area of physics, and have allowed us to understand many spectacular natural phenomena, ranging from fractionalization of charge and topological order to high-temperature superconductivity. Two-dimensional materials have emerged as a powerful new platform for the study of strongly-correlated physics, as the reduced dimensionality enhances particle interactions relative to their kinetic energy. Within these, Transition-Metal Dichalcogenide (TMD) monolayers are premier semiconductors, especially in the context of optics, since they couple strongly to light. In this dissertation, we use this property to optically generate large populations of excitons, quasiparticles that are the low-energy excitation of semiconductors, formed when an electron is excited and bound to the hole it leaves behind. We then study the possible many-body phases of interacting excitons, as they interact strongly via their dipolar moment and through exchange interactions.

The samples we study are heterostructures of TMD monolayers, made of different TMD species. We observe three distinct excitonic phases in TMD heterobilayers: an excitonic Mott insulator, a mixed electron-exciton Mott insulator and an in-plane excitonic ferroelectric phase, and in heterotrilayers we observe a novel quasiparticle, the out-of-plane quadrupolar exciton, with tantalizing signatures that they exhibit out-of-plane antiferroelectric correlations at high densities. The phases are identified through optical spectroscopy, emphasizing the power of relatively simple techniques in identifying microscopic details of the systems under study, due to the TMDs' excellent optical properties. We observe unusual collective emission from moiré excitons which is dependent on the stacking configuration between the monolayers. We also showcase the remarkable tunability of these systems, with integrated electric field and doping control. This work underscores the potential of the 2D platform in further advancing our understanding of strongly-correlated physics, particularly in a driven-dissipative system, and the significant role of TMDs and optics in the discovery and characterization of moiré quantum materials.

Strongly-interacting Excitonic Phases in van der Waals Heterostructures of Two Dimensional Semiconductors

By

Luka Matej Đevenica
B.A., Amherst College, MA, 2017

Advisor: Ajit Srivastava, Associate Professor

A dissertation submitted to the Faculty of the
James T. Laney School of Graduate Studies of Emory University
in partial fulfillment of the requirements for the degree of
Doctor of Philosophy
in Physics
2025

Acknowledgments

There are many people who helped me in the completion of this thesis. I would like to sincerely thank all of them, as they also helped me become a better person along the way.

First, I would like to thank my doctoral adviser, Professor Ajit Srivastava, for his mentorship, patience, guidance and hard work in supporting me to complete my project. His tireless energy and genuine devotion to his craft was an inspiration, and the material and spiritual support he provided me was beyond the call of duty. He challenged me at every turn and pushed me to refine my thinking and improve as an experimentalist as well as in computational and modeling efforts. More than this, he lifted my spirits and made it clear how much he believed in my capacity to do good work when I had all but stopped believing in myself. His gift of time, energy and care is a precious one and I will strive to pass it forward.

Next, I would like to thank my colleagues from the Srivastava Lab at Emory Unversity. Postdocs Prof. Xin Lu and Prof. Sudipta Dubey and my labmates Xiaotong Chen, Neil Tramsen, Jiatian Wu, Runtong Li and Zach Hadjri were wonderful to work with and taught me many key skills in my PhD. I would especially like to thank Weijie Li, who was like a brother to me in the lab and whose dedication and hard work I greatly admire.

I would like to thank all those who helped me at Emory, starting with my committee members Prof. Hayk Harutyunyan, Prof. Luiz Santos, Prof. Connie Roth and Prof. Carlos sa de Melo of Georgia Institute of Technology, for their supervision and guidance. I thank Prof. Sergei Urazhdin for his generous sharing of fabrication tools and facilities he maintains with great effort, as well as Prof. Kurt Warncke for sharing electronic instrumentation crucial for our work.

I would also like to thank my colleagues from the University of Geneva, where part of this work was performed: postdocs Prof. Nicolas Ubrig, Valeria Vento, Bosai Lyu

and Daniel Suarez Forrero and my labmates Klevis Domi and Ludivine Fausten, for their hospitality and support. I would also like to thank Prof. Alberto Morpurgo and his group for sharing their facilities and providing generous training and resources.

I would like to thank our collaborators who provided support in theory and computation: Jin Zhang (Max Plank Institute), Prof. Angel Rubio (Max Plank Institute), Jan Kumlin (TU Wien) and Prof. Thomas Pohl (TU Wien). I would also like to thank our collaborators who provided high-quality sample materials: Song Liu (Columbia University), Prof. James Hone (Columbia University), Prof. Kenji Watanabe (NIMS) and Prof. Takashi Taniguchi (NIMS).

I would like to thank my friends, both near and far, who supported me. My fellow graduate students James Merrill, Sahand Emamian, Kavinda Nissanka, Satya Spandana, Sabid Hossain and Pablo Illing were also fantastic friends, who supported me and with whom I've shared very profound experiences. My friends Vladimir Mlinarević, Sergej Samardžić, Ilya Kiselev, Sophie Lichter, Ilija Nikolov, Stefan Marić, Marko Koprena and Jovan Damjanović were all half a world away, but helped me in many practical and emotional ways, and I am very grateful to have them. I would especially like to thank my girlfriend Hannah Gilbonio for her love, support and the ways she enriched my life and time as a PhD student.

Lastly, but certainly not least, I want to thank my family: my parents Biljana and Gorazd, my sisters Sonja and Martina and their husbands Dušan and Marcel, as well as my nephew Kosta and nieces Danica and Astrid, and my aunt Mirjana. Their love has carried me since the day I was born and it continues to do so today. It is to them that I dedicate this thesis.

Contents

List of Figures

List of Tables

Chapter 1

Introduction

Amid the countless technological revolutions humanity has enacted in the past century, the stunning advances in semiconductor technology stand out for their transformative effect on the world. As Moore's law, which so long set the pace of miniaturization of electronics, reaches its physical limitations, the emerging field of 2D materials pushes semiconductor geometries to their absolute extreme - the single atom limit. This thesis studies a class of semiconductors, called transition-metal dichalcogenides (TMDs), which can be made into atomically thin monolayers, and in this form stably integrated into complex devices. Their reduced dimensionality makes 2D systems an excellent platform for the study of strongly correlated systems, as the reduction in the degrees of freedom increases the potential/kinetic energy ratio and enables the creation of phases of matter that would be unstable otherwise. This has generated much excitement, and 2D materials, including TMDs, are at the forefront of the search for new physics in solid-state materials. They are also promising for technological applications, such as novel detectors or miniaturized light sources.

In the rapidly developing arena of 2D materials, TMD monolayers stand out for their many remarkable properties, including that they interact strongly with light, which enables optical control and detection of many interesting phases [1]. Recent

work in TMD monolayers has included the realization of a robust new electronic degree of freedom called the valley [2], exciton polaritons [3], a rich variety of charge density wave phases [4], as well as superconducting phases at a variety of critical temperatures using different TMD materials [5] and even metastable polytopes of TMDs [6]. The broad class of materials that can be exfoliated into the monolayer form are called van der Waals (vdW) materials, owing to the weak out-of-plane van der Waals interactions that enable thinning them down to single layers.

Going beyond individual monolayers, an exciting direction this field has taken is the construction of artificial multilayer structures by vertically stacking multiple layers of the same or different 2D materials. This enables the creation of structures, artificial van der Waals heterostructures, with remarkable novel properties not found in nature, which can be tuned by the precise details of the structure design. If the vdW heterostructures are assembled with a small twist between them, the resulting moiré superlattice can host 'flat' electronic bands with quenched kinetic energy, which leads to electron-electron interactions becoming the dominant energy scale and can give rise to strongly correlated electronic phases. A famous example is the observation of unconventional superconductivity in graphene bilayers that are twisted to the 'magic angle' of 1.1° [7]. Correlated states in TMD homobilayers (bilayers of the same material) have been found for a range of twist angles, dubbed the 'magic continuum' [8]. In addition to enhanced interactions, such artificial crystals can also host topologically non-trivial electronic bands. The interplay of strong correlations and topology gives rise to the recent observations of topologically nontrivial phases, namely Chern and fractional Chern insulators in twisted $MoTe_2$ [9, 10, 11], which are systems exhibiting the anomalous fractional quantum Hall effect, or the fractionalization of electron states in the absence of external magnetic fields.

As discussed in detail in later chapters, this moiré superlattice potential can be thought to emerge from an interference effect in interlayer tunneling behavior in

homobilayers. The large length scales ($\sim$ 1-10 nm) of the moiré potential relative to the lattice constants of these materials ($\sim$ 3-4 Å) means that high-lattice-filling regimes are achieved more readily with fewer added particles (charged or neutral), enabling exploration of previously difficult-to-access regimes of the Hubbard model. One example of this is the electronic Mott insulator, an insulating phase that arises due to particle repulsion and is intimately related to high-Tc superconductivity [12] and generalized Wigner crystals, which have been observed both in homo- and hetero-bilayers [13, 14, 15, 16, 17, 18].

Extending the study of strongly correlated states of electrons to an out-of-equilibrium setting, the question this thesis addresses is what kinds of new phases are possible in these systems of interacting charge carriers, but also interacting optically excited neutral quasiparticles, called excitons. Such states are naturally out-of-equilibrium and dissipative towards photon emission, which can be analyzed to glean information about the correlated dynamics. Excitons in 2D TMD heterostructures have been shown to strongly interact with each other, both via dipolar electrostatic Coulomb interactions and via exchange interactions [19, 20, 21, 22].

Our focus in this work are the phases of high-density excitons in structures made by combining different TMDs, where we demonstrate that excitons can form several exotic quantum phases. Firstly, we characterize an excitonic Mott insulator in a WSe_2/WS_2 heterobilayer, a excitonic version of the electron Mott insulator, generated by optical excitation. We also observe a mixed electron-exciton insulating phase in the same system upon doping the sample with electrons. Still in the same sample, we observe a spontaneously ordered ferroelectric phase of excitons at densities lower or near the Mott insulator, and which coexists with the Mott insulating state. We study this ordering by analyzing the decay dynamics of excitons which is found to arise from an unusual collective photon emission. Lastly, we present evidence for an anti-ferroelectric excitonic correlations in a $WS_2/WSe_2/WS_2$ trilayer sample, which

competes with the formation of a delocalized out-of-plane quadrupolar exciton state.

1.1 Thesis Outline

In Chapter 2, we will introduce the crystallographic, electronic and optical properties of TMDs and their monolayers. Next, we will turn to their heterostructures, structures made from more than one monolayer of different kinds, and elaborate on the fundamentals of their rich optical physics.

In Chapter 3, we will explain the fabrication methods we used to create TMD heterostructures encapsulated by hBN and with graphene gating. Our setup is entirely home-made and has been successful in creating high-quality samples, integrating a fully mechanized polymer-based dry pickup procedure with temperature and atmosphere control, as well as necessary vibration isolation for handling these delicate samples.

In Chapter 4, we will describe the optical methods we used to measure our samples and detect the electronic and excitonic phases featured in this work, as well as the custom apparatus for integrating the optics into a cryogenic setup and measuring time-resolved photoluminescence with $\sim$ ns precision.

In Chapter 5, we present our results on the excitonic Mott insulator and the mixed Bose-Fermi crystal of excitons and electrons in moiré superlattices. We observe a sizable ($\sim$ 40 mev) excitonic Mott gap and find that the coexistence of the excitons and electrons can be used to realize field-configurable mixed electron-exciton crystals.

In Chapter 6, we investigate an excitonic in-plane ferroelectric phase in semiconductor heterobilayers and its effect on the light-matter coupling strength of the excitons. Excitons in a heterobilayer with a particular twist angle are found to be able to acquire a finite in-plane dipole moment, which facilitates a $\sim$ 15 meV attractive stabilization of a in-plane ferroelectric excitonic phase, which is marked by a slower

exciton decay rate.

In Chapter 7, we showcase our finding of a novel excitonic species, the out-of-plane quadrupolar exciton, and evidence that quadrupolar excitons can form an excitonic out-of-plane antiferroelectric phase at sufficiently high densities. The quadrupolar exciton features a field-tunable lifetime and, at high densities, we observe signatures of antiferroelectric correlations driven by reduction in exchange repulsion and dipolar attraction.

Chapter 2

Background

2.1 Transition Metal Dichalcogenide Monolayers

A natural place to begin our discussion is an introduction to the main material platform studied in this dissertation - Transition-Metal Dichalcogenides (TMDs) and their atomically-thin monolayers. The first-ever TMD structure to be characterized by X-ray crystallography was that of MoS_2, by none other than Linus Pauling in 1923 [23]. In modern condensed-matter physics they have taken the stage as premier 2D semiconductor materials, largely due to being van-der-Waals materials. A van-der-Waals (vdW) material is characterized by strong in-plane covalent forces holding the constituent atoms together, while the material is held by much weaker van-der-Waals forces in the out-of-plane direction. Therefore, bulk van-der-Waals materials consist of many planar layers stacked on top of one another, with a clear 'weak' axis along which the material can be easily cleaved, separating two adjacent planes. In 2005, Novoselov and Geim exploited this property to bring about 2D materials - the ultimate limit of the cleaving approach which leaves behind macroscopically large individual crystal planes [24]. Before this work, the feasibility of free-standing monolayers was unclear, as their theromodynamic stability and macroscopic conti-

nuity was in question. Thankfully, monolayers of all kinds are remarkably stable in ambient conditions: efficient conductors like graphene, strong insulators like hexagonal boron nitride (hBN) and the materials of most interest here - the semiconducting TMDs.

2.1.1 Crystallographic Properties of TMD Monolayers

TMD monolayers are structurally like planar sandwiches, with an X-M-X structure, where X stands for the chalcogen and M for the transition metal (Fig 2.1a). Within the X-M-X sandwich, the X atom sheets and the M atom sheets both form a hexagonal lattice when considered separately, and the various polytopes of TMDs come about from different relative arrangements of these two sub-lattices [25]. There are many different possible combinations of X and M materials, with over 40 known layered TMDs with widely varying properties - some metals, some insulators and some semiconductors [26, 27]. The subset of TMDs we study here are the group VI TMDs: they have M = Mo or W and X = S or Se, and are all semiconductors with band gaps on the order of 1.5-2 eV. These materials are favorable to work with, as they are stable against oxidation in ambient conditions [28]. They also all share the trigonal prismatic (2H) phase as the most common and stable polytope. All future references to TMDs in this work will refer exclusively to these four materials.

Figure 1.1 shows a structure of a typical 2H TMD monolayer. Panel 2.1a shows a side view of the monolayer, and the X-M-X sandwich. Note that the distances from an M atom to the neighboring X are asymmetrical, with a clear short and long M-X bond. This feature is clarified by observing panel 2.1b, where we see that the structure is a honeycomb lattice. In fact, each M site has 3 neighboring X sites, which form vertices of an equilateral triangle, of which M is the center. The chalcogen atoms of a single layer in the 2H phase are horizontally aligned, so we can view them as a single X site. An important aspect of all crystal structures are their symmetries.

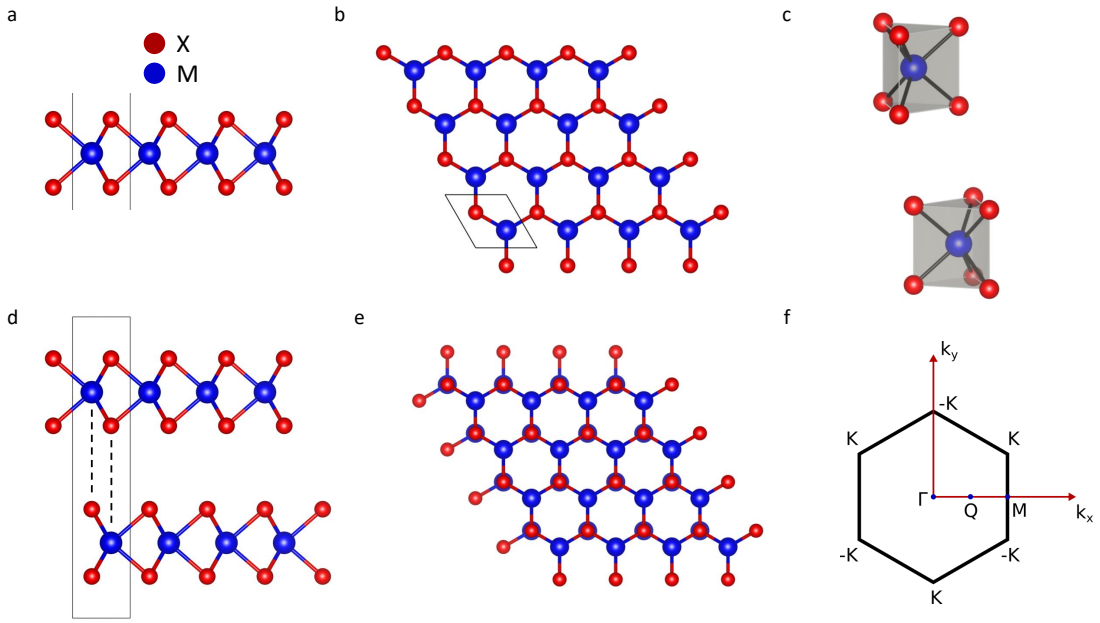

Figure 2.1: Crystallographic Properties of 2H TMD Monolayers. Example used is WSe_2. Lattice constants obtained from [29]. **a.** Side view of a TMD monolayer. Blue atoms indicate the transition metals M, and red atoms indicate the chalcogens X. The black lines indicate the edge of a unit cell. **b.** Top-down view of a TMD monolayer. Black diamond indicates the edges of the unit cell. **c.** Isometric projections of a TMD unit cell, front and back views. **d.** Side view of a Bernal (180°) stacked TMD bilayer. Black rectangle indicates unit cell edges. Dashed lines indicate atomic alignment. **e.** Top-down view of a Bernal (180°) stacked TMD bilayer. Note the alignment of X and M atoms from different layers. **f.** First Brillouin zone of a TMD monolayer, with standard high-symmetry points indicated.

The 2H TMD monolayers belong to the D_{3h} symmetry point group [30]. In the out-of-plane direction, the monolayers have a mirror symmetry about the central plane, which cuts the metal atoms (Figure 2.1a). The monolayers also have a 3-fold (120°) in-plane rotation symmetry about any axis going through an X, M or hexagonal center point h (Figure 2.1b). Importantly, the monolayers have no center of inversion symmetry, as inverting the lattice about the hexagonal center point projects an X site to an M site, and vice versa. Each monolayer is about 0.7 nm thick, and the four materials of interest ($MoSe_2$, MoS_2, WSe_2 and WS_2) have very similar lattice parameters, a selection of which is shown in Table 2.1 [29].

Table 2.1: Select TMD lattice parameters.

Material	Lattice Constant (nm)	M-X in-plane bond angle (rad)
MoS_2	0.3166	0.710
$MoSe_2$	0.3288	0.710
WS_2	0.3153	0.710
WSe_2	0.3282	0.710

In bulk form, TMDs consist of many monolayers stacked in the out-of-plane direction. The most stable stacking order, which characterizes the 2H phase, is called AB, H-stacking or sometimes Bernal stacking. Figure 2.1d shows a side view of an AB stacked bilayer. The name 'AB' comes from the fact that the two monolayers are facing opposite directions, which facilitates the horizontal alignment of X and M sites across the two layers. The planar view (Fig 2.1e) shows that this arrangement is equivalent to the top monolayer being a 180° (or, equivalently, 60°) rotated copy of the bottom, displaced such that the X and M sites of different layers align. This affects the symmetry of the structure, and the point group of the bilayer is D_{3d} [31]. This means that AB stacked bilayers still feature the in-plane three-fold rotation symmetry, but the out-of-plane mirror-symmetry is now broken, whereas the inversion symmetry is restored, with the inversion centers at the midpoint between the two

layers.

TMD monolayers' broken inversion symmetry, which stems from the two inequivalent M and X sites in the lattice, is also present in the reciprocal space of the monolayer lattice (Fig 2.1f). The vertices of the first Brillouin zone of the TMD monolayer are high-symmetry points, which we label as K or $-K$. Since electrons in solids obey Bloch's theorem, each electronic eigenstate in a TMD monolayer is associated with a $\vec{k}$ inside the Brillouin zone, and the crystal momentum of that eigenstate is given by $p_q = \hbar\vec{k}$. Therefore, we observe that K and $-K$ points, being related by an inversion of the velocity, correspond to states with equal and opposite momenta, or states that are related by time-reversal. The inequivalency of these Brillouin zone corners at K and $-K$ stems from the broken spatial inversion symmetry of the crystal, and is a very important feature with profound implications on the electronic structure of these materials.

2.1.2 Electronic Properties of TMD Monolayers

When discussing the electronic properties of any material, we begin with its band structure. The most powerful current methods for theoretical ab-initio determination of band structures of solids are those of density functional theory (DFT). In these approaches, well known potentials of individual atoms are mapped onto the crystallographic structure of the solid in a finite-size cell with periodic boundary conditions, and the allowed electronic states are solved for in a plane-wave basis [32]. These methods have been greatly successful, and for TMD monolayers DFT results align well with results from current gold-standard experimental method for measuring band structures, called ARPES (angle-resolved photoemission spectroscopy) [33]. The DFT approach is, however, computationally expensive, and its results are commonly mapped onto a simpler tight-binding (TB) model. In the tight-binding approach, a number of relevant atomic orbitals (typically the valence orbitals of the atoms) from

the constituent atoms are selected, and a Hamiltonian is constructed which contains so-called hopping terms, which quantify the coupling between the atomic orbitals on different sites. This Hamiltonian is typically found by fitting to already known DFT values. Such an approach was recently done by Dias et al. [34], and we will use the tight-binding values in their model for our analysis here.

In this TB model, Dias et al. consider the contribution of 11 atomic orbitals - 5 d valence orbitals of the transition metal, and 3 p valence orbitals each from the two chalcogen atoms in the unit cell. The p orbitals of the chalcogens are expressed as symmetric and antisymmetric combinations of the top and bottom chalcogen sites, which together with the d orbitals separates the basis into even and odd functions under a mirror-symmetry transformation about the metal plane of the monolayer. We load the parameters defining the hopping between each pair of these bands from the spinless model of [34], using them to construct an 11-dimensional Hamiltonian. The bands are then obtained by diagonalizing this Hamiltonian over the range of crystal momenta in the first Brillouin zone, on all points of a discretized lattice with some finite resolution Δk. For now, we disregard the spin-orbit coupling, and show the bands as spin-degenerate. The bands are typically displayed along a 1D path through the high-symmetry points in the Brillouin zone for clarity (Fig 2.2a). We see that there is a direct band gap at the K point, meaning that the lowest energy conduction band state and the highest energy valence band state have the same crystal momenta, which results in them being 'on top' of each other in the band structure. This direct band gap is a key feature, which will define much of the optical properties of the TMD monolayer.

Figure 2.2b shows the full 2D extent of the valence and conduction bands. The direct band gap is present both at the K and $-K$ points, as the valence and conduction bands are evenly symmetric. Looking more closely at the solved bands near the K and -K points, the valence band is predominantly composed of the d_{xy} and $d_{x^2-y^2}$

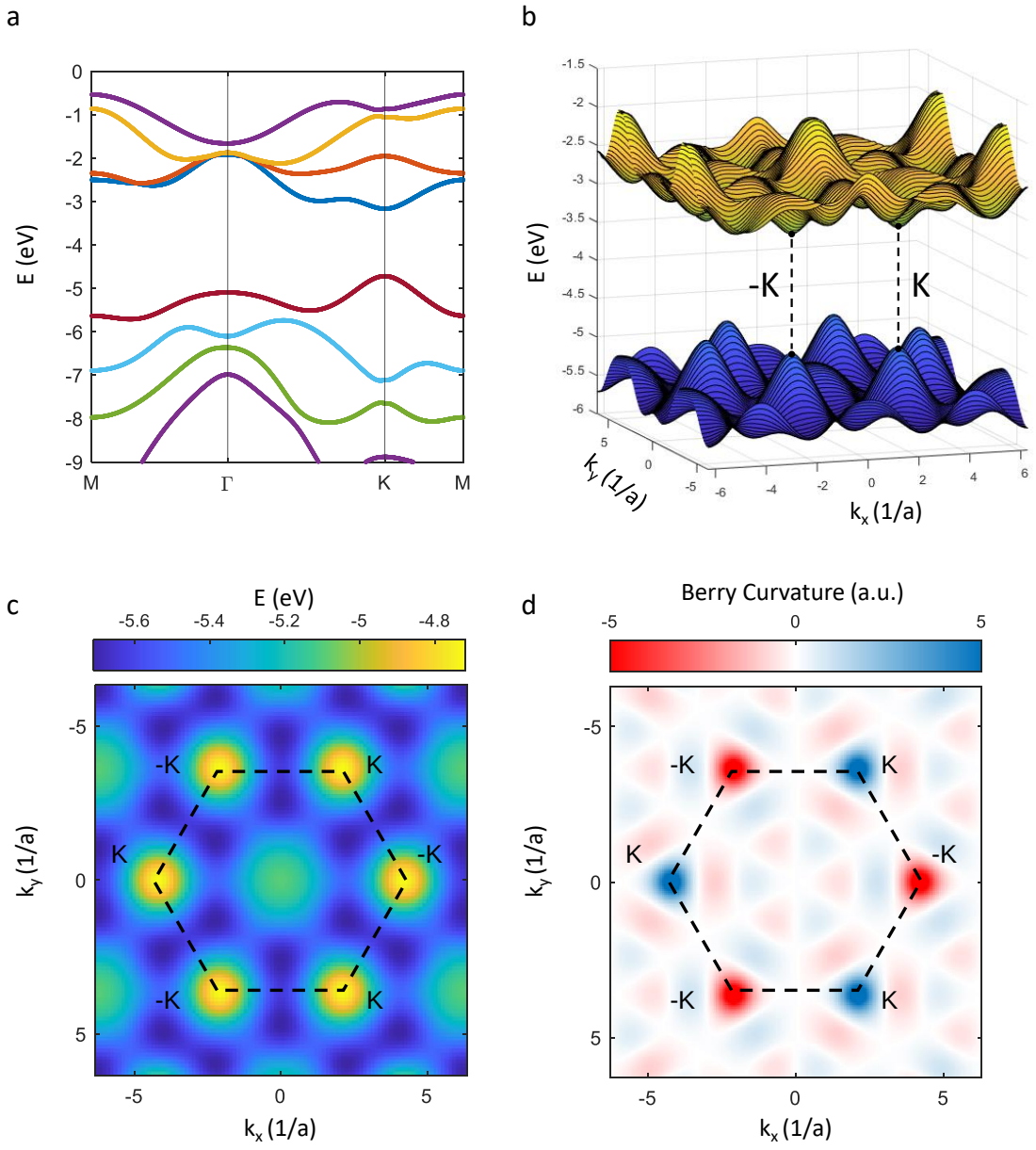

Figure 2.2: Band structure of 2H TMD monolayers. The example used is monolayer WSe_2. Tight binding parameters obtained from [34]. **a.** Band structure of a WSe_2 monolayer. The dark red band is the valence band and the dark blue band is the conduction band. **b.** Full 2D representation of the valence and conduction band. The direct band gap at the K and -K points is indicated by the dashed lines. **c.** Colormap of the valence band. **d.** Berry curvature of the valence band.

bands of the metal, as well as a smaller contribution of the p_x and p_y bands of the chalcogen. The conduction band is predominantly composed of the d_{z^2} bands of the metal and a similar contribution of p_x and p_y bands of the chalcogen. Notably, both the valence and conduction bands are comprised only of basis functions that are even under mirror transformation about the metal plane.

Let us consider the valence band more closely (Figure 2.2c). If we consider the energy of the band alone, the band does not only have the 3-fold symmetry of the lattice structure, but has in fact a full hexagonal, 6-fold symmetry. A natural question is how this is possible, given that the reciprocal space symmetries ought to be preserved from the real space ones. In other words, what is it really that distinguishes the K point from $-K$? The key is in the fact that they are related through time reversal. In order to get at this aspect of the band, we study a quantity called Berry curvature.

Berry Curvature in Monolayer TMD Bands

When any quantum state is adiabatically evolved from some initial eigenstate of the system Hamiltonian H via a closed path back to the exact same state from which it started, the state at the end is identical to the starting one, but with an accumulated phase factor. The sign and magnitude of this phase by which the end state is offset from the initial one is a function of the exact path covered:

$$|\Psi_{end}\rangle = e^{i\gamma_B} |\Psi_{init}\rangle \tag{2.1}$$

This phase γ_B is known as a Berry phase, and it has emerged as a quantity of great interest in characterizing electronic states in solids, as its elaboration lead to breakthroughs in true quantum mechanical understanding of electric polarization and orbital magnetization, beyond the classical pictures of bound charges and currents [35].

Berry phase can be expressed as a line integral of a quantity A_B known as Berry connection:

$$\gamma_B = \oint A_B(\vec{R}) \cdot d\vec{R} \tag{2.2}$$

$$A_B(\vec{R}) = i \left\langle \Psi(\vec{R}) \middle| \frac{\partial}{\partial \vec{R}} \middle| \Psi(\vec{R}) \right\rangle \tag{2.3}$$

where $\vec{R}(t)$ is a set of time-dependent parameters which define the Hamiltonian $H(\vec{R})$ (in most condensed matter systems, since the states are typically expressed in the $\vec{k}$ basis, $\vec{R} = \vec{k}$). We see that Berry connection is essentially a local measure of the rate at which the state moves through the Hilbert space with respect to a change in the parameters $\vec{R}$. Using Stokes' theorem, we can rewrite the Berry phase as a surface integral of the curl of the Berry connection, which we call $\Omega(\vec{R})$:

$$\gamma_B = \int_S \Omega(\vec{R}) \cdot d\vec{S} \tag{2.4}$$

$$\Omega(\vec{R}) = \nabla \times A_B(\vec{R}) = i \left\langle \frac{\partial}{\partial \vec{R}} \Psi(\vec{R}) \middle| \times \middle| \frac{\partial}{\partial \vec{R}} \Psi(\vec{R}) \right\rangle \tag{2.5}$$

The quantity $\Omega(\vec{R})$ is also called Berry curvature, and represents the local Hilbert space geometry of a given band. Note that the entire discussion of Berry phase and curvature rests on the initial state being adiabatically changed by changing $\vec{R}$, but remaining in the same (smoothly connected) eigenstate. Therefore, the Berry curvature is only well-defined within a single band, not for states in superposition of different, non-degenerate bands. However, Berry curvature itself is intimately related to all the other bands, as it represents the sum of all projections to other eigenstates of the initial Hamiltonian that become mixed into the state as it evolves through the parameter space [36]. For this reason, the sum of the Berry curvature of all bands in a system at any point $\vec{R}$ is 0, which is known as the law of conservation of Berry curvature.

A convenient way to numerically calculate the Berry curvature from the model we

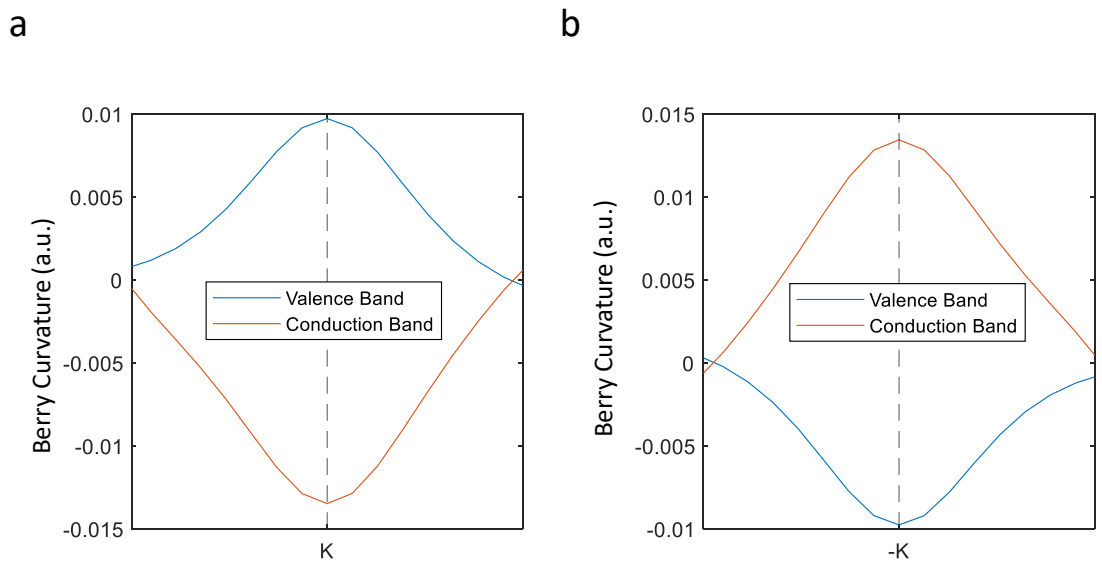

Figure 2.3: Berry Curvature of WSe_2 at K and -K Valleys. **a.** Berry curvature of the valence and conduction bands at the K point. **b.** Berry curvature of the valence and conduction bands at the -K point.

described earlier was developed by Fukui et al. [37]. The salient feature of the technique is that it allows a direct calculation of the Berry curvature, a gauge invariant quantity (unlike the Berry connection), on a discretized lattice. Figure 2.2d shows the resulting calculation. As we can see, the K and $-K$ points are now clearly distinguished by having equal in magnitude, but opposite in sign, local Berry curvature. One striking result related to Berry curvature is that it acts as an intrinsic magnetic field in that it induces a transverse Hall current in the absence of external magnetic fields [38]. Since in TMD materials, the Berry curvature is a function of the valley, this phenomenon is called the valley Hall effect [39, 40, 41]. Another interesting feature our calculation demonstrates is that the Berry curvature has similar intensity but opposite sign at the valence and conduction bands, in accordance with literature results [42] (Figure 2.3).

The presence of finite Berry curvature also implies finite spin-orbit coupling near the K and $-K$ points [35]. In fact, the model of Dias et al. [34] accounts for this

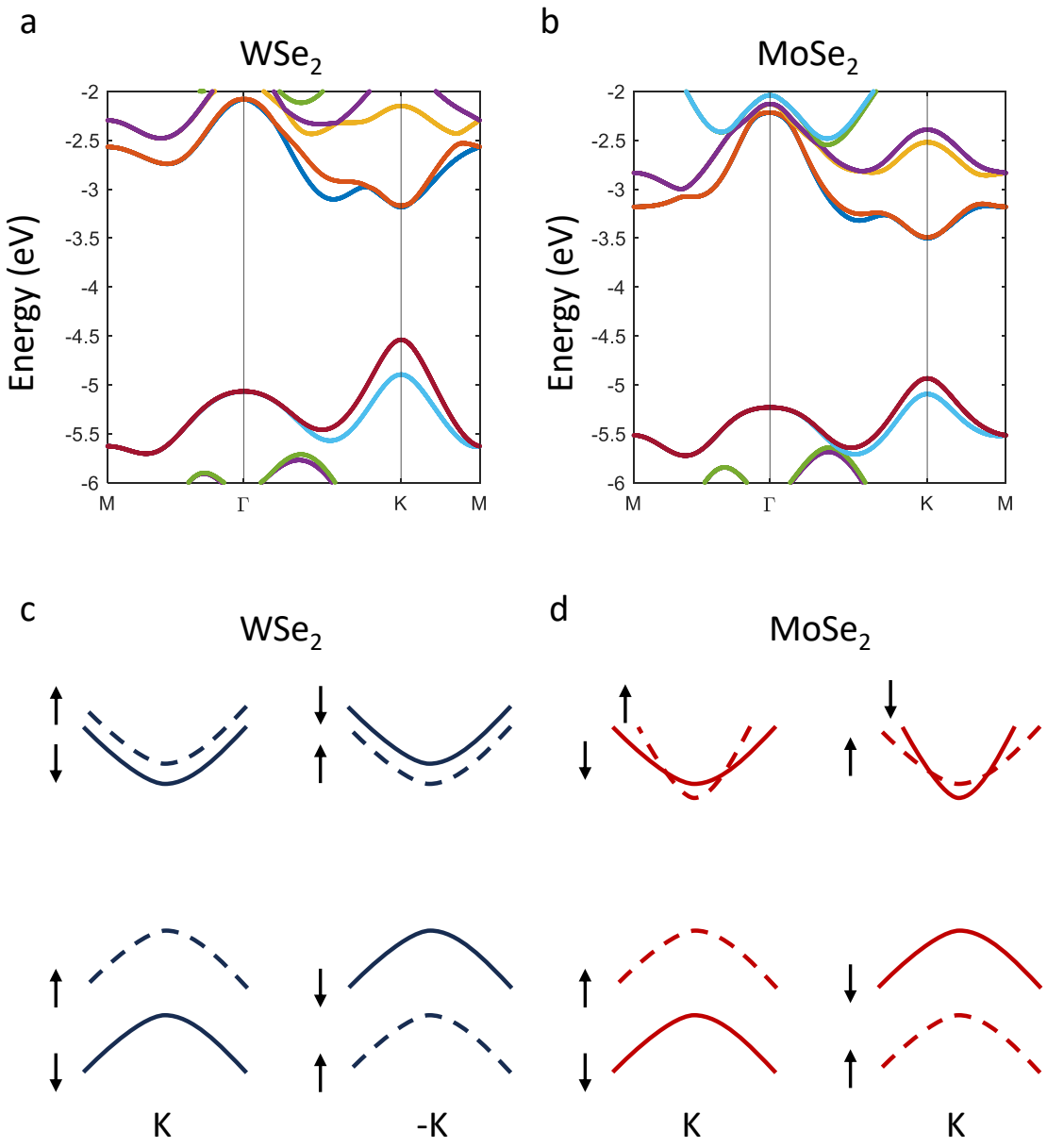

Figure 2.4: Spin-split band structure of 2H TMD Monolayers. Tight binding parameters obtained from [34]. **a.** Band structure of a WSe_2 monolayer with spin-orbit coupling. **b.** Spin-split band structure of a $MoSe_2$ monolayer. **c.** Schematic of the spin-split bands in WSe_2 at the K and -K points. Not to scale. **d.** Schematic of the spin-split bands in $MoSe_2$ at the K and -K points. Not to scale.

as well, and we can use their parameters to investigate the spin-split bands of the monolayer TMDs. Figure 2.4a,b shows the bands with spin-orbit coupling for WSe_2 and $MoSe_2$. We observe that, near the K points, the magnitude of the splitting is much higher for the valence band than for the conduction band, stemming from the different d orbital contributions to the respective bands discussed earlier [40]. Figure 2.4c,d shows a diagrammatic representation of the bands at K and $-K$ points. We see that, as demanded by their time-reversal relationship, the K and $-K$ points have opposite spin-splittings. Interestingly, W-based TMDs and Mo-based TMDs have a slight difference in the nearly-degenerate conduction band, in that the relative order of the spin energies in reversed. For example, in WSe_2, the lowest energy conduction state has an opposite spin to the highest energy valence state in both valleys, whereas in $MoSe_2$ the same pair of states have the same spin.

Lastly, let us comment on the orbital magnetic moment (OAM) of the valence and conduction bands. Since the system is 2D, the only possible magnetic moment is in the z direction. The first contribution to the OAM of the bands comes from the the atomic magnetic moment inherited from the constituent tight-binding orbitals m_α. In order to account for this, we can, to a first approximation, express the valence and conduction bands via their dominant orbital contributions:

$$|\psi_c\rangle = \left|d_z^2\right\rangle \tag{2.6}$$

$$|\psi_v^\tau\rangle = \frac{1}{\sqrt{2}}(|d_{x^2-y^2} + i\tau\,|d_{xy}\rangle\rangle \tag{2.7}$$

where τ is the valley index ($\tau = 1$ for K and $\tau =$ -1 for $-K$). The phase relationship between the d bands in the valence band is derived from the D_{3h} point group symmetry considerations [43]. For the conduction band, m_α is $\sim$0, as the d_z orbital carries no z magnetic moment. For the valence band, m_α is 2τ, since the different linear combinations of the two bands lead to different OAM contributions. This larger

valence OAM band contribution is also the reason for the strong spin-orbit coupling in the valence band, and the absence of the OAM in the conduction band causes weak conduction band spin-orbit coupling.

Apart from m_α, there is a contribution from the wavefunction circulation in a particular valley, m_v, an effect closely related to the Berry phase [44]. The full valley magnetic moment of a band can be calculated as:

$$m_v(\vec{k}) = -i(\frac{e}{2\hbar}) \left\langle \frac{\partial}{\partial \vec{k}}\Psi(\vec{k}) \right| \times [H(\vec{k}) - \epsilon(\vec{k})] \left| \frac{\partial}{\partial \vec{k}}\Psi(\vec{k}) \right\rangle \tag{2.8}$$

where $\epsilon(\vec{k})$ is the energy of the band at that $\vec{k}$.

Only considering the states near the band gap, Xiao et al. demonstrate that we can write the valley contribution to the OAM at the K and $-K$ points, for both valence and conduction bands, as [39]:

$$m_v(\tau) = \tau\mu_B^* \tag{2.9}$$

with μ_B^* representing the effective Bohr magneton:

$$\mu_B^* = \frac{e\hbar}{2m_e^*} \tag{2.10}$$

where m_e^* is the band effective mass, which is simply the curvature near the K and $-K$ points, which are, to first approximation, parabolic minima. This equation suggests that the valley OAM at the valence and conduction band for the same τ are of the same sign (for a hole in the valence band, and electron in conduction band) and close in magnitude, as the effective masses of the hole and electron are close [45]. For different τ, the sign of the moment flips, as expected from time-reversal symmetry. Finally, one finds the total magnetic moment of a band as the sum of the above band and valley contributions: $m = m_\alpha + m_v$.

Having analyzed the electronic properties of TMD monolayers, we are now ready to investigate the optical response of these materials, which will be centered on their direct band-gap in the K and $-K$ valleys.

2.1.3 Excitons in TMD Monolayers

In order to examine the optical properties of TMD monolayers, let us begin by defining the low-energy optical excitation of any semiconductor - the exciton. An exciton is a particle composed of an excited electron that resides in the conduction band and the hole it leaves behind in the valence band. Being oppositely charged, the electron and hole form a bound state qualitatively similar to hydrogen, or better yet positronium. Excitons feature a series of Rydberg states, with the 1s state being the lowest energy state, and their spatial extent is described by their Bohr radius. Excitons are composite quasiparticles, and since their components are two half-integer spin fermions, excitons are themselves bosons with integer spins. This holds so long as the density of the excitons is not too high, such that their separation becomes comparable to their Bohr radii, at which point they undergo a Mott transition where the excitons dissociate into a fermionic electron-hole liquid [46]. Excitons can be generated resonantly, by matching the excitation energy to their emission energy, or by exciting with an energy above the band-gap and allowing the electron to relax into the bottom of the conduction band and form the exciton.

In general, the two main types of excitons are the Wannier-Mott and Frenkel excitons. Wannier-Mott excitons are defined as having a Bohr radius singificantly larger than the lattice constant of their host material, while Frenkel excitons have Bohr radii on the order of, or smaller than the lattice constant [47]. In TMD monolayers, as is typical of semiconductors, the dominant type of exciton is the Wannier-Mott exciton, with a radius of $\sim$ 1-1.5nm [48]. However, unlike a typical Wannier-Mott exciton, excitons in TMD monolayers feature large binding energies of ~ 0.5 eV, owing to the

reduced screening in their low-dimensionality regime [49]. The large binding energies also contribute to exciton stability in this platform, making it suitable for the study of many-excitonic phases.

Crucially, because the TMD monolayer band-gap is direct, excitons can re-combine radiatively. This phenomenon is called photoluminescence (PL), and, as we will see throughout this work, the excitonic PL allows us to measure indirectly various properties of the exciton that generated it. Since the excitons are confined to a 2D plane, the direction they emit light is primarily out-of-plane, since the direction of light propagation is perpendicular to the transition dipole. Therefore, excitonic PL can be collected straightforwardly via an objective placed above the plane of the material. The energy at which the excitons emit is called the excitonic band-gap, and is lower than the single-particle band-gap by the electron-hole attraction [26].

2.1.4 Optical Selection Rules in TMD Monolayers

It is instructive to see what kinds of optical transitions are allowed in our TMD monolayers, as optically generated excitons are the primary focus of this work. Since each photon carries a spin unit ($\pm\hbar$) of angular momentum, depending on its circular polarization, each optical transition in which a single photon is absorbed or emitted must occur between two states which differ in angular momentum by this same amount, in order to maintain conservation of angular momentum. Since light couples to matter primarily via its electric field component, rather than via the magnetic field, optical transitions are primarily spin-conserving, since the electric field component of light does not act on the spin [47]. The optical excitation of a valence band electron to the conduction band in a spin-conserving way is also called an electric dipole transition. The hole the electron leaves behind has the opposite spin to the excited electron. This preserves total spin conservation, since the initial full valence band has a net spin of zero, so the removal of an electron spin must leave a net spin opposite to the

removed electron. Therefore, the exciton generated by an electric dipole transition is in a singlet state, with a total spin of 0. The case where an optical transition occurs with a spin flip of the excited electron from its initial state occurs when the magnetic field component of the light couples to the electron, in which case the exciton is in a triplet state, with a total spin of $\pm$ 1. The coupling of the magnetic field to electrons is so much weaker that such excitons are commonly referred to as 'dark', or spin-forbidden. But if the optical transition results in a spin-0 particle, what happens to the spin of the absorbed photons?

In atomic spectroscopy, the answer to this question is that bright transitions occur between orbitals which differ in orbital angular momentum by $\pm$ 1 (e.g. s to p, or p to d, etc.), so that the photon angular momentum can be absorbed. In solids, other degrees of freedom can also carry angular momentum, and transitions can occur both across different atoms and within the same atom [50]. Also, much like the crystal translational momentum, since the rotational symmetry is reduced, the angular momentum is conserved only to modulo 3, for the three-fold symmetry of the crystal. In order to determine which transitions are bright in a TMD monolayer, we can follow Xiao et al. [40] and consider a simplified model of the TMD band structure, which only considers the valence and conduction bands near the $\pm K$ points:

$$|\psi_c\rangle = \left|d_z^2\right\rangle \tag{2.11}$$

$$|\psi_v^\tau\rangle = \frac{1}{\sqrt{2}}(|d_{x^2-y^2}\rangle + i\tau\,|d_{xy}\rangle) \tag{2.12}$$

where τ is the valley index ($+1$ for K and -1 for $-K$). The model only considers the metal d bands, which as we saw in the preceding section dominate near the K points of the two bands. In order to evaluate the optical transition strength for an incident photon of a given circular polarization $\sigma_\pm$ at a particular valley, we need to

evaluate the dipole transition strength $P_{\pm}$, which is given by the inter-band matrix element of the generalized momentum operator connecting the valence and conduction band states [47]:

$$\hat{P}_{\pm}(\vec{k}) = \hat{P}_x(\vec{k}) \pm i\hat{P}_y(\vec{k}) \tag{2.13}$$

with $\vec{k}$ here representing the k-space distance from $\pm$ K points, and $\hat{P}_x$ and $\hat{P}_y$ representing the linear inter-band elements of the generalized momentum:

$$\hat{P}_x(k) \equiv \langle \psi_v(k) | \frac{m_0}{\hbar} \frac{\partial \hat{H}}{\partial k_x} | \psi_c(k) \rangle \tag{2.14}$$

$$\hat{P}_y(k) \equiv \langle \psi_v(k) | \frac{m_0}{\hbar} \frac{\partial \hat{H}}{\partial k_y} | \psi_c(k) \rangle \tag{2.15}$$

with m_0 being the free electron mass.

In order to evaluate this, we need a Hamiltonian for $\vec{k}$ in the neighborhood of the $\pm$ K points. Xiao et al. [40] again use symmetry considerations to arrive at:

$$\hat{H} = at(\tau k_x \hat{\sigma_x} + k_y \hat{\sigma_y}) + \frac{\Delta}{2}\hat{\sigma_z} \tag{2.16}$$

with a being the lattice constant and t being a hopping parameter that quantifies the strength of the mixing of the two eigenstates at $\pm$ K away from these high-symmetry points, τ as the aforementioned valley index and Δ is the band-gap.

Evaluating $\hat{P}_{\pm}(\vec{k})$ now yields:

$$|P_{\pm}(\vec{k})|^2 = \frac{m_0^2 a^2 t^2}{\hbar^2}(1 \pm \tau \frac{\Delta}{\sqrt{\Delta^2 + 4a^2t^2k^2}})^2. \tag{2.17}$$

Since $\Delta \gg atk$ near the K points (where $\vec{k}$ is by definition differential), we can simplify the result to:

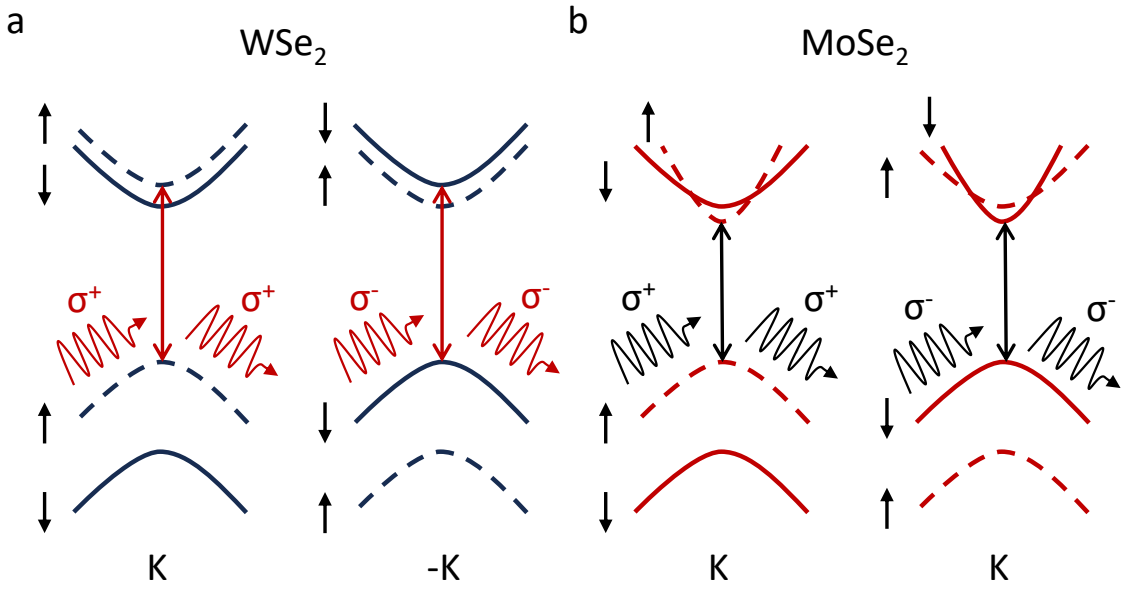

Figure 2.5: TMD Monolayer Light Absorption and Emission. **a.** Light coupling by valley of a WSe_2 monolayer, considering the lowest energy bright transition. Bands not to scale. **b.** Light coupling by valley of a $MoSe_2$ monolayer, considering the lowest energy bright transition. Bands not to scale.

$$|P_{\pm}(\vec{k})|^2 = \frac{m_0^2 a^2 t^2}{\hbar^2}(1 \pm \tau)^2 \tag{2.18}$$

So, for $\tau = 1$, near the K valley, P_+ is finite but P_- is 0, and for $\tau = -1$, near the -K valley, P_- is finite but P_+ is 0. Therefore, light of a $\pm$ circular polarization couples strictly to the $\pm$ K valley.

Let us finally consider how this result defines the optical selection rules, while also including the spin-orbit coupling. Figure 2.5 shows the selection rules for WSe_2 and $MoSe_2$, considering the lowest-energy allowed transition. We see that light of a particular circular polarization couples to a single valley, and therefore drives electrons only of a single spin. Therefore, circularly polarized light incident on TMDs can generatesspin- and valley- polarized excitons [51, 52, 53]. Interestingly, the conduction band structures for W-based and Mo-based TMDs differ in that the order of the spin-split bands are opposite. Therefore, the lowest energy state in W-based TMDs is in

fact a spin-dark state. However, this splitting is small compared to the valence band splitting, and since spin-flip scatterings of excitons tend to occur rarely, this has little effect on the emission from W-based TMDs. Therefore, bright excitons are readily created and observed in W-based TMDs.

The result above can also be expanded on by considering the transition in terms of angular momentum quantum numbers of the valence and conduction band. In this, we follow Yu et al. [54] and note that, since TMD monolayers have a three-fold in-plane rotation symmetry and an out-of-plane mirror symmetry, any Hamiltonian, and therefore the states, must also conserve these symmetries. For the states at the K point ($\tau = 1$), and now explicitly including the spin S_z:

$$\hat{C}_3 \left|\psi^1_{n,S_z}\right\rangle = e^{-i\frac{2\pi}{3}(C_3(n)+S_z)} \left|\psi^1_{n,S_z}\right\rangle, \tag{2.19}$$

$$\hat{\sigma}_h \left|\psi^1_{n,S_z}\right\rangle = e^{-i\frac{2\pi}{3}(\sigma_h(n)+S_z)} \left|\psi^1_{n,S_z}\right\rangle, \tag{2.20}$$

where $\hat{C}_3$ is the 120° rotation operator about a high-symmetry point (X atom, M atom or hexagonal center point), $\hat{\sigma}_h$ is the mirror inversion operator, and the index n can be v and c, for valence and conduction bands. Table 2.2 summarizes the eigenvalues of the valence and conduction bands for the two operators in a generic TMD monolayer [55]. Importantly, both bands are even under the $\hat{\sigma}_h$ operator, but they have different eigenvalues under in-plane C_3 rotation, for the same reason that they have opposite sign Berry curvature (see Section 2.1.2). Just as with Berry curvature, the -K point has all the same values as shown in Table 2.2, but with opposite sign, as dictated by the time-reversal relationship between the K and -K points.

Using the full 3D momentum operator $\hat{P} = \hat{P}_+\vec{e_+} + \hat{P}_-\vec{e_-} + \hat{P}_z\vec{z}$, with $\vec{e}_\pm = \vec{x} \pm i\vec{y}$, and using the identities $\hat{C}_3\hat{P}_\pm\hat{C}_3^{-1} = e^{\mp i\frac{2\pi}{3}}\hat{P}_\pm$, $\hat{C}_3\hat{P}_z\hat{C}_3^{-1} = \hat{P}_z$, $\hat{\sigma}_h\hat{P}_\pm\hat{\sigma}_h^{-1} = \hat{P}_\pm$ and $\hat{\sigma}_h\hat{P}_z\hat{\sigma}_h^{-1} = \hat{P}_z$ which hold due to the symmetries of the Hamiltonian, Yu et al. show that a transition between two states $\left|\psi^1_{n,S_z}\right\rangle$ and $\left|\psi^1_{m,S'_z}\right\rangle$ couples to a photon with

Table 2.2: TMD monolayer symmetry operator quantum number at the K-point. Values obtained from [55]

	C_3(h)	C_3(X)	C_3(M)	σ_h
v	0	+1	-1	+1
c	+1	-1	0	+1

polarization:

$$\sigma_{\pm} \text{ for : } \begin{cases} C_3(m) - C_3(n) + S'_z - S_z = 3N \pm 1 \\ \sigma_h(m)\sigma_h(n)e^{i\pi(S'_z - S_z)} = 1 \end{cases} \tag{2.21}$$

$$z \text{ for : } \begin{cases} C_3(m) - C_3(n) + S'_z - S_z = 3N \\ \sigma_h(m)\sigma_h(n)e^{i\pi(S'_z - S_z)} = -1 \end{cases} \tag{2.22}$$

(for N = ...,-1,0,1,...).

As seen from Table 2.2, $C_3(c) - C_3(v) = 1$ and $\sigma_h(c) = \sigma_h(v) = 1$ at the K point. The complete optical selection rules are summarized in Figure 2.6. As before, one finds that the $\pm K$ points couple to photons of $\pm\sigma$ circular polarizations, but also that there is an allowed spin-flip transition, driven by light which is linearly polarized in the out-of-plane direction, and which is mediated by the finite spin-orbit coupling in the system and is still an electric dipole transition [54]. This transition is therefore not possible to drive with light normally incident on the sample.

2.2 TMD Heterostructures

One of the most exciting aspects of TMD monolayers is the prospect of using them to construct heterostructures by placing different TMD monolayers in contact. This way, new materials with properties not found in nature can be engineered on the nanoscale. As described in Section 1.1.1, monolayers of TMD materials we study are naturally only found in the H-stacked configuration when forming multilayer and bulk

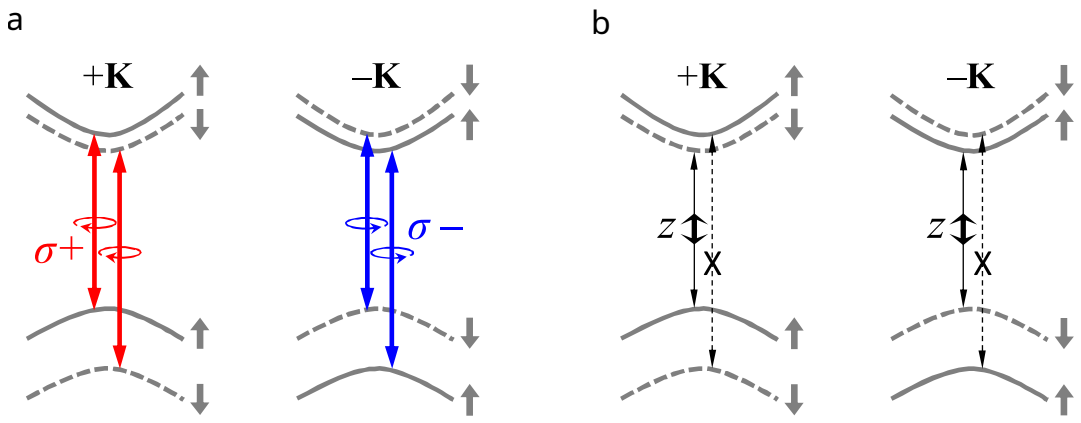

Figure 2.6: TMD Monolayer Full Selection Rules. **a.** Spin-conserving allowed transitions coupling to different circular polarizations in different valleys. **b.** Spin-flip transition coupling to a z-polarized photon, mediated by the spin-orbit coupling. Bands not to scale. Figure adapted from [54].

pieces. Therefore, in addition to mixing different TMD materials when constructing heterostructres, another interesting degree-of-freedom emerges - the twist angle. In principle, when fabricating a heterostructure device, one can arbitrarily select the twist angle between the two layers.

2.2.1 The Moiré Potential

When two monolayers are placed on top of each other at some twist angle, they form a moiré pattern. A moiré pattern is a spatial beating pattern stemming from the interference of the mismatched periodic structures of the two layers. If the two layers have either an angle mismatch, a mismatch in their lattice period, or both, there will emerge a finite difference in the reciprocal vectors of the two lattices along any given direction, the inverse of which corresponds to the moiré period. Just as with regular crystals, the moiré pattern can be divided into unit cells, often called moiré supercells. In order to get some intuition for these patterns, let us see what happens when two identical lattices are twisted relative to one another (Figure 2.7). We see that larger twist angles introduce smaller moiré periods. However, a moiré pattern

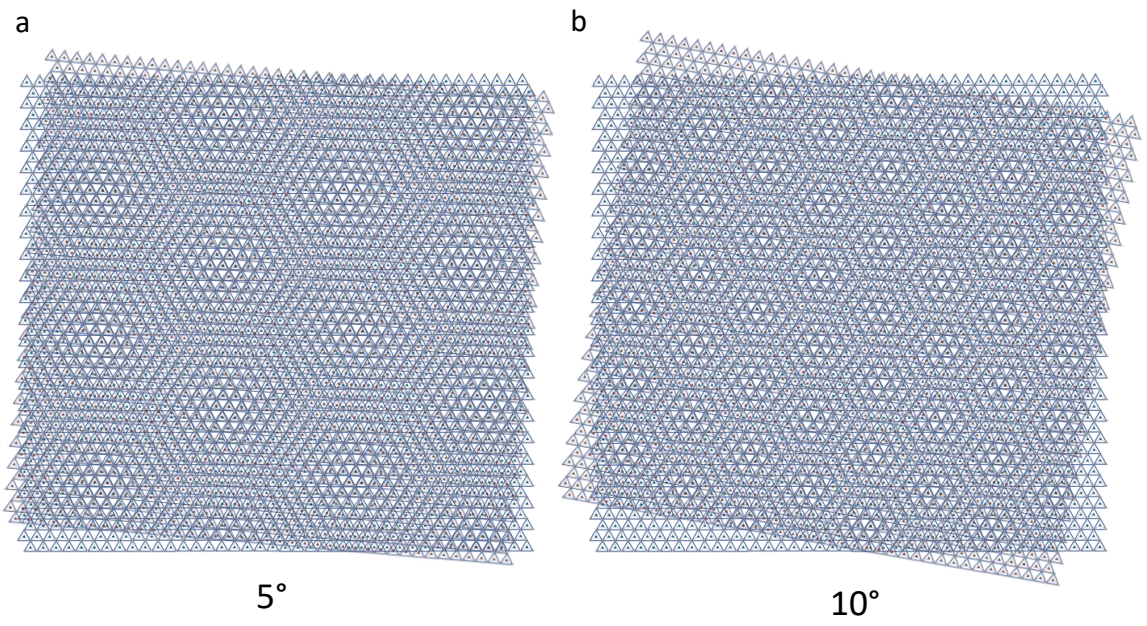

Figure 2.7: Moiré Patterns at Different Twist Angles. The two lattices are identical, but twisted relative to one another with **a.** at 5° and **b.** 10°. We see that a larger twist angle induces a smaller moiré period.

can also be realized using two lattices with different periods, even if they are aligned with 0° twist.

Figure 2.8 shows a moiré cell of a heterostructure of WSe_2 and WS_2 at a 0° twist angle, also called R-stacking. While in the corners the two lattices begin well-aligned, the lattice mismatch causes the alignment to drift inside the unit cell, until it is recovered in another corner, one moiré period later. A particular point inside the unit cell is often referred to as a 'registry', and the unit cell features several high-symmetry registry points, namely R_h^h, R_h^X and R_h^M, illustrated in Figure 2.8. The high-symmetry registry points are labeled in a R_h^μ convention, signifying which site $\mu = M, X$ or h of the top layer aligns with site h of the bottom layer, with M signifying the metal atom site, X the chalcogen atom site, and h the hexagonal lattice center site.

A key parameter of the moiré pattern is its period. By considering the difference

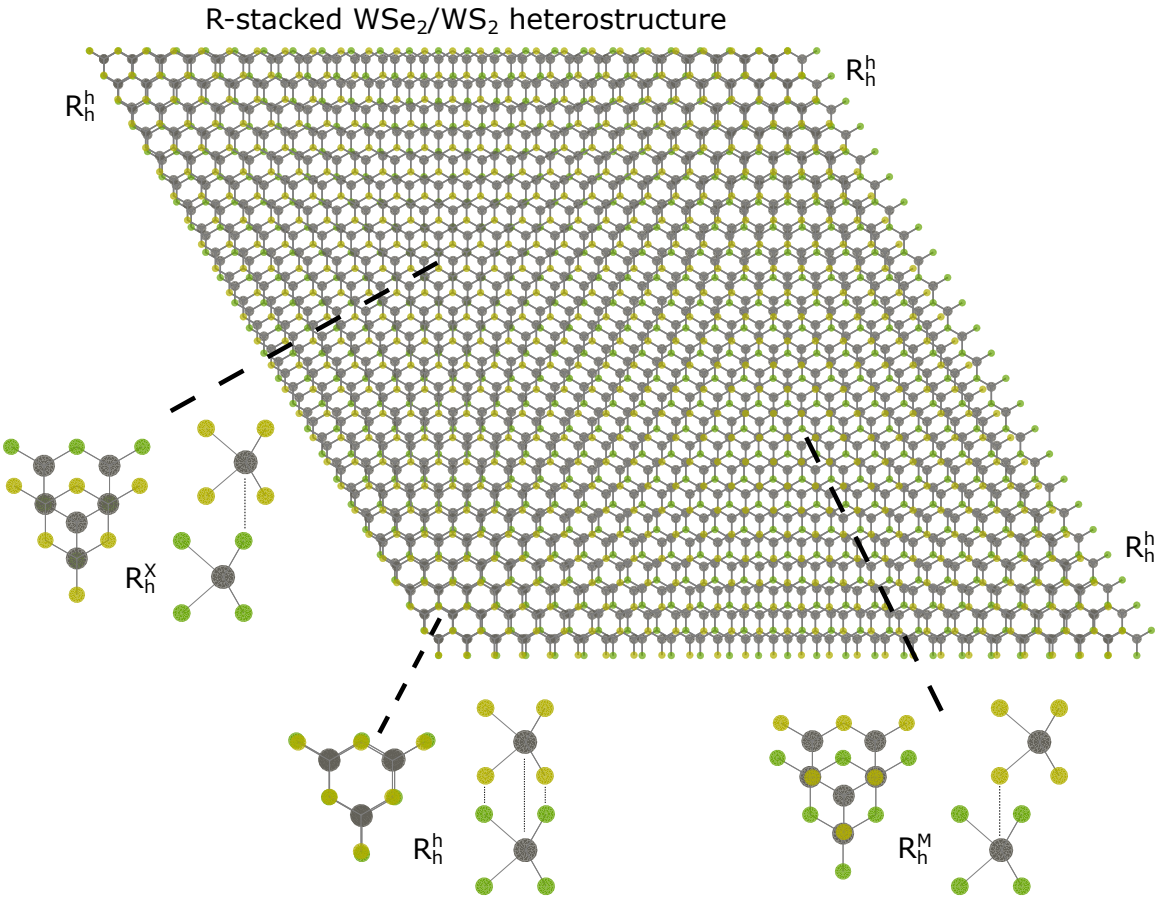

Figure 2.8: R-Stacked TMD Moiré Cell. Indicated are the high-symmetry registry positions - R_h^h, when the atoms of one layer are exactly horizontally aligned with the corresponding atoms of the other layer; R_h^X, when the metal of the top layer is aligned with the chalcogen of the bottom layer; and R_h^M, when the metal of the bottom layer is aligned with the chalcogen of the top layer.

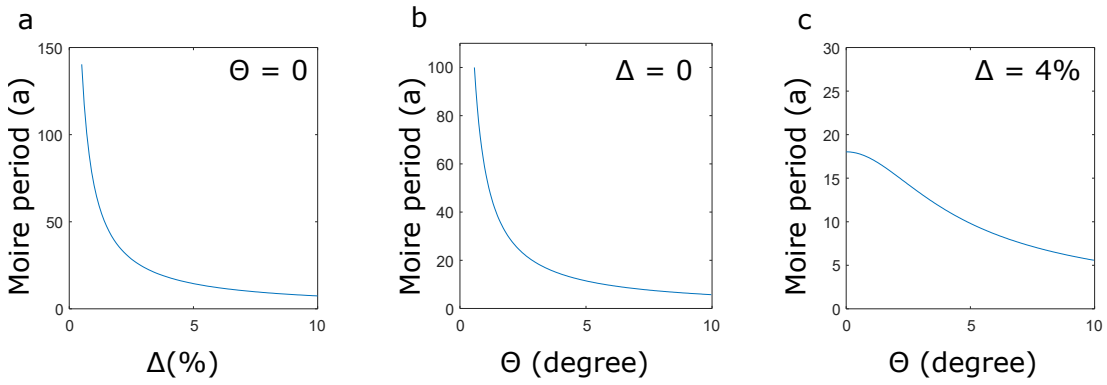

Figure 2.9: The Moiré Period for Different Twist Angles and Lattice Mismatches. Twist angles defined modulo 60°. **a.** Moiré period as a function of lattice mismatch for an aligned (R-stacked, 0° twist angle) heterostructure. **b.** Moiré period as a function of twist angle for a heterobilayer (or homobilayer) with no lattice mismatch. **c.** Moiré period as a function of twist angle for a heterobilayer with 4% lattice mismatch.

between the reciprocal vectors of the two hexagonal lattices, the moiré period can be shown to be of the form [56]:

$$a_M(\theta, \Delta) = \frac{(1+\Delta)a}{\sqrt{2(1+\delta)(1-\cos\theta)+\delta^2}},$$

where a_M is the moiré period, θ is the twist angle (modulo 60°), and Δ is the dimensionless lattice mismatch, calculated as $\Delta = \frac{|a_1-a_2|}{(a_1+a_2)/2}$. Figure 2.9 shows the moire period as a function of lattice mismatch and twist angle. The twist angle is defined up to modulo 60°, given the underlying hexagonal lattices. With no twist or lattice mismatch, the period diverges, which is essentially the case with natural multilayer and bulk TMDs.

As we established in Section 1.1.1, the natural conformation for TMD multilayers is H-stacking, having a twist angle of 60° between the layers. In heterostructures, while the H-stacked case has the same moiré period as the R-stacked case, they are distinct conformations with different physical properties. Figure 2.10 shows a moiré cell of a heterostructure of WSe_2 and WS_2 with H stacking (60° twist angle). Analogously to the R-stacked case, the unit cell features several high-symmetry registry

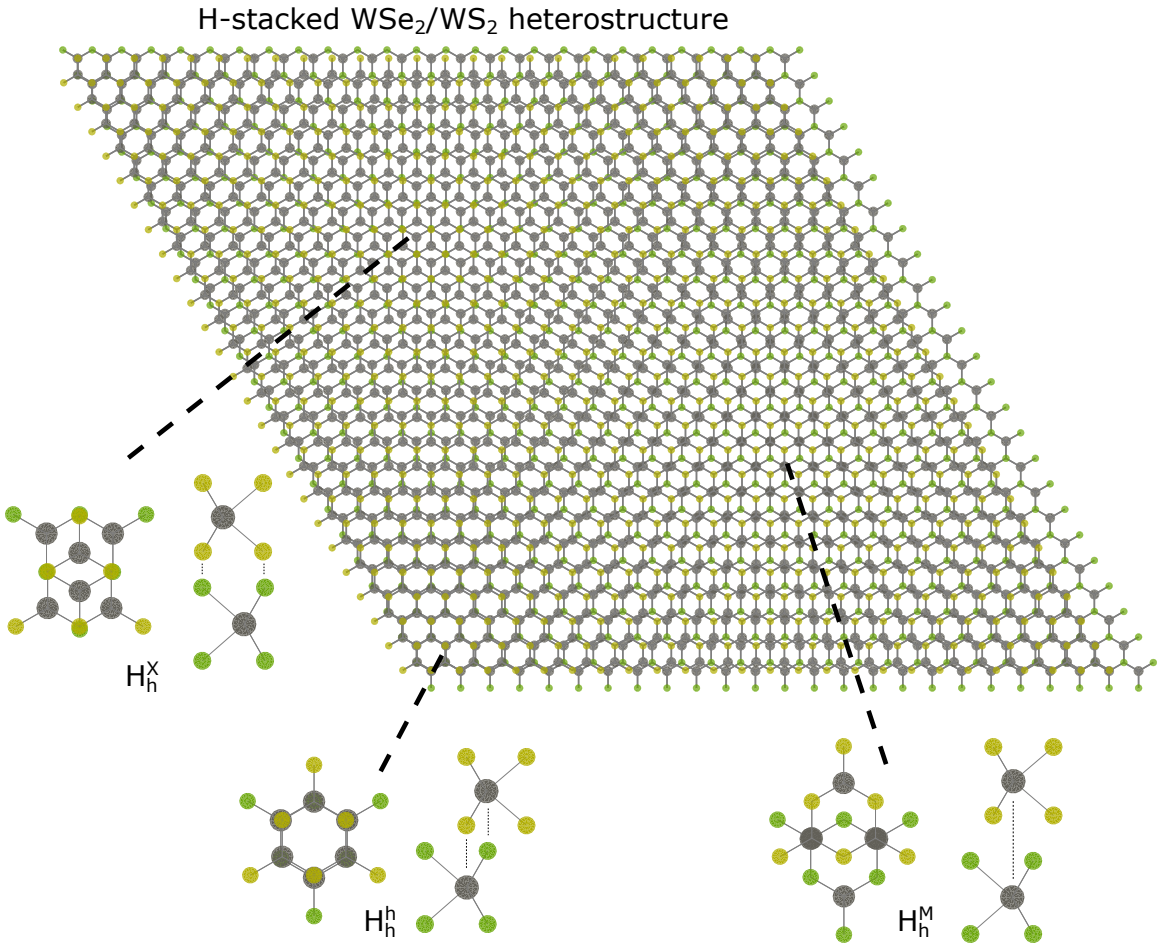

Figure 2.10: H-Stacked TMD Moiré Cell. Indicated are the high-symmetry registry positions - H_h^h, when the chalcogen atoms of one layer are exactly horizontally aligned with the metal atoms of the other layer; H_h^X, when the chalcogens of the two layers are aligned (but not the metals); and H_h^M, when the metals of the two layers are aligned (but not the chalcogens).

points, namely H_h^h, H_h^X and H_h^M.

This changing registry leads to the formation of the moiré potential, which is a consequence of the different electrostatic properties of the constituent atoms of the two lattices. As the registry changes, the metal and chalcogen atoms from different layers have different local displacements, and the amount of charge transfer between the layers that occurs due to the different electronegativities of the metal and chalcogen atoms varies. This charge transfer then leads to a electrostatic potential landscape that any additional charge carriers introduced to the system would see. The moiré

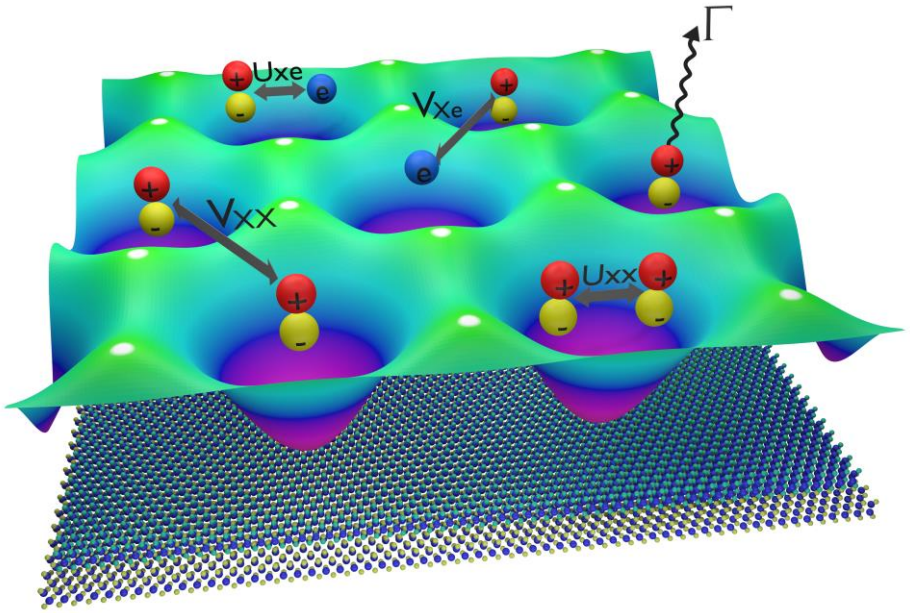

Figure 2.11: Diagram of the Moiré Potential in WSe_2/WS_2 Heterobilayer. This diagram illustrates the electrostatic potential in a heterobilayer. The potential can confine both charge carriers like electrons, and electrically neutral particles like excitons by acting on its constituent electron and hole. Sketch is primarily illustrative, and not to scale. Real moiré potentials for both excitons and electrons can be significantly more complex, and feature multiple minima/maxima in each cell. The moiré potential also defines several interaction scales between electrons and excitons, such as the on-site exciton-exciton interaction U_{XX}, cross-site exciton-exciton interaction V_{XX}, on-site electron-exciton interaction U_{Xe} and cross-site electron-exciton interaction V_{Xe}, and can influence the exciton emission rate Γ.

potenital shares the same periodicity as the moiré pattern, and the difference between the peaks and valleys is called the moiré potential depth. The details of the moiré potential, such as its exact structure and the dependence of its depth on the moiré period, are nontrivial, but for angles close to R and H stacking, the typical depth of the potential has been measured to be on the order of 100-400 meV [57].

Figure 2.11 shows a sketch of the moiré potential, illustrating how, at such depths, the potential can trap electrons and excitons at low temperatures, as well as define the scope of interactions between them. This means that any electrons and holes that are doped into the heterostructure, as well as excitons that may be formed, experience a

sizeable periodic potential, which, as we will explore in this work, can have profound effects on the low-energy behavior of the system.

2.2.2 Optical properties of Type-II TMD Heterostructures

Before we examine how electrons and excitons interact with each other and the moiré potential in TMD semiconductor heterostructures, let us turn to the question of the nature of individual excitons in such structures, namely their optical generation and their light emission. The nature of the lowest energy exciton is determined by the band alignment between the two monolayers. As shown in Figure 2.12, this band alignment can have three different configurations, depending on the relative energies of the conduction-band minimum (CBM) and valence band maximum (VBM) of the two layers [47].

Almost all heterobilayers involving the group-IV TMDs have type-II alignments, as shown in Table 2.3, with the only exception of $MoSe_2/WS_2$, where the CBM are nearly of the same energy, and the type-I alignment can be changed to type-II by external electric field [58]. This type-II configuration means that electrons and holes at the interface reside in different layers at equilibrium. This has an interesting consequence for excitons in these structures, whose ground state become the interlayer exciton (IX) [59, 60, 19, 61, 62]. The interlayer exciton (as opposed to the *intra*layer exciton of the monolayer, often labelled as simply X) is still a bound state of an excited electron and hole, but the carriers reside in different layers, according to the type-II gap alignment. Therefore, the IX is a spatially indirect exciton, because of the spatial separation of the two layers, which is typically comparable to the layer thickness of 0.7 nm.

In order for the exciton to be optically active, it is important that the band-gap of the heterostructure is direct, in the same way that the monolayer band-gap is. This means that, in momentum space, the electron and hole states which reside in the $\pm$K

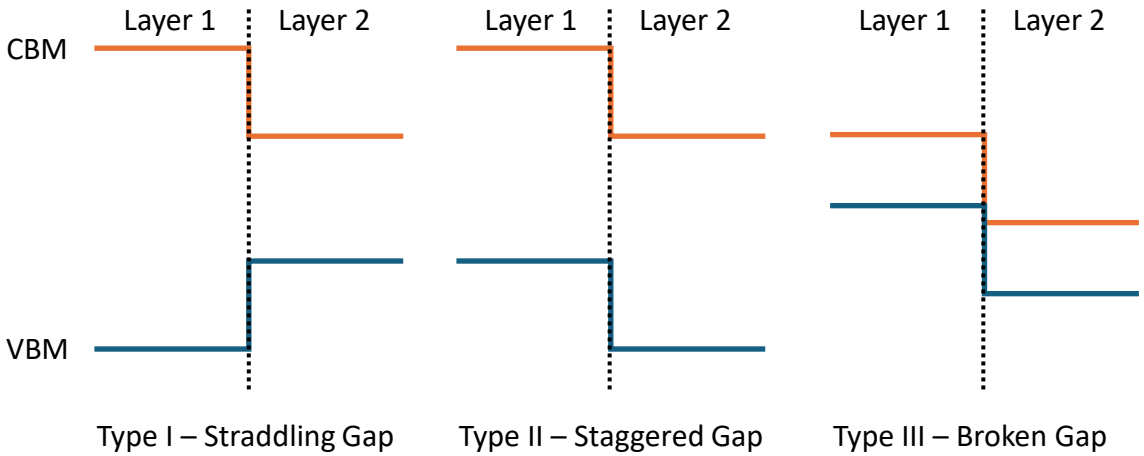

Figure 2.12: Diagram of the three semiconductor heterojunction types. Type I, or straddling gap, junctions have the conduction-band minimum (CBM) and valence band maximum (VBM) of one layer (Layer 2) both between the CBM and VBM of the other layer (Layer 1). In such a structure, a doped hole or electron would move to Layer 2 to lower their energy. Type II, or staggered gap, junctions have both the CMB and VBM of one layer (Layer 2) lower than that of the other. In this case, a doped electron would lower its energy by moving to Layer 2, but a doped hole would do so by moving to Layer 1. Type III junctions have a broken gap, as the VMB of one layer is higher than that of the other, and have a large amount of charge transfer between the layers without any doping.

Table 2.3: TMD Heterostructure Junction Types and Charge Carrier Equilibrium Position.

TMD 1 \ TMD 2	WSe_2	WS_2	$MoSe_2$	MoS_2
WSe_2	Homobilayer	Type II, h^+ in WSe_2, e^- in WS_2 [19, 63]	Type II, h^+ in WSe_2, e^- in $MoSe_2$ [60, 64]	Type II, h^+ in WSe_2, e^- in MoS_2 [65, 66]
WS_2	\	Homobilayer	Type I, h^+ and e^- in $MoSe_2$* [58]	Type II, h^+ in WS_2, e^- in MoS_2 [67, 68]
$MoSe_2$	\	\	Homobilayer	Type II, h^+ in $MoSe_2$, e^- in MoS_2 [69, 70]
MoS_2	\	\	\	Homobilayer

*(close to Type II due to near-degenerate e^- bands)

points of each layer need to be nearly-aligned across layers for the heterostructure band-gap to be direct. Figure 2.13 shows the in-plane alignment of two monolayer Brillouin zones. Because of the inequivalency of the K and $-K$ points, there are two distinct ways to form the IX - between two $+K(-K)$ points of the two layers (R-stacking) and between a $+K(-K)$ point of one layer and the $-K(+K)$ point of the other (H-stacking). The greater the misalignment of the $\pm$K points between the layers, the more indirect the band-gap becomes, and the oscillator strength of the IX correspondingly decreases. In the real space picture, this means only heterostructures with twist-angles close to 0° and 60° feature bright IXs. As shown in Figure 2.13b, the finite mismatch between the in-plane momenta of the valleys across the two monolayers mean that the bright exciton features a non-zero center-of-mass momentum relative to the K point. Figure 2.13b also shows the electron-hole interaction V. While it common to depict an exciton using the single-particle bands (and will be done throughout this thesis for simplicity), one must keep in mind that the electron-hole attraction changes the Hamiltonian compared to the single charge carrier picture, and the resulting excitonic eigenstate is a mixture of the single particle states for the electron and hole, as indicated by the Feynman diagram. The excitonic band-gap is also smaller compared to what the single particle bands alone would indicate, due to the excitonic binding energy.

Being spatially indirect in the out-of-plane direction, the IX has a 2-3 orders of magnitude smaller optical transition dipole than X, even in a well in-plane-aligned heterostructure [60]. Therefore, IX lifetime is significantly longer than that of X, and the IX transition has poor light absorption, requiring significant effort to detect experimentally [71]. Therefore, a typical scenario in a Type-II heterostructure is that intralayer excitons are generated efficiently in one of the monolayers, which then rapidly ($\sim$ fs) turn into interlayer excitons by charge transfer [72]. Figure 2.14 illustrates this mechanism. Once the IX is formed, it can radiatively decay at an

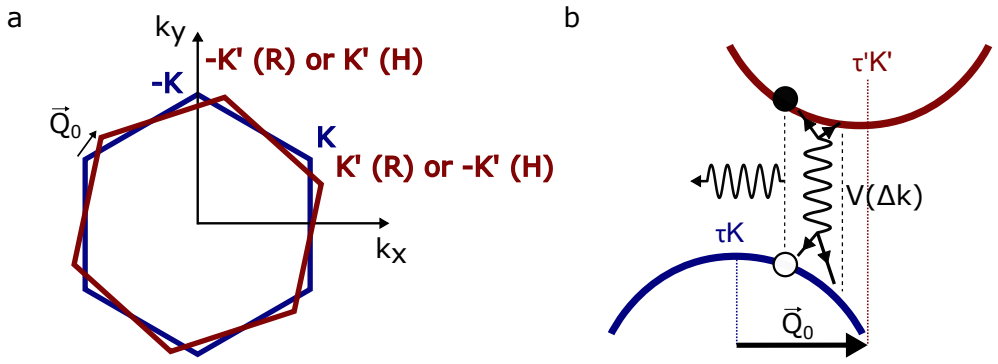

Figure 2.13: Diagram of k-space alignment of the Brillouin zones in a Type-II heterostructure. **a.** Brillouin zone edges for two monolayers in a heterostructure. The (6-fold symmetric) $\vec{Q}_0$ denotes the momentum-space displacement between the $\pm$K points of the two layers. Different stacking configurations (R - close to 0° and H - close to 60°) have opposite valleys aligned in the bottom layer (unprimed labels) and top label (primed labels). **b.** Sketch of the finite-momentum bright IX. The valley indices for the top and bottom layers are twist-angle dependent, as indicated in panel a. Due to the momentum mismatch of the $\pm$K points of the two monolayers, the bright exciton (with no relative momentum difference between the electron and hole) has a finite center-of-mass momentum with respect to the $\pm$K points. The Feynmann diagram represents the electron-hole interaction V, which acts as a momentum-conserving coherent scattering of the bright exciton across the single-particle states. For larger magnitudes of $\vec{Q}_0$, the oscillator strength of the exciton rapidly decreases, as the gap become less momentum-direct.

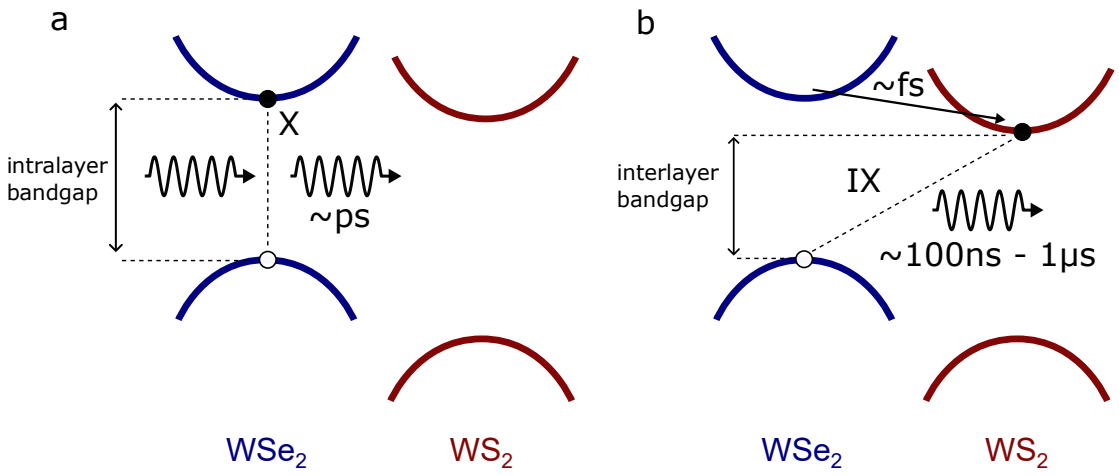

Figure 2.14: Diagram of X to IX transition in a WSe_2/WS_2 Type-II heterostructure. **a.** Diagram of exciton generation and the $\sim$ ps lifetime of radiative emission as an intralayer exciton X, at the WSe_2 band-gap energy. Details of spin-orbit coupling omitted. **b.** Intra- to interlayer exciton conversion, which is a competing mechanism to intralayer emission, with a $\sim$ 3 orders of magnitude faster rate. Subsequent radiative interlayer emissions IX can have a lifetime up to a microsecond, depending on the sample. The illustrated bands of the two samples are drawn side-by-side for clarity, but are presumed to be at the same momentum, making the IX in-plane momentum direct.

energy lower than the intralayer exciton that was excited, with the difference in the energy of the photoluminescence corresponding to the difference between the intra- and inter- layer excitonic band-gaps. As is common practice, in this and subsequent IX emission diagrams, the bands are drawn side-by-side for clarity, but are presumed to be in-plane momentum-direct across the layers.

2.2.3 The Moiré Potential and Optical Selection Rules

The moiré potential has a profound effect on the optical properties of the heterobilayer devices. In fact, the moiré potential can be sufficiently deep to localize IXs. Figure 2.15 shows that at twist angles very close to the H- and R- stackings, the band structure is very flat, admitting highly localized states [73]. The fact that flat bands

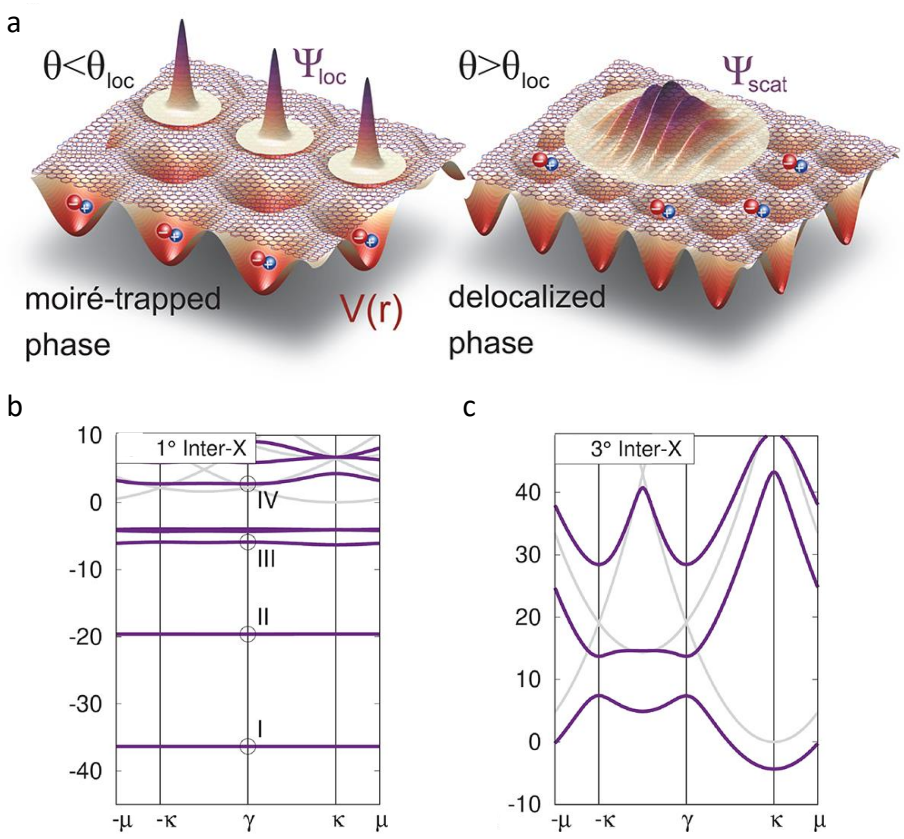

Figure 2.15: Trapped and delocalized moiré IXs. All panels adapted from [73], and the band diagrams are based on DFT calculations. **a.** Diagram of localized and scattered moiré IXs. Twist angles near 0° and 60° lead to moiré potentials with sufficient depth and period to suppress the kinetic hopping of the exciton. **b.** The band diagram of a low twist-angle (1°) $MoSe_2/WSe_2$ heterobilayer shows flat excitonic bands for IXs, which admit highly localized states. **c.** The band diagram of a higher twist-angle (3°) $MoSe_2/WSe_2$ heterobilayer, no longer featuring flat excitonic IX bands.

lead to localization can be understood in the following way - since the group velocity of wave packets is $v_g = dE(k)/dk$, flat bands mean $v_g = 0$, meaning that a localized state, once initialized, does not move. Therefore, the trapped excitons in moiré lattices with flat excitonic bands can be understood as close to arrays of quantum dots, which has been experimentally demonstrated [74, 75, 76].

The optical selection rules for the IX are similar to those of the monolayer discussed in Section 2.1.4, with some additional complications introduced by the moiré potential. The main point is the spin-valley locking is largely inherited from the

monolayer case, and IX emission that is generated with circularly polarized light retains some of this circular polarization when it emits. However, in IX there can be both co- and cross- polarization, which is the phenomenon where the emission is primarily of the same or opposite polarization as the absorbed photon. The work by Yu et al. discussed earlier [54] also deals with these issues, and we will briefly recapitulate the salient points here. In a heterobilayer, the σ_h symmetry is violated, but the C_3 symmetry is preserved at the high symmetry R_h^μ and H_h^μ sites, discussed in Section 2.2.1, such that the C_3 quantum number can be assigned to each site as a rotation center. Using the same analysis as in Section 2.1.4 yields the same selection rules for the K valley as in equations 2.21-2.22:

$$\sigma_\pm, \text{for} : C_3(c') - C_3(v) + S'_z - S_z = 3N \pm 1, \tag{2.23}$$

$$z, \text{for} : C_3(c') - C_3(v) + S'_z - S_z = 3N, \tag{2.24}$$

However, the selection rules are now site dependent, and the same K-point transition can couple with all three polarizations, at different registry sites, as shown in Table 2.4 [54]. In addition, by inclusion of second-order processes mediated by the spin-orbit and interlayer couplings, spin-flip transitions are also able to couple to normally incident $\sigma\pm$ photons. The table shows that the optical selection rules in heterobilayers are significantly richer and less restrictive than in case of the monolayer, and the same K-point exciton can now couple to both $\sigma+$ and $\sigma-$ emission, depending on where in the moiré lattice the recombination occurs. The optical properties of a particular heterostructure are difficult to predict *a priori*, but we will make use of this framework to interpet our results in later chapters.

Table 2.4: TMD heterobilayer registry-dependent selection rules at the K-point. Values obtained from [54].

	R_h^h	R_h^X	R_h^M	H_h^X	H_h^h	H_h^M
$\|v,\uparrow\rangle \leftrightarrow \|c',\uparrow\rangle$	$\sigma+$	$\sigma-$	z	$\sigma+$	$\sigma-$	z
$\|v,\uparrow\rangle \leftrightarrow \|c',\downarrow\rangle$	z	$\sigma+$	$\sigma-$	z	$\sigma+$	$\sigma-$
$\|v,\downarrow\rangle \leftrightarrow \|c',\downarrow\rangle$	$\sigma+$	$\sigma-$	z	$\sigma+$	$\sigma-$	z
$\|v,\downarrow\rangle \leftrightarrow \|c',\uparrow\rangle$	$\sigma-$	z	$\sigma+$	$\sigma-$	z	$\sigma+$

2.3 Field Modulation of Electronic and Excitonic Properties of TMD Devices

A key challenge in the pursuit of using TMDs for technological applications is the question of their integration into functional devices. In pursuit of this goal, two other van-der-Waals materials have played key roles - hexagonal boron nitride (hBN) and graphene. The former is an excellent insulator with a band-gap of almost 6 eV, and can also be cleaved down to the monolayer limit. Thick hBN flakes serve as a bulk insulator while few- or monolayer flakes are often used as means to separate layers in heterobilayer structures, which can suppress moiré effects [77]. The encapsulation of TMD monolayers with hBN yields remarkably high-quality and sharp optical emission from the TMDs [78], making hBN, with its atomically flat surface, a good choice for protecting and electrically insulating TMDs in devices. Graphene is a semi-metal due to its famous Dirac-like band structure, and features excellent conductivity, especially flakes of few-layer-graphene (FLG), which are less susceptible to strain-induced increases in local resistance. Graphene also has no band-gap and therefore a low Shottky barrier when integrated with metals or TMDs [79]. These two materials are well-suited for making TMD devices with electrical control, with hBN as an insulator and FLG flakes in the role of contact lead or voltage gate. In this section, we will see how these elements can be used to apply electric field and electrostatic doping to TMD samples. In our setups, we also have access to an out-of-plane magnetic field, as

detailed in Chapter 4. We will also explore how applying doping and external electric and magnetic fields on the sample changes the character of optical emission, allowing for *in-situ* tunability of optical properties, which is a key advantage of the TMD platform. We will summarize some important results from the literature, which illustrate how these external fields modify the photoluminescence from TMD monolayers and heterostructures and inform our analysis in subsequent chapters.

2.3.1 TMD Device Design

Let us examine a typical TMD device design. Figure 2.16a shows a dual-gated TMD heterostructure device, which can independently apply electrostatic doping and out-of-plane electric field to the heterostructure. The sample of interest is in the middle, 'sandwiched' between two thick hBN flakes, which are in turn 'sandwiched' between graphite gates. Using a simple parallel-plate capacitor model, which is valid because of the extremely flat aspect ratio of the sample, we can easily deduce two configurations - doping without electric field (Figure 2.16b) and electric field without doping (Figure 2.16c). Any combination of doping and electric field can be achieved as a linear superposition of the two configurations. In this way, full electrical control of the sample is achieved. In such samples, a small but finite Schottky barrier is still typically formed at the interface between the contact graphene and the TMDs, which acts as a diode and needs to be overcome before the sample begins to be doped. In the illustrated case of a heterostructure, the doped charge carriers would go to the appropriate layer, depending on the relative alignment of the TMD monolayer bands, as seen in Table 2.3.

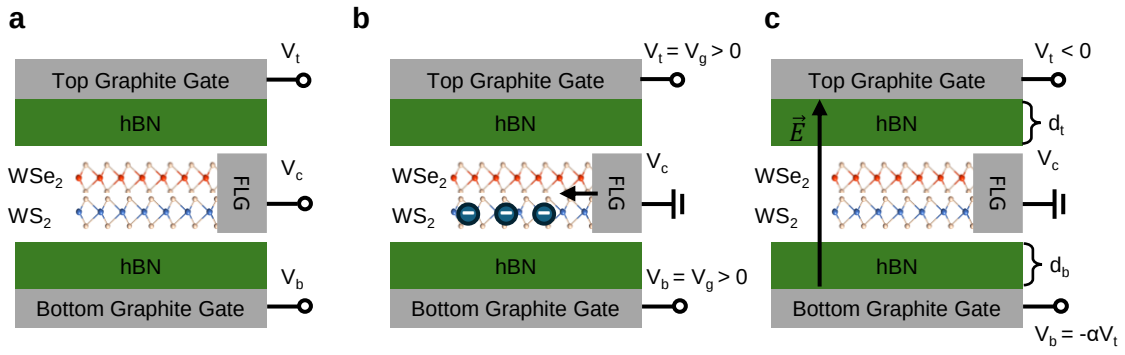

Figure 2.16: Diagram of a typical dual-gated WSe_2/WS_2 Type-II heterostructure. **a.** The typical TMD device has a sample of interest (in this case a WSe_2/WS_2 heterostructure) 'sandwiched' between two (relatively thick, typically 20-50nm) hBN flakes. The sample is contacted by an FLG flake called the contact flake and a voltage V_c can be applied directly to the sample. Outside of the two hBN flakes are the gates, bottom and top, on which voltages V_b and V_t can be applied, respectively. **b.** Doping gate configuration. If the sample contact is grounded, and a sufficient equal positive (negative) voltage V_g is applied on the two gates, electrons (holes) are doped into the heterostructure. The symmetric gate voltages mean no electric fields are applied to the sample. **c.** Electric-field gate configuration. If the gate voltages are anti-symmetric, such that $V_b = -\alpha V_t$, where $\alpha = d_b/d_t$ compensates for different dielectric thicknesses, then an electric field $\vec{E}$ with $|E| = |V_b - V_t|/(d_b + d_t)$ is applied across the sample, with no doping.

2.3.2 Monolayer Effects: Electrostatic Doping and the Valley Zeeman Effect

Let us first consider the case when the sample of interest is a TMD monolayer, as seen in Figure 2.17a. Since the exciton is confined to a single layer, the out-of-plane electric field has no significant effect on the PL. Doping the sample with charge carriers, however, leads to the formation of a new particle species, the trion [80, 81]. Figure 2.17b shows that for symmetric gating, which introduces either e^- or h^+ carriers, the photoluminescence peak suddenly redshifts considerably (30 meV). This is the hallmark of the formation of a trion, illustrated in Figure 2.17c, which is an attractive bound state of an exciton with an itinerant electron or hole, a quasiparticle analogous to H^- or H_2^+ (insofar as the X is analogous to H). The $\sim$ 30 meV redshift therefore represents the binding energy of this state. The trion appears almost immediately as the sample is doped, as the relatively mobile electrons and excitons are able to diffuse and pair up efficiently. The range of voltages for which the neutral X (or X^0 for emphasis of neutrality) is dominant represents the range for which the Fermi energy is within the band-gap of the system. The effect of doping is observed both in emission and in absorption spectra of the monolayer, effectively red-shifting the excitonic band-gap by the binding energy. In fact, a more accurate term for the trion is an attractive polaron, as the entire Fermi sea of the doped electrons dresses the excitons [82].

The monolayer excitons also respond in an interesting way to an external magnetic field. As detailed in Section 2.1.4, excitons in the two different monolayer valleys couple to photons of opposite circular polarizations. Section 2.1.2 also details how the total magnetic moments of the electron and hole states that make up the exciton depend on the valley index and can be split into valley and orbital contributions. When a out-of-plane magnetic field $\vec{B}$ is applied, the excitons in the two different valleys become split [45, 83, 84, 85]. The energy of this splitting depends on the

total magnetic moment of the electron and hole comprising the exciton, and is often expressed as $\Delta E = g\mu_B B$. where μ_B is the Bohr magneton and g is called the Landé g-factor, in analogy to the atomic physics concept [86].

Figure 2.17d shows the different contributions to the electron and hole coupling to magnetic field via their spin, valley and orbital magnetic moments. Since K and -K points are time-reversed images, these contributions are opposite in the two valleys and lead to a different energy for the low-energy bright excitons. The key point is that the conduction and valence bands in the same valley shift by roughly the same amount from the spin and valley terms, while the orbital terms coming from the different atomic orbitals comprising the valence and conduction bands are negligible in the conduction band and contribute $\sim 2\mu_B$ each to the g-factor, as would be expected from the discussion in Section 2.1.2. While it qualitatively captures the salient features, this model for obtaining the g-factor is not exact, and the calculation of precise g-factors for each of the bands individually requires full treatment of the bands, taking into account effects such as the asymmetric effective masses of the conduction and valence bands [87, 88, 89, 90], an approach supported by experiments [86].

Figure 2.17e shows the experimental manifestation of the valley Zeeman effect [84]. Since the two valleys couple to photons of opposite circular polarizations, measuring the photoluminescence from the sample for only one circular polarization reveals the energy shift due to the magnetic field in the corresponding valley. The slope of the shift as a function of the magnetic field reveals a total excitonic g-factor close to 4, as expected from two valence bands splitting in opposite direction, each with a g-factor of 2.

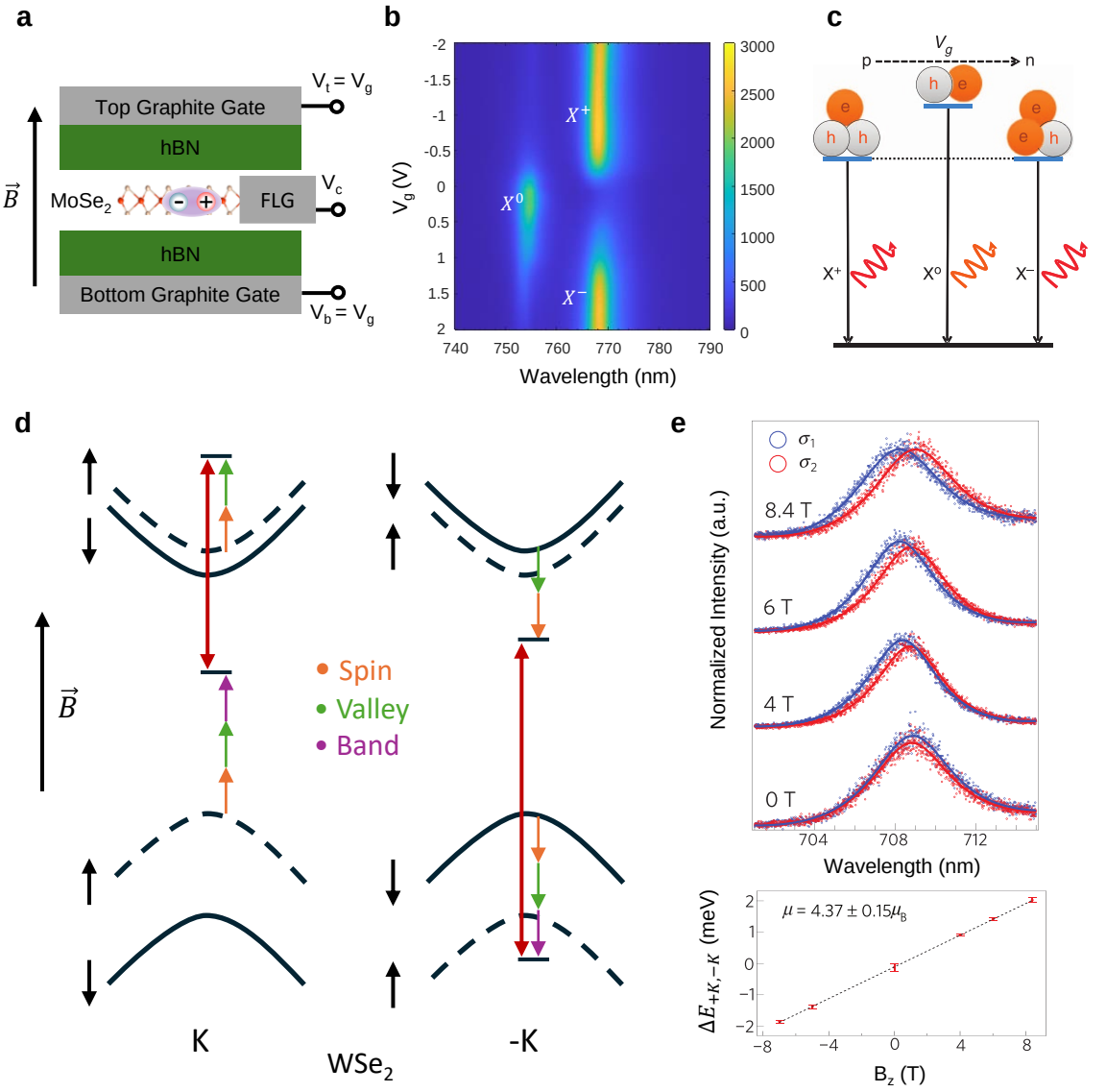

Figure 2.17: TMD Monolayer Doping and Valley Zeeman Effect. **a.** Monolayer TMD device with external magnetic field. **b.** Measured photoluminescence (PL) of the monolayer under doping. At charge neutrality we measure the intralayer exciton X^0, as well as the charged trions X^+, X^-. **c.** Sketch of the different exciton species as a function of doping. Figure adapted from [81]. **d.** Diagram of the valley Zeeman effect and the excitonic splitting under a magnetic field in monolayer WSe_2. In each band, the spin, valley and band contributions of the angular momentum cause an energy shift under a B-field in the same direction for the valence and conduction bands. However, while the spin and valley contributions are also of similar magnitude, the band contribution is much greater in the valence band, which causes the energy splitting between the K and -K excitons (red lines). Diagram not to scale. **e.** Measurment of the Valley Zeeman effect in monolayer WSe_2. The excitonic g factor is close to 4, as predicted from two times the band angular momentum of 2. Figure adapted from [84].

2.3.3 Excitonic Stark Effect

In the case of TMD heterostructures, the type-II band alignment between monolayers means that the exciton is an indirect interlayer exciton (IX). The IX has a static out-of-plane dipole moment $\vec{d}$, which readily couples to an out-of-plane electric field $\vec{E}$, as seen in Figure 2.18a. The energy by which the IX shifts is given simply by $\Delta E = -\vec{E} \cdot \vec{d}$. Figure 2.18b shows a E-field scan, done with antisymmetric gating, of a WSe_2/WS_2 heterobilayer with matching hBN thickness on either side (such that $\alpha = 1$). The energy shifts linearly with the voltage difference $|V_{tg} - V_{bg}|$ across the gates, which is expected from a simple capacitor model, where $|V_{tg} - V_{bg}|$ is proportional to the $\vec{E}$ in the sample. This coupling is called the excitonic Stark effect, and is the hallmark sign of the IX in type-II heterostructures. Because of the permanent out-of-plane dipole the IX carry, they can also intereact with each other. Figure 2.18c shows how, for larger excitation powers, and therefore greater IX densities, the excitons repel, blueshifting the emission. This can be understood in the context of the Stark effect as the IXs creating an internal electric field due to their layer separation, which blue-shifts any one IX.

The excitonic Stark effect can be used for precise tuning of IX emission energy, but also exploited more creatively. For example, Figure 2.18d shows an excitonic switch, where the Stark effect is used with patterned gates to create a high-energy barrier inside the sample, preventing IX diffusion [91, 93]. More careful patterning is able to produce gradients of $\vec{E}$ strength, which serves to control the IX drift, creating controllable IX currents, as shown in Figure 2.18e [92, 94]. These elements can be combined with the IX valley selection rules in order to create valleytronic circuits. Valleytronics is the concept of using the valley index of the exciton as an information carrier, and the possibility of routing IXs to make functional valleytronic devices is being actively investigated.

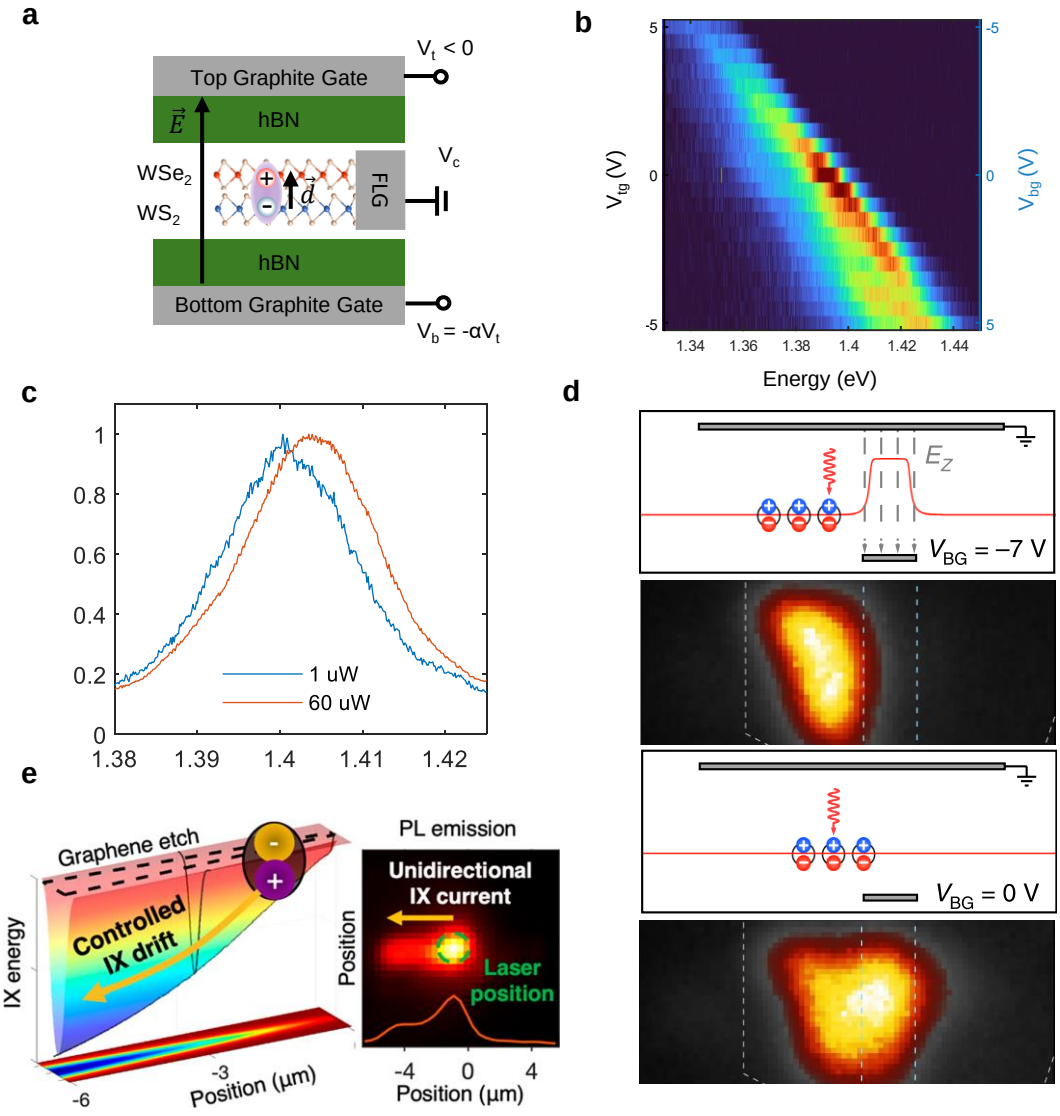

Figure 2.18: TMD Heterobilayer Stark Effect. **a.** Heterobilayer WSe_2/WS_2 device with external electric field. **b.** Stark effect measured in IX PL under external gating. **c.** Density-dependent shift from repulsive exciton out-of-plane interaction. **d.** Patterned gate as an excitonic switch. The Stark effect can be used as a barrier to exciton diffusion. Adapted from [91]. **e.** Patterned gate as an excitonic guide. Continuously modulated strength of the Stark effect allows for controlled IX current. Adapted from [92].

2.3.4 Heterostructure Valley Zeeman Effect

As is the case for the optical selection rules discussed in Section 2.2.3, the magnetic nature of IXs is more involved than the monolayer case. The basic principle is the same - since the high-symmetry points at which radiative exciton recombination occurs all violate inversion symmetry, just as the monolayer does, in momentum space there will be two time-reversed images made up of combinations of K points of each monolayer coupling to the photons. This means that, just as for the monolayer, there will be two valleys coupling to the photons, with opposite spin, valley and orbital contributions to the magnetic moment in the valence and conduction bands. Figure 2.19 illustrates two possible scenarios of alignment of the monolayer K points, in the R- and H-stacked case.

The mechanism is similar to the one discussed in Section 2.3.2, and indeed in the R-stacked case one expects a similar g-factor to the monolayer case, as shown in Figure 2.19a. Experimental evidence suggests this is indeed the case, with g-factors for WSe_2/WS_2 heterobilayers close to the monolayer value of ~ 4 [15], while heterobilayers of $MoSe_2/WSe_2$ have a g-factor of ~ 7, likely due to different sizes of valley moment contributions for the two materials [64, 62]. In the H-stacked case, the valley contributions for the two IXs are now opposite across the valence and conduction band, which for one valley moves the conduction and valence bands closer together, and separates them farther apart in the other, as shown in Figure 2.19b. This results in a significantly larger g-factor, with reported values of $\sim$ 10-12 in WSe_2/WS_2 H-stacked heterobilayers [15] and ~ 16 in $WSe_2/MoSe_2$ H-stacked heterobilayers [95, 64].

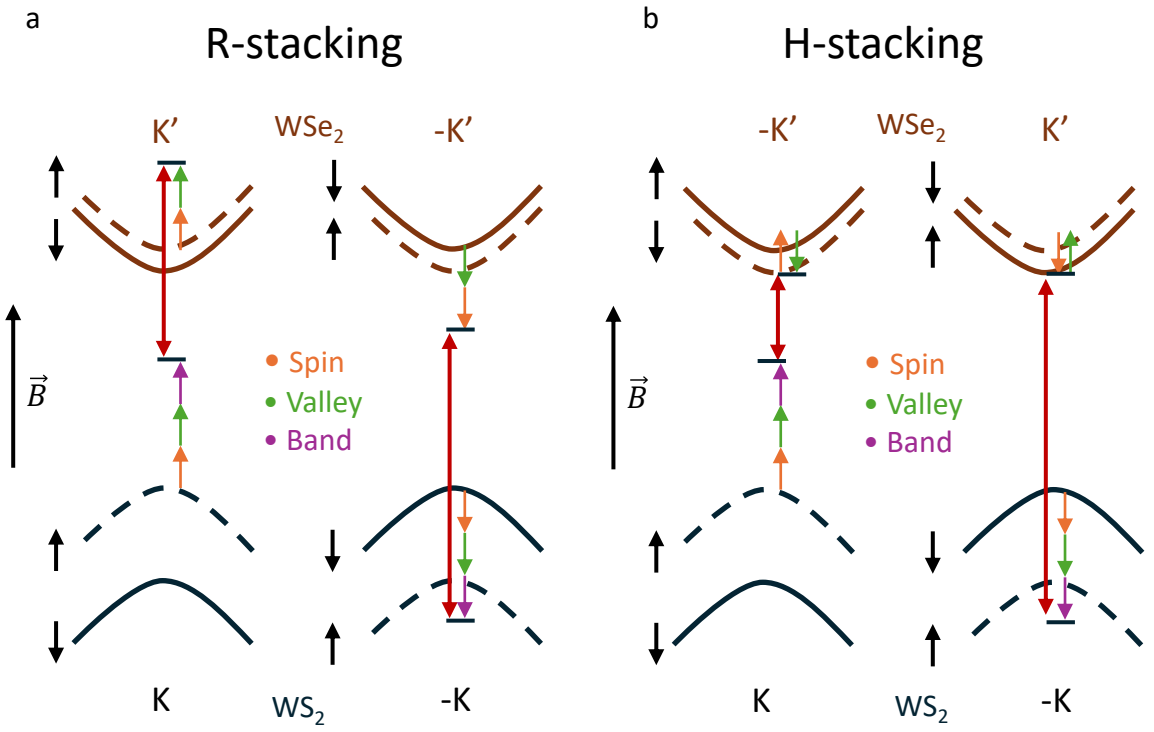

Figure 2.19: TMD Heterobilayer g-factor. **a.** Diagram of the valley Zeeman effect and the excitonic splitting under a magnetic field in R-stacked heterobilayer WSe_2/WS_2. In each band, the spin, valley and band contributions of the angular momentum cause an energy shift under a B-field in the same direction for the valence and conduction bands. However, while the spin and contributions are also of similar magnitude (though the valley contribution can differ for different TMD materials, such is the case for $MoSe_2$), the band contribution is much greater in the valence band, which causes the energy splitting between the K and -K excitons (red lines). The g-factor is comparable to the monolayer case. Diagram not to scale. **b.** Diagram of the valley Zeeman effect and the excitonic splitting under a magnetic field in H-stacked heterobilayer WSe_2/WS_2. In each band, the spin, valley and band contributions of the angular momentum cause an energy shift under a B-field, but the valley contributions are in opposite directions for the valence and conduction bands, due to the different monolayer valleys which are now momentum-aligned. The g-factor is now significantly larger than the monolayer case, as the valley contribution acts in opposite directions across the conduction and valence bands, and across the two species. Diagram not to scale.

2.3.5 Electronic Mott Insulator and Generalized Wigner Crystals

Taking a closer look at Figure 2.11, an interesting question arises - what happens in this system of interacting particles when their kinetic energy is substantially lower than the scale of the various interparticle interactions? Such a regime typically leads to new and interesting phases of matter, called strongly correlated phases. As this thesis will focus on such phases for excitons, let us examine the extant work on strongly correlated electronic phases in moiré systems. In analogy the the excitonic and electronic interactions shown in Figure 2.11, we can define an on-site electron-electron interaction U_{ee} and a long-range cross-site interaction V_{ee}.

Let us first examine the consequences of a strong U_{ee}. Figure 2.20a shows how U_{ee} leads to sequential filling of moiré sites under doping. As the electrons avoid residing in the same site, they first fill every available site, at which point an incompressible state forms, as the addition of subsequent electrons costs U_{ee}, which becomes an insulating gap [15, 14, 13]. This phase of matter is called a Mott insulator, a state which is not insulating because of the single-particle band-gap, but due to particle interactions. Now let us expand our consideration to finite V_{ee} as well. The cross-site interactions lead to the electrons assuming configurations that minimize this repulsion by reducing the mean distance between any two electrons. At particular filling fractions where these states are characterized by certain symmetries, such as the ones illustrated in Figure 2.20b, the electrons are also incompressible, as the change of position of any one other electron would violate the established symmetry and would increase the global energy of the system. These states are called generalized Wigner crystals, and have been widely observed in moiré heterostructures [13, 16, 17, 18].

As we saw in Section 2.3.2, the introduction of free charge carriers in monolayer can be optically detected, as the charges interact with the excitons in the systems to form trions, and more generally extended polaronic states. In TMD heterobilayers,

the presence of the Mott and Wigner insulating phases can be detected through these states, as the exact binding energy of the polaronic states is altered when an insulating state is formed. Though a quantitative description of this phenomenon is complex, it can be understood intuitively by considering that incompressible electrons are not able to dress the excitonic state as efficiently, and the polaron energy is expected to blueshift at such states. Furthermore, as these insulating states are gapped, small changes in doping voltage around the insulating states would lead to no change in the total electron density in the system, and therefore the excitonic absorption would remain constant for such small changes in voltage. Figure 2.20c,d shows differential reflectance spectra (see Section 4.2.4) of a laser tuned near the WSe_2 intralayer exciton resonance in a WSe_2/WS_2 heterostructure. The dips in the differential reflectance represent insulating states. The wide dip before the hole or electron doping begins is the charge-neutral intrinsic region where the Fermi energy is inside the band-gap of both materials. As the doping begins, small dips appear at the Wigner crystal fillings, with another broad minimum at half-filling of the moiré sites, which is the Mott insulator. The width of the minimum is a measure of the size of the insulating gap.

A central question of this thesis is how interlayer excitons organize in moiré potentials, and what kinds of phases can they realize as charge-neutral dipolar bosons, compared to the charged electrons and holes. As we will see, the excitons have their own analog of the Mott insulator and can also interact with the electronic Wigner crystals to form new kinds of complex particles. In the next section, we will introduce our sample fabrication techniques, in order to illustrate how to make TMD heterobilayer devices that host these exotic phases.

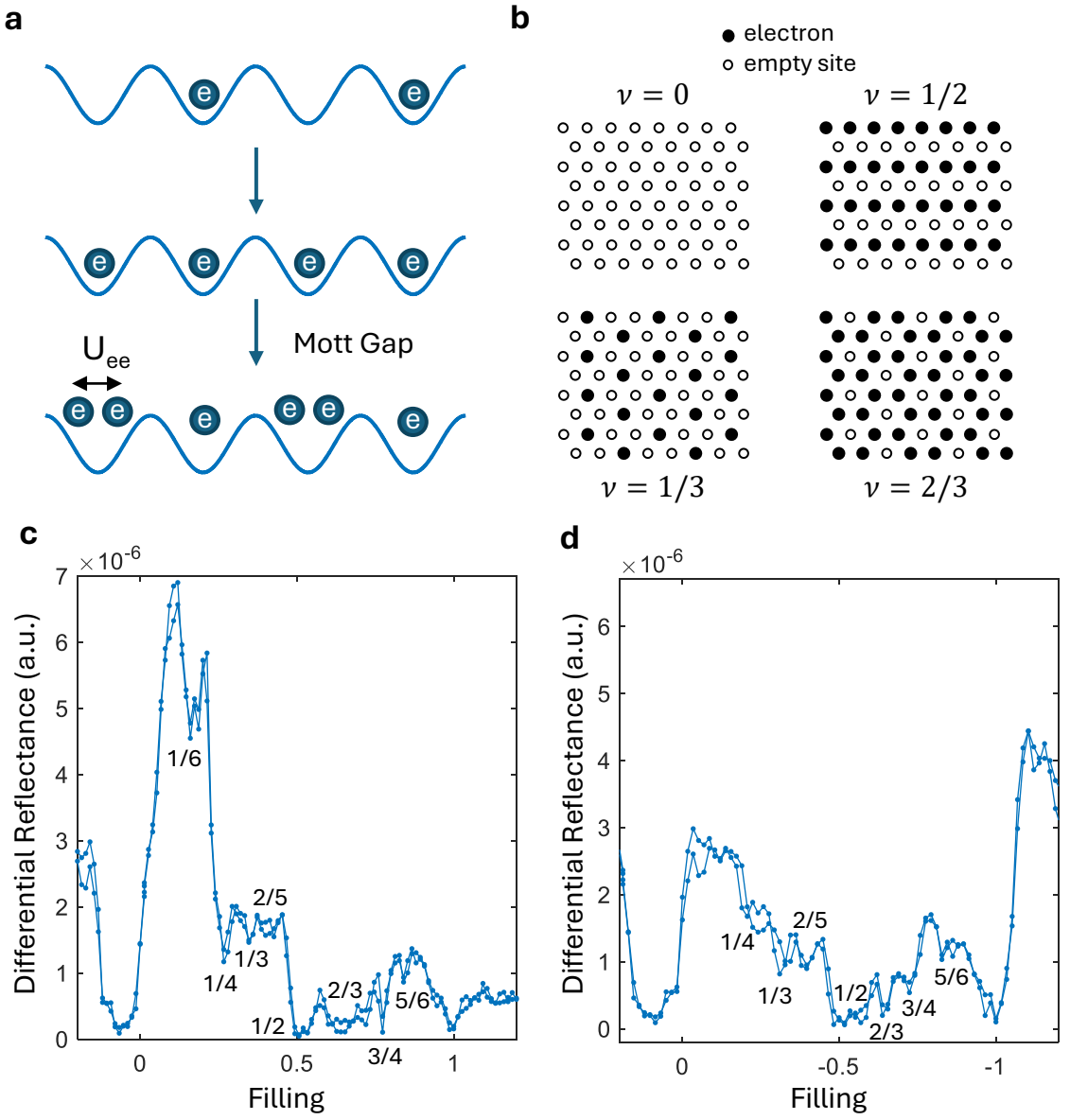

Figure 2.20: TMD Heterobilayer Mott Insulator and Wigner Crystals. **a.** Diagram of a electronic Mott insulator in a moiré system. **b.** Fractionally filled incompressible moiré states that minimize interparticle repulsion, termed generalized Wigner crystals. **c.** Differential reflectance measurement of generalized Wigner and Mott states. Electron-doped side. **d.** Differential reflectance measurement of generalized Wigner and Mott states. Hole-doped side.

Chapter 3

TMD Heterostructure Fabrication

Fabrication of reproducible, high-quality TMD heterostructures is a significant challenge that all researchers working in this field face. At the present moment, high-throughput deterministic additive fabrication methods on platforms such as CVD are still ineffective compared to manipulation of individual, pre-exfoliated flakes from bulk crystals. The primary constraint are the defect densities, which remain superior in bulk-grown crystals [96, 97]. The layer-by-layer methods presented here are based on the methods developed over the past decade [98, 99], and, as is traditional in semiconductor fabrication, include a fair amount of empirical best practices which are determined through a significant amount of trial and error. These techniques are rudimentary compared to the sophistication of GaAs and Si fabrication processes, and the success rate in fabrication decreases rapidly with sample complexity and total number of layers. We present here the methods we used, with the emphasis on the fact that these tools are constantly evolving together with the entire field of 2D materials.

3.1 Flake Exfoliation

3.1.1 Exfoliation of thin flakes on SiO_2 substrates

Step 1: Prepare clean silicon wafers. Our raw substrate was a heavily p-doped Si crystal, with a 300nm SiO_2 layer on top (University Wafer, 300nm Wet Thermal Oxide, Single-Side Polish, p-type, Boron dopant). In order to protect the clean side during the cutting process, we use a Nitto tape (Nitto, SWT 20+R) to cover the clean, polished side of the wafer, to protect it from dust during the dicing process. Then, with the use of a automated dicer (Micro Automation Model 1006) or manually by cutting with a diamond cutter, we made squares of $\sim$ 6 mm by 6 mm from the initial wafer. Once the cutting is complete, we removed the Nitto tape from the sliced squares, before placing them in a beaker of acetone to remove any tape adhesive residue. Next, the beaker would be covered by a tightly tied aluminum foil lid to prevent the acetone from evaporating and would be sonicated at 50°C in order to help the dissolution of the tape residue. Next, the wafer squares would be taken out and quickly (while still wet with acetone) transferred into a beaker of iso-propyl alchohol (IPA), before drying them with a nitrogen blow-gun. The IPA step help to dry the silicon without streaks, whereas directly drying the acetone tends to leave marks. Finally, the silicon substrates are oxygen-plasma cleaned at 30 s exposure, which burns off any remaining organic impurities and passivates the surface.

Step 2: Prepare tapes for exfoliation. Depending on the material, a tape with suitable material thickness must be prepared. This involves using an initial piece of bulk material and thinning it down sequentially using Scotch tape. A typical strategy is to press one side of a bulk crystal against a section on one side of a longer ($\sim$15 cm) piece of tape and remove it, which deposits a thick ($\sim 10^5$ - 10^6 layers) flake. The other end of the tape is then folded against itself to touch where the thick flake is. After making sure good contact was established, one peels off the other end,

which now has roughly half of the material. Making sure to stagger the pieces on the two sides, the sides are pressed again, such that the split flakes nearly touch each other so as to avoid blank space. Care must be taken not to press flakes against each other, as such grinding reduces the size of exfoliated flakes and leads unwanted sub-micron scale dust. This maneuver doubles the number of the flakes on either side of the tape to two, for a total of four flakes, each flake now with roughly a quarter of the starting material. High quality TMD and hBN crystals are typically less than 1 mm in size, so to cover a 6x6 mm silicon substrate, one needs to perform about 6 such doublings before having a square roughly 6x6 mm as well. This square tends to still be too thick for direct exfoliation and the two sides thus created are referred to as the 'mother' tapes. 'Daughter' tapes are created by pressing against the mother tapes and releasing, and they tend to have sufficient material to deposit a large number of flakes, without depositing only very thick flakes. The conditions of such tapes to achieve optimal exfoliation and the appearance of tapes that promise many flakes of a suitable size and thickness is estimated by eye, and practitioners tend to have empirical rules of thumb for particular materials.

Step 3: Apply and exfoliate tapes on substrate.

The prepared daughter tape is then applied on the substrate. Using a cotton q-tip, the tape was pressed against the substrate, eliminating all air bubbles inside. Making sure no sliding of the tapes occur, the pressure should be significant, to ensure good contact between the material and substrate. The substrates are then taped to a glass slide and placed on a a heater set to 100°C for 3-5 minutes. This step contributes to the good contact between the flake by helping eliminate gas pockets. The tapes are then removed, and after cooling slowly peeled off the substrate. The rate of peeling should be such that one substrate is peeled of in about 60s. This technique has been show to increase thin flake yield [100]. Once this step is completed, the substrates can be inspected for good flakes, which should have the proper thickness and sufficient

size to be integrated into a device.

3.1.2 Flake identification and selection

Once the exfoliation process is complete, the substrates are manually scanned for appropriate flakes. In the case of TMDs, these are typically monolayers, which can be recognized by their characteristic blue color against the silicon wafer. However, we can also use the PL of the monolayer we detailed in Chapter 1 to clearly distinguish the monolayers from bilayers, which can be difficult to do from color alone. Our microscope is equipped with a pair of filters - 550nm short pass for illumination and 650nm long pass for collection, which enable us to excite above the band-gap, but only collect the PL from the flakes. This has the additional benefit of enabling us to assess the quality of the flakes, as a uniform PL signal from across the flake indicates a uniform flake structure, whereas the appearance of hotspots might indicate structural defects [101]. In the case of graphene, flakes are chosen to be relatively thick to reduce resistance, but not so thick as to impede the PL signal from the device.

For hBN, the precise thickness is of particular importance, as the hBN flakes surrounding the monolayer TMDs can serve as a cavity which affects the optical properties of the encapsulated TMD flakes, as specified in Appendix A. This same property allows us to confirm the flake thickness when it is exfoliated on the silicon substrate, as a single hBN flake itself can serve as a cavity, with light reflected off the top and bottom interfaces interacting constructively or destructively with the incident light. This is essentially a thin-film interference effect, and as such is wavelength-dependent, since the difference in path length over the thickness of the flake leads to a wavelength-dependent phase difference. This leads to hBN flakes having a thickness-dependent color under white light illumination, which can be calibrated against AFM measurements for a reliable optical identification of thickness, as shown in Figure 3.2. Such a calibration should be done at each particular microscope, as the details of the

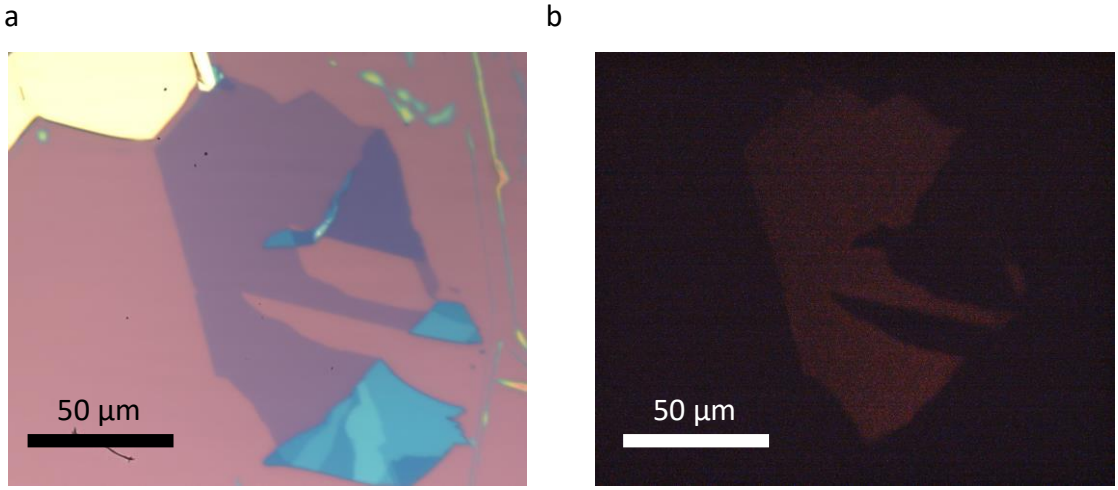

Figure 3.1: Exfoliated TMD Monolayer Photoluminescence. **a.** A particularly large monolayer of WSe_2, brightfield image. Monolayer is surrounded by thicker pieces. **a.** Using a 550 nm short-pass filter on the illumination arm and a 600 nm long-pass filter on the collection arm, we see the efficient PL only in the monolayer region.

illumination and objectives affect the calibration substantially.

After identifying the flakes, images are taken at varying degrees of zoom, in order to facilitate sample design and locating the flake in the future by referencing it against the position of other, larger exfoliated flakes at landmarks.

3.2 Heterostructure Stacking

In this section, we will specify how exfoliated flakes are combined into functional devices. Firstly, we turn to the fabrication of patterned substrates, which have defined electrical contacts for the sample, and then to the process of stacking the layers and depositing them onto the patterned substrate.

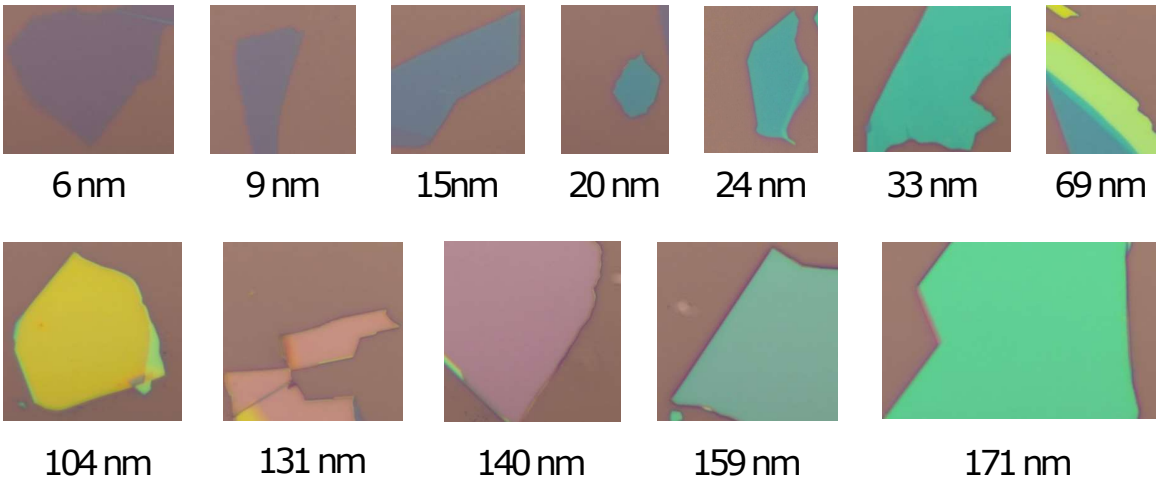

Figure 3.2: hBN Thickness by Color. h-BN flakes exfoliated on 290 nm SiO_2 on Si, full microscope lights, 60 ms, 100x, all other camera settings default. hBN thicknesses were determined by AFM.

3.2.1 Patterned Substrate Fabrication

The primary method for our substrate fabrication is electron-beam lithography (EBL). Since the patterned substrates are made in relatively large quantities, photolithography is also a good option, but our demand for prototyping different sample designs and accommodating flakes of various sizes led us to primarily use the more precise but time-consuming EBL. The steps in creating a substrate are the following:

Step 1: Create a drawing in the appropriate CAD software. The design should include a serially decreasing feature size, with large bonding pads on the side where wirebonding will be done to contact the leads to outside equipment. A series of decreasing-size pads is also present, as backups in case the larger pads are damaged and to assist in navigating the sample once loaded into the cryostats. Figure 3.3 illustrates a typical design.

Step 2: Spin coat the substrate. Clean 6x6 mm substrates (the same used for exfoliation in Section 3.1.1) are placed on a spin coater (Laurell WS-400-6NPP). The coating applied is of two resist layers - first an MMA layer, followed by a PMMA layer. Since MMA is a 'weaker' resist that is more susceptible to damage to electron

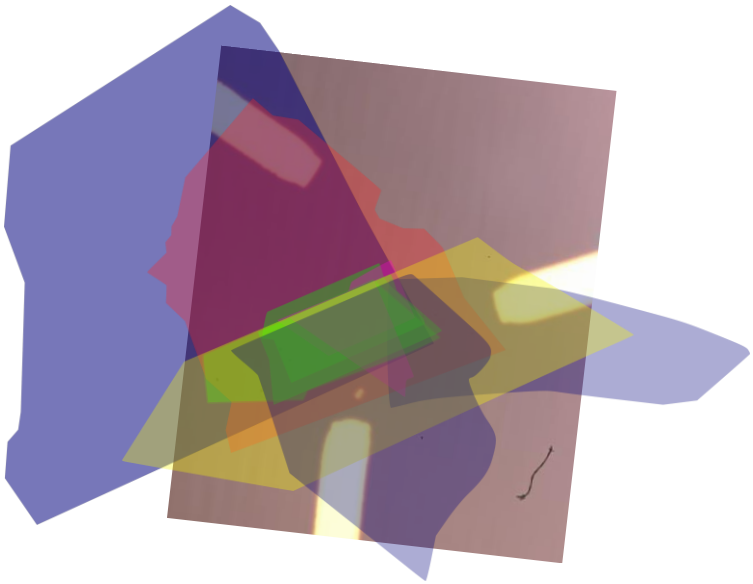

Figure 3.3: Typical Stacking Plan. Over a bright-field image of the substrate with leads are overlayed the flake positions. Blue flakes are graphene, red and yellow bottom and top hBN, and the green and pink flakes are TMDs.

exposure, this kind of two-layer structure allows for an 'undercut' – a situation where the top layer will have smaller feature sizes than the bottom after exposure and development. This allows for an easier lift-off, which is the process of removing PMMA and MMA and only leaving the deposited metal, as the metal would not directly contact the polymer. Both MMA and PMMA were spin coated at 4000 rpm, which makes an $\sim$ 100 nm MMA layer with a 200 nm PMMA layer on top, which is greater than the $\sim$ 80 nm lead height we intend to deposit. After each coating, the substrates are placed on a 100°C hotplate for 1 min to dry the polymer layers.

Step 3: Electron-beam exposure.

The coated substrates are placed in the electron microscope (Zeiss EVO 35) and secured with set-screws. The sample chamber is evacuated and the beam is initialized according to standard protocol, including calibrating the beam current in a Faraday hole, with larger features ($>$ 200 nm) using 100 pA specimen currents and smaller features using 15 pA. The position of the beam is placed in the center of the substrate, taking care to use a small current, low zoom and brief exposures in order to minimize

the exposure of the resist. The CAD file created in Step 1 is uploaded to the EBL software, which turns the design into a set of instructions for the electron microscope control module. The commands are then executed, delivering a typical area dose of 100-300 μC/cm^2. The polymers under irradiation undergo scission, making them significantly more soluble than the unexposed polymer. The substrates are then removed from the microscope.

Step 4: Develop the resist.

After the exposure, the resist is placed in a solvent composed of 1:3 ratio of MIBK (Methyl Isobutyl Ketone) and IPA (Isopropyl Alcohol) for a brief period of $\sim$ 15 s, before quickly transferring to IPA alone and drying with a nitrogen gun. This selectively dissolves the exposed polymers, leaving behind the desired pattern as a series of holes in the polymer layer.

Step 5: Deposit the metals.

The developed substrates are then placed in a thermal evaporator facing the crucibles, with two different crucibles with different metals loaded - chromium and gold. The evaporator is equipped with a metal stop which between the crucibles and the substrates. The evaporator is evacuated and a high current ($\sim$ 1-3 A) is run through the crucible to melt the metal and begin evaporating. A quartz scale is located near the substrates. When the stop is removed, metal vapor rises from the crucible and is deposited onto the substrates, with the quartz scale measuring the deposited amount. We typically deposit 5 nm of chromium as a wetting layer, since it has good adhesion onto silicon oxide, followed by 75 nm of gold. This makes 80nm tall wires, which is a sufficiently tall profile to reduce the resistance and make good contacts to the flakes.

Step 6: Lift-off of the polymer mask. Finally, the PMMA/MMA mask needs to be removed. This is typically done overnight under acetone, with gentle stirring or sonication to accelerate the PMMA/MMA dissolution and the removal of the thin gold film on top of the mask.

3.2.2 Polycarbonate-based dry fabrication method

The predominant fabrication method of TMD heterostructures at the time of writing is the polycarbonate (PC) based dry transfer method, in which a sacrificial layer of the polymer PC is used to pick up the flakes one by one and is then melted off onto the patterned substrate together with the sample, where it is subsequently dissolved away [98]. This method is fairly reliable in picking up the flakes, but must be performed carefully in order not to damage them or induce excessive unwanted strain in the sample. A great advantage of this approach is that only the topmost flakes are in contact with the PC directly, which tend to be the protective large hBN flakes, thereby preserving a clean interface between the TMDs, which is the most sensitive part of the sample. The procedure presented here, as with everything in this section, includes many empirical rules of thumb and best practices developed through trial-and-error.

Motorized Stacking Setup

In order to fabricate the samples, we need to have nm-scale precision in positioning the flakes relative to one another. Such precision can only be achieved through a motorized setup, with precise motors moving and rotating the substrate and sample relative to one another, and with an integrated microscope to guide the fabrication process. For this purpose, we designed a custom setup that integrates 50 nm step size motors (Zaber LSM Series Motors) with a 4 μrad step size rotation stage (Zaber RSW) into a microscope, as shown in Figure 3.4. The setup consists of a sample stage, which is mounted on translation and rotation motors, and a slide arm, which holds the glass slide used to manipulate the flakes, and can only translate. The sample stage itself is a copper piece with an integrated insertion heater, which is controlled by a PID controller. The sample stage is heated both for pickup of new flakes by the slide arm and for drop-down of the completed sample by melting the PC. The setup is controlled by a custom made LabView program, which allows for

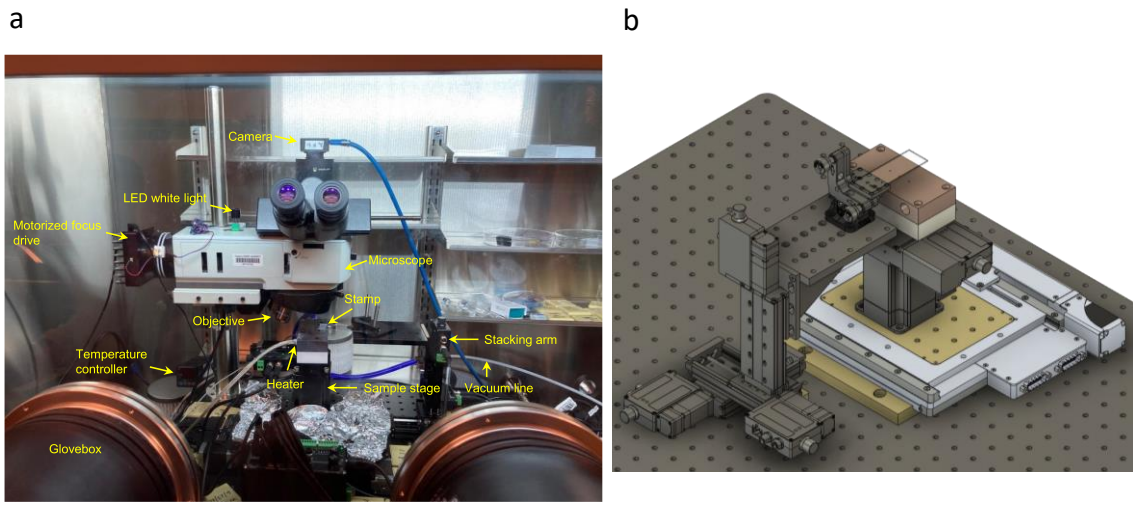

Figure 3.4: Stacking Setup. **a.** Photograph of setup with components labelled. **b.** CAD design of the stamp arm and sample stage.

precise movement of every degree of freedom. Above the sample stage, there is a microscope with an adjustable zoom by selection of 5X, 10X, 20X or 50X objective in a motorized nosepiece. The focus of the microscope is likewise motorized, which allows us to focus on the sample stage or the slide arm as needed. The entire setup is placed inside a nitrogen-filled glovebox, in order to minimize oxidative damage to the flakes, especially when they are exposed to higher temperatures. The copper piece also has three 1 mm diameter holes on the top that are connected to a high-temperature-resistant vacuum line, which creates a vacuum chuck for the samples, fixing them to the copper piece for good thermal contact and stability.

Stacking Design

Using the images taken when identifying suitable flakes, we trace out the edges of good candidates in am open-source vector graphics design software (InkScape). Then, the flakes are placed in appropriate positions for the desired sample. A careful stacking plan is of the utmost importance in making a viable sample, especially as flakes may shift during the process, and good, clear drawings can be edited on the fly to

compensate for these factors.

There are a significant number of principles that need to be obeyed for a successful sample design, and we will list them in no particular order here:

1. *Tolerance for error.* As flakes tend to shift when picked up, it is important to leave large margins for error whenever possible. For example, hBN flakes should be substantially larger than the TMD monolayer being picked up, so that plentiful room is afforded on each side when possible, rather than relying on very similarly sized flakes aligning precisely. Graphene contact areas should also be made particularly large when possible, so that deviations still lead to reasonable contact resistances. Lastly, one should always have backup flakes, particularly for the initial steps of picking up a flake directly with PC and picking up an hBN flake with graphene, as they tend to have the highest failure rates.

2. *Minimizing risk of short circuits.* All graphene flakes should be separated by at least 20 nm think hBN and should never be near each other, or near an hBN edge (other than the side that they contact the metal leads). This is particularly important in tear-and-stack samples, where TMDs are picked up by the edge of the hBN and a graphene gate must also come close to that same edge to maximize the area of the TMDs that are gated. At least 1-2 μm of distance should be left between the graphene and the hBN edge, to avoid a gate-TMD short.

3. *Aligning 'blind'.* As the thickness of the sample grows with each new flake, it becomes difficult to see the next one directly through the stamp and the already picked-up flakes, particularly seeing monolayers through thick hBN flakes. In this case, landmarks around the target flake must be used for alignment, which are typically plentiful very small flakes that are commonly left on the surface or a part of the same flake being picked up which is thicker and of no interest. Reducing the magnification to 20X as opposed to the 50X one would use for the highest precision also allows for greater imaging contrast of the target flake.

4. *Direction of stacking.* As the stamp is circular, it makes contact with the substrate in a radially symmetric way, creating a growing circle of contact between the PC and the substrate. This means that the flakes should be aligned with their long side pointing radially away from the stamp center, so that when the flake is being picked up, the contact front can slowly and in a controlled fashion move across the flake. This is particularly important for tear-and-stack, where the hBN edge must make contact with the portion of the TMD flake being picked up, but the PC must not be allowed to contact the TMD part being saved for the next pickup, lest it contaminate the surface.

5. *Proper hBN flake choice.* The hBN flakes must be very flat and uniform in thickness to serve as good platforms for the TMD flakes. Also, they must have no cracks or defects, to maintain good electrical insulation of gates from the TMDs. As mentioned before and detailed in Appendix A, proper thickness choice is very important to obtain good reflectance signals from the TMDs.

6. *Gated contact regions.* In order to efficiently dope the system, it is important that the region where a contact graphene touches the TMD flakes is also covered by the gates. In this way, when the gate voltage is increased, free carriers are introduced into the contact region, making the local graphene and TMD more conductive and facilitating the minimization of the Shottky barrier.

7. *Independent TMD contacts.* In our samples, we always contact as many TMD layer separately by the contact graphene as possible, rather than only rely on doping one TMD layer through the other TMDs. In this way, more layers have a comparable Shottky barrier and no significant transient potential differences across the neighboring layers are introduced.

Stacking Procedure

Firstly, we make the stacking stamp, with the following procedure:

Step 1: Prepare the PDMS domes. PDMS is typically purchased as two liquids (Sigma-Aldritch Sylgard 184), with DMS base and a curing agent. The DMS is mixed with a cross-linking agent that initializes the polymerization. When mixed, the liquid PDMS base slowly becomes stiffer and after drying forms into a elastic gel-like solid. To make the domes, the base and curing agent are thoroughly mixed, and then deposited as a droplet near the edge of a glass slide. The slide is then rapidly flipped and placed into a 120°C furnace on a stand, such that the droplet is free to sag under gravity into a convex shape. The placement into the furnace must be quick, so as not to allow time for the droplet to drip off the glass slide. Once the first droplet is cured, another is added on top of the first to enhance the curvature, and cured in the same way as the first. The PDMS domes can be reused indefinitely, and tape can be used to clean their surface of dust.

Step 2: Prepare the PC films. The PC is purchased in the form of pellets, which need to be dissolved in chloroform with a 6% PC concentration by weight. The dissolution should be done with a magnetic stir bar, and the PC takes about 48 hr to dissolve homogeneously. Such a solution is stable for years and can be reused. Then, prepare two clean glass slides by cleaning them with acetone then IPA and scrubbing with a low-lint wipe (KimTech) for each solvent. When the slides are dry, several drops of PC solution are applied on one slide, and the other is quickly pressed against it, making the PC solution evenly distributed without bubbles. Next, the slides are slid laterally in a uniform motion, which leaves a uniform thin PC film on both slides. The slides should dry for a few minutes before use.

Step 3: Prepare the PC stamp.

We cut a square hole significantly larger than the PDMS dome from Step 1 in a piece of tape. Next, the tape is applied to the PC film from Step 2. We use a razor to cut the PC around the edges of the hole in the tape, as well as around the outer edges of the tape. Then, the tape is lifted, leaving an isolated PC square. Using a

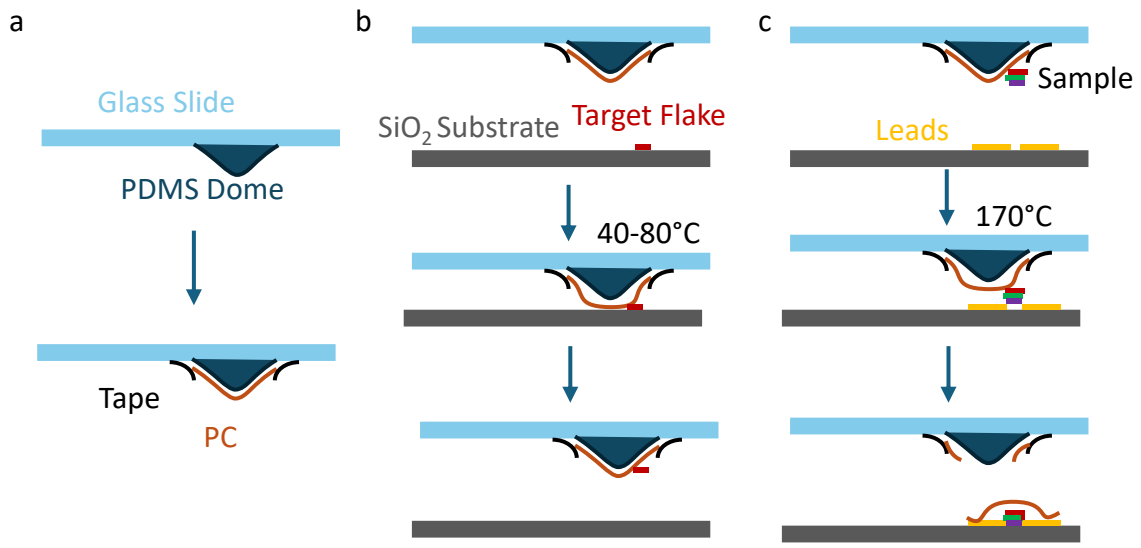

Figure 3.5: Pickup Procedure Sketch. **a.** Making a PC stamp. **b.** Picking up a flake. **c.** Dropping a completed sample down onto patterned leads.

hole punch, we punch a hole roughly the size of the PDMS dome in another piece of tape, and use it to pick up the PC square, such that the hole is centered on the larger square and the edges of the PC square adhere to the tape. Now we carefully lift off, yielding a hole in the tape completely covered by PC. This region is then applied to the PDMS dome, creating a structure as shown in Figure 3.5a. The stamp is then inspected under the microscope to ensure no dust is present, as dust particles can interfere with the pickup process.

Next, the glass slide with the stamp is loaded into the glovebox and onto the stacking arm motors. Now, we are prepared for the stacking process, which proceeds as follows:

Step 1: Touch stamp to clean substrate.

Firstly, the stamp is briefly contacted to a clean substrate at ambient temperature, in order to determine the position of the stamp center. This allows for better planning of the position of the sample relative to the center, which should be offset sufficiently that the initial contact of the stamp to the substrate does not immediately reach the target flakes, so as to maintain control of the approach.

Step 2: Pickup of first flake. Now the InkScape drawing is scaled on the screen to a right size relative to the camera image at the desired magnification, and the first flake target position is drawn in. Then, the target flake is oriented and positioned using the rotation and translation stages in the correct position. The first flake is typically a graphene or hBN flake, and is picked up at a temperature of 80°C, which makes the PC slightly more sticky and facilitates a clean pickup. The drawing is always overlaid on the microscope image, in order to correct continuously as the stacking arm makes its approach. The flake is crossed with the contact front slowly, using a 100 nm/s speed on the slide arm z-axis to make the approach and pausing if necessary to ensure no air bubbles are trapped between the PC and the flake. The flake is kept for several minutes in contact before the stamp is retracted. A change of color of the flake upon the from reaching it is indicative of a successful pickup - in the event that it does not immediately occur, temperature is incrementally increased up to 120°C until the flake picks up.

Step 3: Pickup of second flake. Using the same procedure as above, we pick up the second flake. In the case of the bottom gate, the first flake picked up was hBN, followed by graphene. In the case of the top gate and sample, the first flake is graphene, followed by hBN. For both cases, a temperature of 80°C is appropriate for both steps. The bottom gate procedure is complete at this step, whereas the top gate hBN will now be used to pickup the TMD monolayers and form the sample itself.

Step 4: Pickup of subsequent flakes. At this step, the TMDs are picked up in the same way, followed by the contact graphene. The temperature for these steps is kept low (40°C), as the adhesion of the TMDs and graphene to the hBN which is being used to pick them up is considerable, and the low temperature minimizes risk of damage to the sample and introducing strain from lateral forces of the PC sticking to the substrate that might alter the moiré potential.

If the tear-and-stack technique is used, then one of the pickup steps will involve

pickuping up only part of the flake using the edge of the top hBN, making sure the contact front does not go over this edge, so that PC never touches the TMD flake being cut. Only the part under the hBN will pick up, leaving a clean cut underneath. Since the tear-and-stack technique is used in order to guarantee precise angle alignment, as the use of the same flake guarantees that their crystallographic axis is the same, it is important to only use the precise rotational motion of the motor for subsequent steps, and note the target absolute position of the rotation stage for the second pickup of the same flake immediately after the first is picked up, to ensure minimal error in the relative angle of the two pieces of the same flake.

Step 5: Drop-down. Once the sample is complete, it needs to be deposited onto the substrate. Firstly, the bottom gate/hBN structure is deposited directly onto the patterned substrate into the appropriate position. The alignment and approach method are as before, but the temperature upon approach is increased to an initial 140°C. Great care must be taken in approaching the correct position at these temperatures, and the approach should be as quick as can be safely done, to avoid the PC heating to displace the flake from the target position. Still, the approach must be smooth, such that minimal air bubbles are introduced. When the sample is firmly in position and in good contact with the surface, the contact front is pushed significantly out and the temperature increased to 170°C. At this temperature the PC begins to melt, and a sudden rapid jerk of the sample arm upward induces first delamination of the PC from the PDMS dome, followed by a complete tear, depositing the sample and the part of the PC stamp in contact onto the patterned substrate. Then, the stage heat is shut off and the substrate with the bottom gate is placed overnight under chloroform, to dissolve the PC film. Next, the sample is placed in a furnace and annealed under a flow of 5% H_2/ 95% N_2 gas at 350°C for 3 hours, which adheres the bottom gate and hBN well to the substrate and removes any PC residue. The method for the top gate/sample drop-down is the same, but it is dropped onto the

bottom gate and no annealing step is done, as the PC contamination is outside of the sample region and the sample might undergo changes at such high temperatures.

Sample Mounting

Once fabricated, the sample needs to be mounted onto an appropriate chip carrier, which allows for mounting into the cryostat and with electrical leads which allows us to connect the sample to our apparatus. The procedure is as follows:

Step 1: Create chip carrier and mount the sample. The chip carrier consists of a copper piece (high-vacuum grade copper) with a printed circuit board (PCB) attachment, as shown in Figure 3.6. The PCB (Attocube ASH/PCB/12) has leads with pads near the sample for wire-bonding to the sample directly, as well as away from the sample on one side for soldering wires to connect to our equipment. The soldered wires for connection to the equipment are attached before the sample is mounted. A layer of sapphire crystal (Al_2O_3) is attached on top of the middle of the copper piece using G-varnish. This layer serves to provide electrical insulation from the copper. The sample is mounted on top of the sapphire layer using silver paste, which ensures good thermal contact to the piece.

Step 2: Wire-bond the sample. The wires fore equipment connection are going to now be connected to the sample, and must therefore be grounded to a good common ground to avoid sudden potential differences across the sample due to static electricity. A good choice is are shorted screw terminals, which ensure a tight connection. The carrier chip with sample is then taken to a wire-bonding machine (West Bond 7476E) and the pads on the substrate are connected to the carrier pads using 1 mil gauge aluminum wire. Care must be taken during the bonding to avoid touching the sample.

Step 3: Load the sample into the cryostat. The sample is now ready to be loaded into the cryostat. The common ground of the chip wires is also grounded to

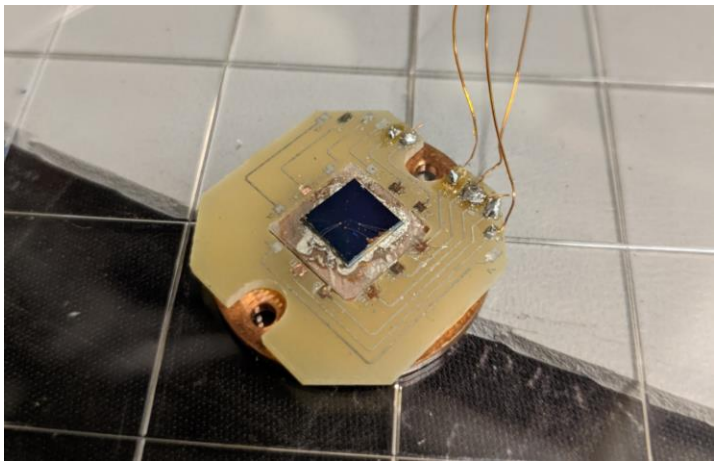

Figure 3.6: Completed Sample. Photograph of a completed, mounted sample after wire-bonding, ready for loading into a cryostat.

the cryostat lead ground. Using carbon-tipped tweezers, the wires leading to each gate and the contact are recorded by their chip number and carefully removed one at a time from the grounding screw terminals and placed into the cryostat terminals, taking care not to touch the metal part of the wire pin with the tweezers. The number of the cryostat terminal corresponding to each sample lead is recorded. A small (toothpick-tip) amount of vacuum grease (Apeizon Cryogenic Vacuum Grease) is applied on the back of the copper piece and spread evenly with a toothpick to ensure good thermal contact between the copper and the cryostat cold braid.

Now the sample is ready to be cooled down and measured, using the techniques we will outline in the following chapter.

Chapter 4

Optical Measurements of TMD Heterostructures

As we saw in the preceding chapters, one of the most appealing properites of monolayer TMDs is their optical response. Therefore, a wealth of information about the system can be gained by optical measurements alone, down to the microscopic arrangement of electrons inside the moiré lattice. In this section, we will introduce our apparatus and experimental procedures that were used to obtain the data in subsequent chapters.

4.1 Measurement Setup

In order to measure the optical properties of any material, one needs to illuminate the material with some light of known structure (color spectrum, polarization) and collect the reflected or re-emitted light (after absorption) back. The illumination light and the apparatus used to deliver it to the sample is commonly referred to as the excitation and 'excitation arm', respectively. The light coming off the sample is the collection light, and the relevant apparatus is accordingly the 'collection arm'. Since the physics of quantum phases we are interested in has relatively modest energy

scales, we need the sample to be at low temperatures in order for these phases and effects not to be dominated by thermal motion. Therefore, our samples are loaded in cryostats which can reach temperatures as low as 3-4 K. Therefore, our optics setup needs to be designed around the cryostats, with all of the optical treatment and modification of the excitation and collection beams occurring outside of the cryostat. We will describe the two experimental setups used in our work and named after the cryostat brands - 'Bluefors' (Bluefors BF-LD 4K) and 'Attodry' (Attodry 800). The Bluefors cryostat is equipped with an ± 8 T magnet, which applies a magnetic field out-of-plane of the loaded sample. The basic architecture of these two setups is the same, with some differences in the precise details of the construction.

4.1.1 Setup 1 - 'Bluefors'

The design of the Bluefors optical measurement system is laid out in Figure 4.1. On the excitation arm, we fiber-couple different light sources: white light sources with strong intensity near the monolayer TMD resonances for reflectance measurements, a tunable continuous-wave (CW) titanium-sapphire (Ti:S) laser (MSquared SolsTiS) with a range of 700-900 nm, used for photoluminescence (PL), photoluminescence excitation (PLE) and differential reflectance measurements, and a pulsed 640 nm laser (PicoQuant LDH-D-C-640) used for lifetime and time-resolved PL measurements. The fiber-coupled beams are then mated to another fiber which is out-coupled and routed towards the sample, enabling us to efficiently adjust the excitation at the mating joint without disturbing the alignment of the optical setup.

On the excitation side, we control the total power of the excitation via different means: white light sources come with integrated intensity modifiers, but the power is usually set to a fixed value, as reflectance measurements are done at constant power to keep the same reference spectrum valid. The laser intensity often needs to be controlled more precisely, especially when investigating exciton density-dependent

effects. For this purpose, we use a $\lambda/2$ wave-plate followed by a polarizing beam splitter (PBS) cube and a tunable ND filter in the case of the Ti:S laser and a linear polarizer in the case of the pulsed laser. The Ti:S laser has a power output of 5W, making the first stage of power reduction with a PBS cube necessary, which operates reflectively and diverts excess power to a sink. Next, an absorptive ND filter is used for fine-tuning the power. In the case of the pulsed laser, the maximum power is a much lower 50 mW (when operated in CW mode), making a $\lambda/2$ wave-plate followed by an absorptive linear polarizer a sound choice. The $\lambda/2$ wave-plate was mounted on a motorized rotary stage (Elliptec ELL14K), which allowed for automated power adjustment.

The excitation beam is out-coupled into a short-pass filter, in order to remove any light created by nonlinearities inside the fiber in the same range as the signal of interest. Next, the beam encounters a $\lambda/2$ wave-plate, which can rotate the linearly polarized beam to align with the following linear polarizer to maximize power throughput. The linear polarizer is aligned to the slow axis of the full-plate liquid-crystal retarder (LCR, Thorlabs LCC 1513-B) that follows. An LCR is esentially a wave-plate with a voltage-controlled retardance, meaning that, when linearly polarized light is incident on the slow axis, the LCR can modify the beam to arbitrary linear or circular polarization, with the retardance/polarization pairs given in Table 4.1.

Table 4.1: LCR Output for Different Retardances. The two orthogonal linear polarizations are labeled with $l_{1,2}$ and the RCP and LCP circular polarizations with $\sigma_{1,2}$.

Retardance (δ)	Output Polarization
0	l_1
$\lambda/4$	σ_1
$\lambda/2$	l_2
$3\lambda/4$	σ_2

The light, now with a well defined polarization, is incident on a 50/50 beam

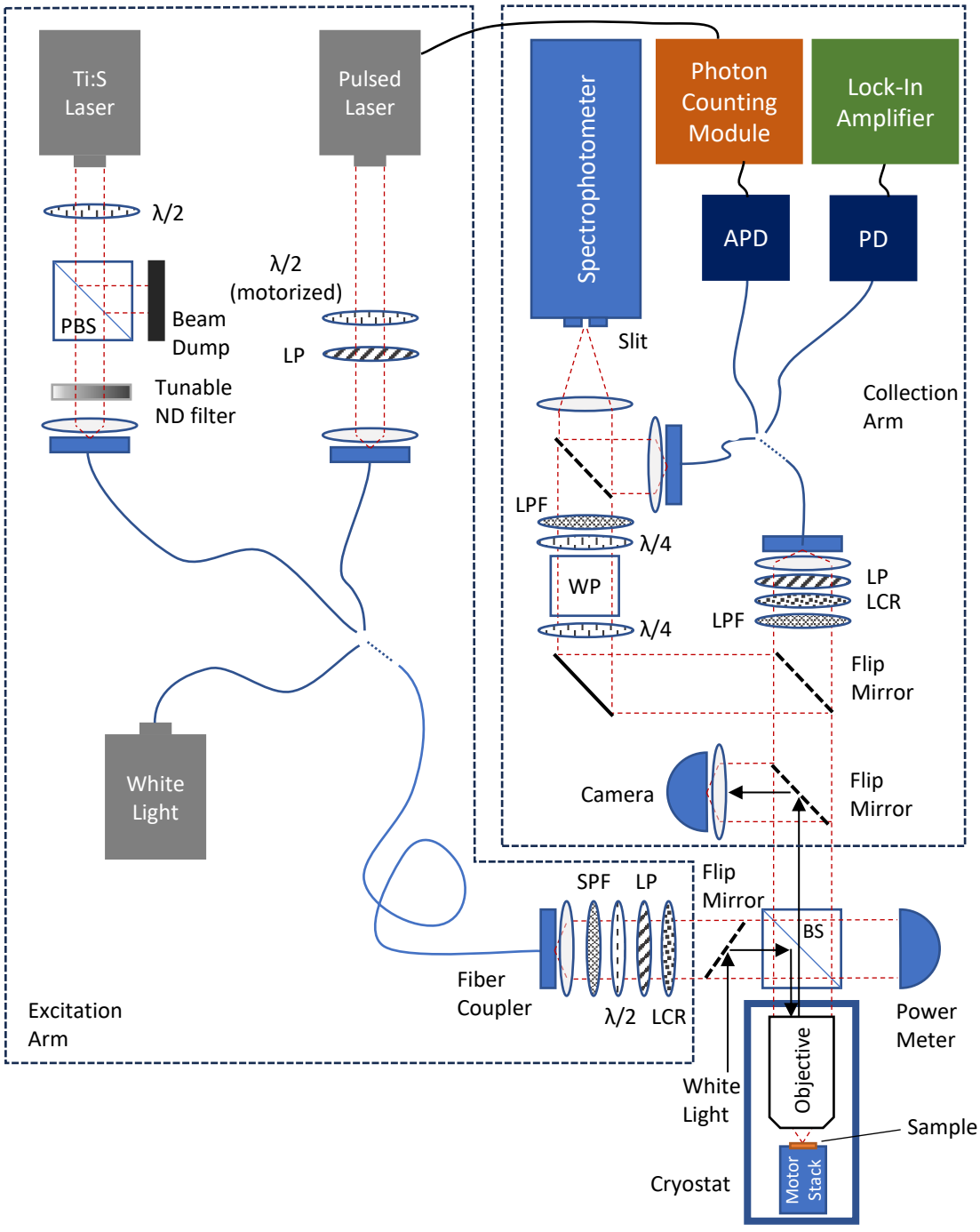

Figure 4.1: Optical Measurement Setup Diagram. Legend: BS - beam splitter (50/50); PBS - polarizing beam splitter; $\lambda/2$ - half-wave plate; $\lambda/4$ - quarter-wave plate; LP - linear polarizer; SPF - short-pass filter; LPF - long-pass filter; LCR - liquid-crystal retarder; PD - photo-diode; APD - avalanche photo-diode; WP - Wollaston prism; ND - neutral density. Mirrors ommitted for clarity.

splitter, with a power meter on one branch to monitor the incident power and the other arm going into a glass window on the cryostat and into the objective. In the case of the Bluefors setup, the custom achromatic Mitotoyo objective (NA = 0.63, f = 4 mm) is mounted inside the cryostat. The objective focuses the excitation light to a ~ 1 μm diameter spot.

The emitted light is collected by the same objective and can go to one of three collection branches. In the first option, the light is routed through a long-pass filter to remove the excitation light, after which it goes through the same LCR/linear polarizer setup as the one described for the excitation arm in order to define the collection polarization. The light is then fiber-coupled, and can be sent to different measurement apparatus: a spectrophotometer for spectral analysis or an avalanche photo-diode (APD) for photon counting, for example, as shown in Figure 4.1.

In the second case, using a flip mirror, we can route the light into the spectrophotometer without fiber-coupling it (free-space). In this case, the light passes through a $\lambda/4$ plate, a 2° Wollaston prism, and back through a $\lambda/4$ plate. Since the Wollaston prism separates the light by linear polarization by refracting the two polarizations with 2° difference in directions, the inclusion of the $\lambda/4$ plates mean that this sequence creates a 2° separation of the light of σ_1 and σ_2 polarization coming from the sample. The Wollaston prism is aligned such that the separation is vertical. The collimated light is then focused by a lens onto the entry slit of a spectrophotometer (Princeton Instruments SP-2750), where the two circular polarizations are vertically separated on the collection CCD (Princeton Instruments PyLoN).

In the third option, a flip mirror is used to divert the light into a CCD camera (Teledyne FLIR CM3-U3-50S5C-CS). This is used in conjuction with a white light source on the excitation arm, for bright-field imaging of the sample in order to find the regions of interest.

4.1.2 Setup 2 - 'Attodry'

As already mentioned, the Attodry setup is built on the same principle as the Bluefors one, however the setup itself is vertical and constructed in a cage system, whereas the Bluefors one is laid out on an optical table. The objective is the Mitutoyo M-Plan Apo 50X (NA = 0.42, f = 4 mm), and is outside of the cryostat. Also, a different spectrophotometer is used (Princeton Instruments HR-500) with a different CCD (Princeton Instruments PIXIS-400). This setup is also not equipped with the Wollaston prism, relying on the LCRs for polarization resolved measurements.

4.2 Measurement Techniques

4.2.1 Photoluminescence (PL) Spectroscopy

For PL measurements, a CW laser is used, typically the Ti:S laser or the 640 nm pulsed laser operated in CW mode. The light is routed through one of the two options into the spectrophotometer, with a 300 g/mm grating, blazed at 750 nm. PL measurements are a fundamental tool in our work, revealing the energy and intensity of the excitons in our devices. Our setup features independent settings of excitation and collection polarization, enabling us to also measure the degree of circular polarization (DCP) of our emission. In such experiments, the excitation is set to, for example, σ_1 polarization, and emission of both σ_1 and σ_2 is measured. The DCP is defined by the ratio of intensities:

$$DCP = \frac{I_{\sigma_1} - I_{\sigma_2}}{I_{\sigma_1} + I_{\sigma_2}}. \tag{4.1}$$

A DCP of 0 would indicate an equal amount of two emissions, while a DCP of 1 (-1) would indicate 100% σ_1 (σ_2) emission.

4.2.2 Photoluminescence Excitation (PLE) Spectroscopy

The PLE measurements are performed in the same way as the PL ones, but here the excitation wavelength is scanned, requiring the use of the Ti:S laser. Here, we measure the PL spectrum as a function of the excitation wavelength, revealing details about the absorption processes in addition to the exciton emission.

4.2.3 Reflectance Spectroscopy

Another method of measuring the absorption spectrum of the TMD monolayers is to shine white light in the range of the exciton resonance and observe the characteristic Fano shape at the exciton absorption. For this, we use the same experimental setup as in the PL and PLE cases, but without any filters, as the excitation and collection light are now of the same color. To deteremine the actual absorption spectrum of the material of interest, a reference spectrum is needed of the excitation light, ideally exactly as it would reflect off the substrate if the material was not there. The formation of trions/polarons and the shift in the exciton energy with doping discussed in Section 2.3.2 is of use here - by placing the TMDs in a high doping regime the oscillator strength at the original excitonic resonance vanishes, allowing us to use that spectrum as the reference when analyzing the undoped exciton (and vice versa), thereby eliminating the errors that would be introduced by taking a reference at a different position.

4.2.4 Differential Reflectance Spectroscopy

In order to increase the signal-to-noise ratio of the reflectance spectroscopy method when tracking the changes of reflectance contrast with, for example, sample doping, a CW laser at a wavelength close to the exciton resonance can be used. Then, an AC electric signal can be applied on the gates, varying the doping in the sample with time

at some frequency much smaller than the characteristic frequency of the device. If the reflected light is collected on a photodiode and coupled to a lock-in amplifier with the AC signal as a reference, very small changes to the reflectance contrast can be detected, but only for the particular wavelength chosen by the laser. This technique is useful in measuring the Wigner crystal states in TMD heterostructures, as shown in Figure 2.20.

4.2.5 Lifetime Measurements

In order to measure the lifetime of exciton emission, we use 640 nm laser in pulsed emission mode. The emission is filtered in a spectral range of interest matching the exciton and collected by an APD (PerkinElmer SPCM-AQR-16-FC) plugged into a photon counting module (Picoquant PicoHarp 300). The APD records counts with high sensitivity, while the photon counter records the delay of each photon with respect to the pulsed laser clock, which triggers the counter. The resulting data is a histogram of all recorded photon delays, which for a Poisson process traces out an exponential decay. In order to avoid dead-time effects, the total count rate is kept at less than 5% of all excitation intervals. This reduces the distortion of the histogram due to the dead time of the APD. Dead time is the time when the APD cannot record data after a photon count already occurred. At a total hit rate of 5%, the likelihood of photons striking the detector during the dead time can be neglected.

4.2.6 Time-Resolved PL Spectroscopy

For time-resolved photoluminescence spectra measurements (TRPLS), we used the same method as for PL, but strictly in the fiber-coupled mode. This enabled us to add a fiber-coupled acousto-optic modulator (AOM) (Aerodiode 850-AOM-2) in-line with the fiber collection, which modulated the collection time window. Figure 4.2 shows a truncated measurement setup diagram with the AOM fiber module. The AOM,

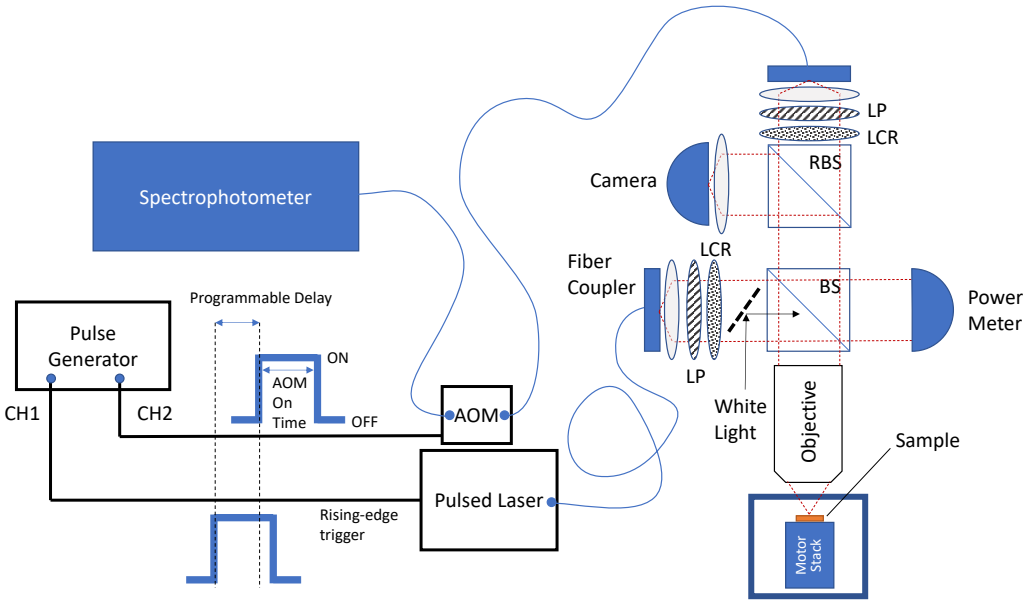

Figure 4.2: Time Dependent PL Measurement Setup. An external pulse generator synchronizes the pulsed laser and an AOM, while defining the AOM delay relative to the pulsed laser and the AOM ON-time, allowing for a defined time-window of PL collection.

when turned on, allows the light to pass, at 50% intensity, and the AOM controller can be externally controlled, turning on whenever an external input voltage is at a value of 3V, and off for 0V. The AOM ON-time was controlled by a tunable-width digital delay/pulse generator (SRS DG535), whose other channel also served as the trigger for the pulsed laser, ensuring synchronization across excitation and collection. The AOM ON-time was set to 10ns by sending 10ns-wide pulses from the SRS DG535 and operating the AOM controller in external trigger mode. The delay of the AOM ON-time pulse was then scanned, giving binned PL measurements over 10 ns intervals at arbitrary delays. In this way, we are able to continuously collect data with the spectrophotometer, while the AOM filters the emission in time.

Chapter 5

Excitonic Mott Insulator and Electron-Exciton Composite Crystals in TMD Bilayers

As we elaborated in Chapter 2, TMD heterostructures with strong moiré potentials are being vigorously investigated for strongly correlated electronic phases [13, 14, 15, 16, 17, 18]. Therefore, it is a natural question whether, in addition to the correlated electronic phases, TMD heterobilayers could host interesting excitonic phases as well. In this chapter, we present our measurements of two such phases - the excitonic Mott insulator and a mixed insulating phase comprised of excitons and electrons. A section of these results are, as of the time of writing, published as a pre-print [102], and the excitonic Mott insulator was also observed by several other groups concurrently with our measurements [103, 104, 105, 106, 107, 108].

5.1 Excitonic Mott Insulator

In a typical type-II semiconducting heterostructure, the electron and hole are localized in separate layers, leading to long-lived ($\sim$ 1-100 ns), spatially indirect interlayer

excitons (IXs). As discussed in Section 2.3.3, IXs feature an out-of-plane static dipole moment, making them good candidates for realizing phases arising from finite-range interactions. Moreover, as described in Section 2.2.3, moiré excitons can be trapped inside moiré potentials, in the same way as electrons. Therefore, an interesting question is what the energy of placing two IXs in one moiré site would be, illustrated by U_{XX} in Figure 2.11.

In order to measure U_{XX}, we study the PL of IXs in a WSe_2/WS_2 heterobilayer. This platform has shown robust correlated electronic phases, including a wealth of Wigner crystals, indicating that it has a robust moiré potential. The sample we fabricated is presented in Figure 5.1. It features two heterobilayer regions, with a middle WSe_2 layer flanked by two WS_2 layers. The WS_2 layers come from the same original flake and are mutually rotated by 60° using the tear-and-stack technique. Using this arrangement and staggering the outer flakes, we created an H- an R-stacked region in the same sample, enabling us to study the two in the same cool-down of the cryostat and in near-identical conditions.

In order to confirm the presence of the moiré superlattice in our sample, we first studied the PL as a function of carrier doping, shown in Figure 5.2. Figure 1b shows the photoluminescence (PL) emission from IX in the H-stacked region, as a function of electron doping in the sample. Our dual-gated sample geometry (Figure 5.1) permits independent control of the doping and the out-of-plane displacement field. Consistent with other observations [104, 105, 106, 107, 108], we measure a blueshifted peak in PL (IX_e) at unit electron filling, which arises from the onsite exciton-electron repulsion $U_{Xe} \simeq 42$ meV. In addition, we observe a characteristic modulation of IX PL at other fractional fillings from 1/3 to unit filling, consistent with the formation of generalized Wigner crystals of electrons at fractional fillings [15, 14, 109]. We also observe a strong ($\sim$ 15 meV) redshift near 1/7 doping to a peak that we label IX_{ICe}, an effect that we will address in Chapter 6.

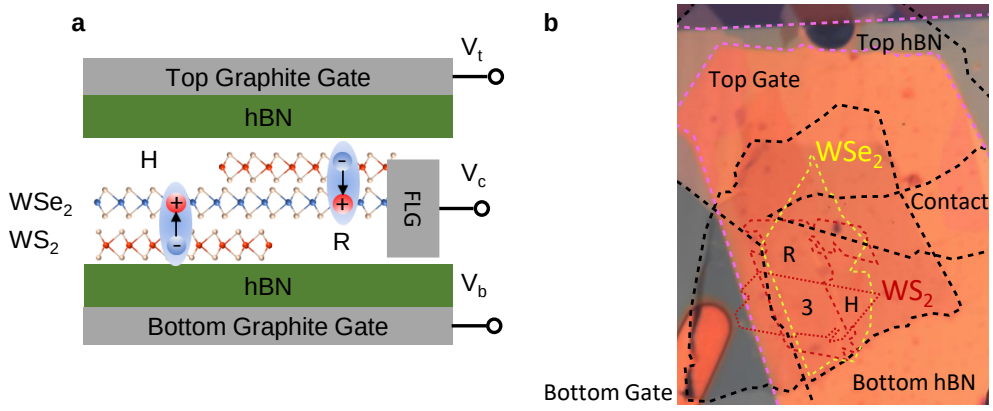

Figure 5.1: Sample Details. **a.** Schematic of the sample studied. The gating configuration allows for independent control of doping and electrical field in the sample. V_t denotes the top gate voltage, V_b the bottom gate voltage and V_c the direct contact voltage on the sample, which is in our case always kept grounded. The contact voltage is applied to the sample by a few-layer-graphene (FLG) flake. **b.** Optical microscope image of the sample, with regions of different heterobilayer stacking angle indicated as R for R-stacking, H for H-stacking and 3 for the trilayer region, in which the H- and R-stacked outer WS_2 layers overlap.

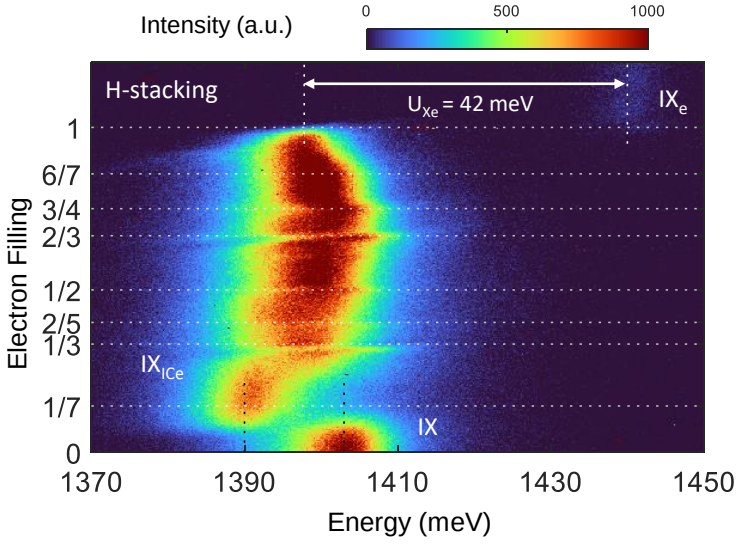

Figure 5.2: Doping PL Scan. Doping scan of the photoluminescence (PL) emission of an H-stacked region, using 10 nW of 1 MHz 640 nm pulsed laser excitation. Dashed lines indicate generalized Wigner crystals at fractional fillings.

Having established the presence of a moiré lattice in our sample, we study its photon emission properties. The PL signal as a function of excitation power of the H-stacked region of the sample is shown in Figure 5.3. As seen in Figure 5.3a, at a certain power threshold, another blue-shifted peak appears. The blue-shifted peak rapidly increases in intensity with increasing power, but does not appreciably shift past the initial blue-shift relative to IX. Figure 5.3b shows a comparison between a normalized low and high power spectrum, showing the emergence of the new peak at an energy 36 meV greater than the IX. We attribute this peak to a state of double occupancy (two excitons) of a single moiré site decaying to a singly occupied site, and therefore label the peak IXX. This state is analogous to the IX_e in that the comparable size blue-shift observed means that IXs are also capable of forming a Mott insulator, with the U_{XX} acting as the Mott gap.

To further analyze this state, we analyze the power dependence of the total integrated intensity of the IX and IXX peaks in Figure 5.3c. We see that, up to the power at which we begin to observe the IXX peak, the IX peak intensity increases linearly, indicated by the slope of 1.00 ± 0.01 in the log-log plot. However, at the power where IXX begins, the IX intensity begins to saturate. We label the excitonic filling at this power as $\nu_{max} = 1$. Concurrently, IXX intensity begins to increase, and as shown in the figure inset, the rate is also linear with excitation power once the offset of the power needed to reach $\nu_{max} = 1$ is accounted for. Figure 5.3d shows the interpretation of this result. The number of intralayer excitons produced by pulsed laser is linear with power, as the powers used are not sufficient to saturate the monolayer absorption resonance. Then, as explained in Section 2.2.2, the intralayer excitons rapidly tunnel into the interlayer IX configuration. While there are free moiré sites, the repulsion between the IXs distributes them across nearby sites, ensuring a correspondent linear increase in the observed IX intensity. However, when all nearby sites are filled, the excitons have no option but to share a site, suffering the U_{XX} penalty,

and the population of this species then begins to increase linearly. This is in contrast to an isolated quantum emitter, where IX intensity tends to increase linearly and IXX quadratically with power, and IXX is observed even at low excitation powers, as shown in our previous work [110].

We further analyze our results by considering the emission helicity of IXX. Figure 5.4 shows the time-dependent PL of IX and IXX, as well as their degree of circular polarization (DCP, see Section 4.2.1). We notice that the IXX lifetime is significantly shorter than that of IX, which is likely due to rapid non-radiative recombination channels opening due to on-site exciton-exciton annihilation. In addition, the IX features a significant degree of cross-polarized (negative) DCP, meaning that its emission is opposite that of the excitation beam, accounting for a reflection off the substrate. This cross-polarization has been widely observed in WSe_2/WS_2 H-stacked samples, and is understood as a consequence of registry-specific selection rules (see Section 2.2.3) and the predominant mechanisms of intralayer exciton to interlayer exciton relaxation [106, 108]. However, the IXX peak shows no such DCP, even though the duration of its brief lifetime corresponds to the strongest DCP of the IX. This can be understood by considering the exchange interaction between two excitons in the same site. Excitons in different valleys consist of electron-hole pairs of opposite spins, and excitons in the same valley can have considerable exchange repulsion at high densities, even when not confined to the same site [20]. Therefore, in close proximity this repulsion forces the excitons on the same site to reside in opposite valleys. Due to the strong valley coupling to emission helicity, and due to the fact that the lifetime of the two valley excitons is the same in absence of any breaking of their symmetry (with magnetic field, for example), the IXX is indeed expected to have no DCP, as the helicity of the first emitted photon from this singlet exciton pair is completely randomized. This further confirms our assignment of IXX as a double exciton occupancy of a single site and the ensuing phase as an excitonic Mott insulator.

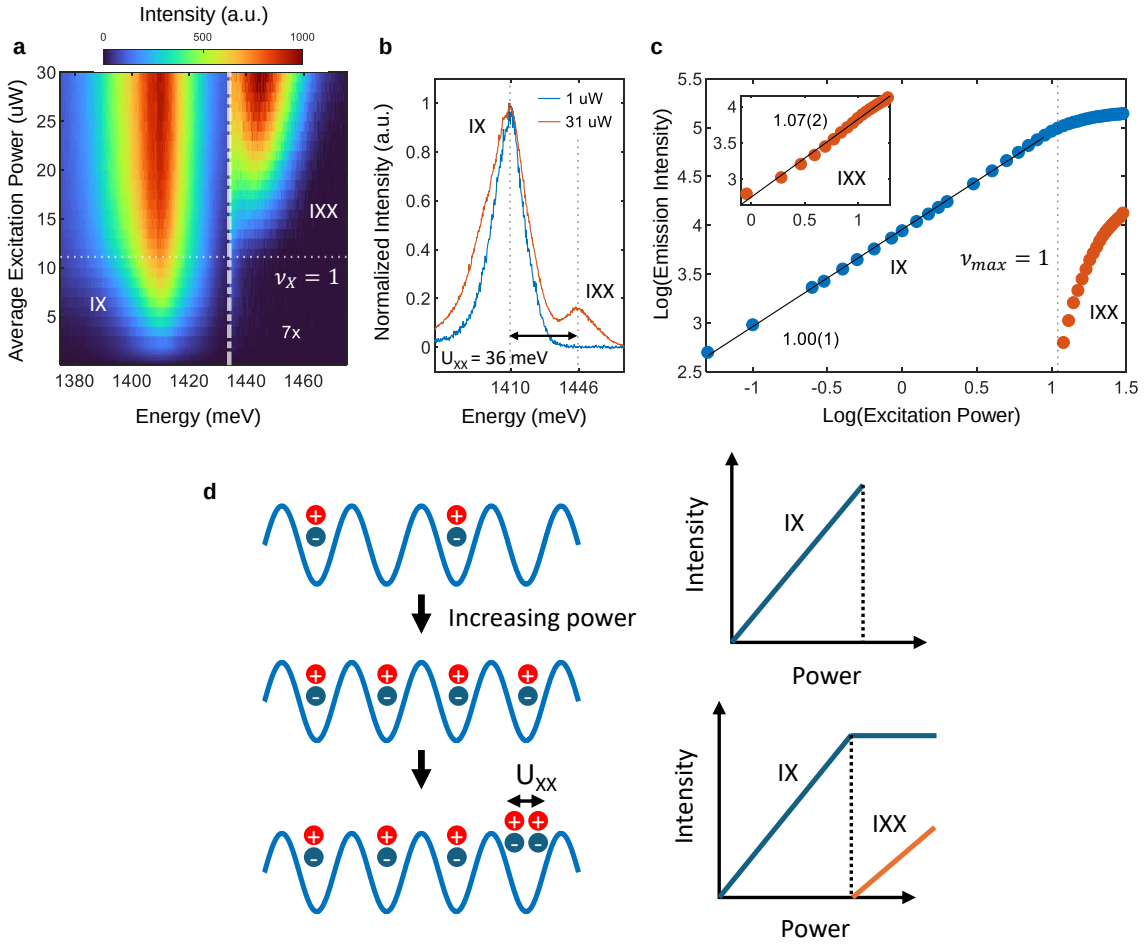

Figure 5.3: Detection of the Excitonic Mott Insulator by Photoluminescence. **a.** PL emission of an H-stacked region as a function of the average excitation power, using a 1 MHz 640nm pulsed laser. Data right of the vertical dashed line is scaled by 7x for visibility. Horizontal dashed line at 11.1 uW indicates when the IX begins to saturate and IXX emission becomes measurable. **b.** PL emission of an H-stacked region at a high and low excitation power, using a 1 MHz 640nm pulsed laser. The difference in IXX to IX energy shows $U_{IXX} = 36$ meV. At higher power, a red shoulder at 1395 meV becomes prominent. **c.** Log-log plot of total intensity of the IX and IXX peaks as a function of excitation power. The intensity of IX increases linearly (slope 1.00 ± 0.01) until the power at which IXX becomes measurable, when IX starts to saturate. The inset shows the IXX intensity against power, with an offset to the IX saturation power, which shows IXX intensity also increases linearly (slope 1.07 ± 0.02)) when the power is above the saturation value. **d.** (left) Schematic of sequential filling of excitons in a moiré lattice. The on-site repulsion U_{XX} leads to the excitonic Mott insulator at unit IX filling. (right) Idealized sketches of an expected intensity profile at different excitation powers before and after saturation.

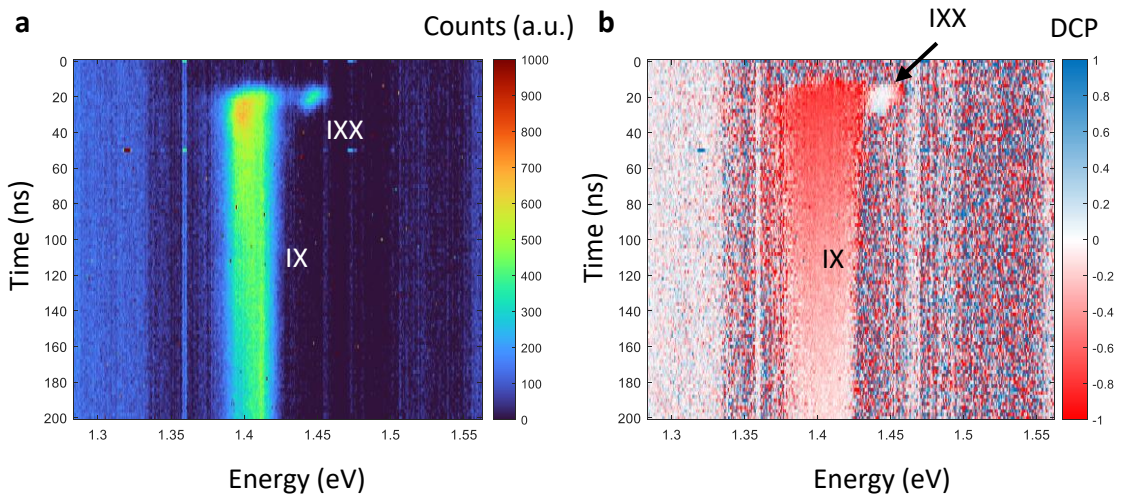

Figure 5.4: Emission Helicity of IX and IXX. **a.** Time-resolved photoluminescence spectra (TRPLS) of the H-position with no doping, with 16 uW of σ_1 polarized excitation power. **b.** Degree of circular polarization of the emission in panel a. IXX shows a characteristic absence of DCP as expected from the low-energy singlet configuration of the two excitons occupying the moiré site.

The clear presence of the excitonic Mott insulator also allows us to determine the excitonic filling below $\nu_{max} = 1$ with considerable precision. Since we have access to the TRPLS technique, we can measure the signal of from the first ~ 20 of emission, as in Figure 5.4. As the lifetime of IXX is much smaller than that of IX, the early collection effectively filters the weak IXX signal through while suppressing the IX signal whose blue tail can otherwise obscure the IXX peak when the spectrum is integrated across time. This allows us to detect IXX even when it is ~ 2 orders of magnitude weaker than IX, as seen in Figure 5.1c. Since the intensity below $\nu_{max} = 1$ depends linearly to high precision on the excitation power, we can conclude that no significant non-radiative emission channels are opened or closed with the increasing IX density, up to the Mott insulator state.

Due the fact that our excitation beam is Gaussian, at $\nu_{\max} = 1$, the sample region in the center of the beam achieves unit excitonic filling such that IXX forms. However, this may not be case for the regions further away from the beam center. Therefore,

$\nu_{\max}$ is a measure of maximal local excitonic filling at the center of the excitation beam. In the linear regime below $\nu_{\max} = 1$, we can still safely consider the IX density as depending linearly on the excitation power. This means that the determination of $\mathrm{P_{exc}}(\nu_{\max} = 1) = 11.1(1)$ uW provides a calibration to assign excitonic filling fractions, which becomes proportional to the excitation powers. In other words,

$$\nu_{\max} = \frac{P_{\mathrm{exc}}}{P_{\mathrm{exc}}(\nu_{\max} = 1)}. \tag{5.1}$$

We will make extensive use of this calibration in the subseqent sections and Chapter 6.

5.2 Mixed Exciton-Electron Mott Insulator

Having established the presence of an excitonic Mott insulator at full filling of the moiré lattice, we turn to the question of whether a mixed phase of electrons and excitons can form an insulating phase as well. We measured in the preceding section an on-site exciton-electron energy $\mathrm{U_{Xe}}$ at 42 meV, somewhat greater than the exciton-exciton on-site repulsion $\mathrm{U_{XX}}$ of 36 meV. Because of this comparable on-site energy, we expect that a Mott phase would occur also when each site is occupied either by an exciton or electron.

Figure 5.5a shows a doping scan at an excitation power corresponding to $\nu_{\max} = 1/3$, as determined by the method explained above. As before, at a certain filling, we see a blue peak, which may be from either IXX or IX_e, and so we label it IXX_e. The data is taken during the first 20 ns of emission to emphasize the IXX/IX_e peak. Unlike in the low excitation power case shown in Figure 5.2, the IXX_e peak appears exactly at 2/3 electronic filling, making the total filling ν_{tot} equal to 1. Increasing the excitonic filling to 2/3, as shown in Figure 5.5b, decreases the necessary doping needed to observe the IXX_e peak. Now, the IXX_e peak is observed at an electronic

filling of 1/3, maintaining the condition $\nu_{\mathrm{tot}} = 1$.

We further analyze the power dependence of excitonic emission at a fixed doping of $\nu_{\mathrm{e}} = 1/2$. Figure 5.6a shows that, up to the power where we observe the $\mathrm{IXX_e}$ peak, the IX peak increases linearly, as the slope of the log-log plot is precisely 1. Since this measurement is done in an H-stacked sample at an electronic filling above 1/7, the excitons form an intercell electronic complex, which is described in more detail in Chapter 6, and we therefore label the IX as $\mathrm{IX_{ICe}}$. Just like IX, the $\mathrm{IX_{ICe}}$ is restricted to one moiré site, and this difference has no effect on the full filling condition of the lattice. The emergence of the $\mathrm{IXX_e}$ peak marks the end of the $\mathrm{IX_{ICe}}$ linear regime and the peak begins to saturate. Simultaneously, the $\mathrm{IXX/IX_e}$ peak emerges and begins to increase. This transition occurs at $\nu_{\mathrm{max}} = 1/2$, which is 1/2 the power needed to reach the same transition in the undoped case of Figure 5.3c and fulfills the condition $\nu_{\mathrm{tot}} = 1$. As in Figure 5.3c, Figure 5.6b shows that, when offseting for the $\nu_{\mathrm{tot}} = 1$ power, the slope of the log-log plot of the $\mathrm{IXX_e}$ peak is also 1, and the peak increases linearly. By the same reasoning as in the preceding section, this sequential filling of the excitons from lower to higher energy states is a clear signature of a Mott insulating state (Figure 5.6c).

In order to characterize the $\mathrm{IXX/IX_e}$ peak, we also observe its emission helicity. Figure 5.7a shows the time-resolved measurement of the spectrum at 2/3 electronic filling. The measurement conditions were identical to those in Figure 5.4, apart from the presence of the electronic 2/3 GWC. We see a substantially brighter $\mathrm{IXX/IX}_e$ peak compared to Figure 5.4a, which is expected since fewer sites are available to the excitons, and the same excitation power produces proportionally more $\mathrm{IXX/IX}_e$.

Looking at the emission DCP in Figure 5.7b, we find that, unlike in 5.4b, the blue-shifted peak has a high degree of DCP. Closer inspection reveals that the peak does feature some structure, with the bluer portion exhibiting a higher DCP than the red side. This would indeed be expected if the emission came both from IXX and IX_e

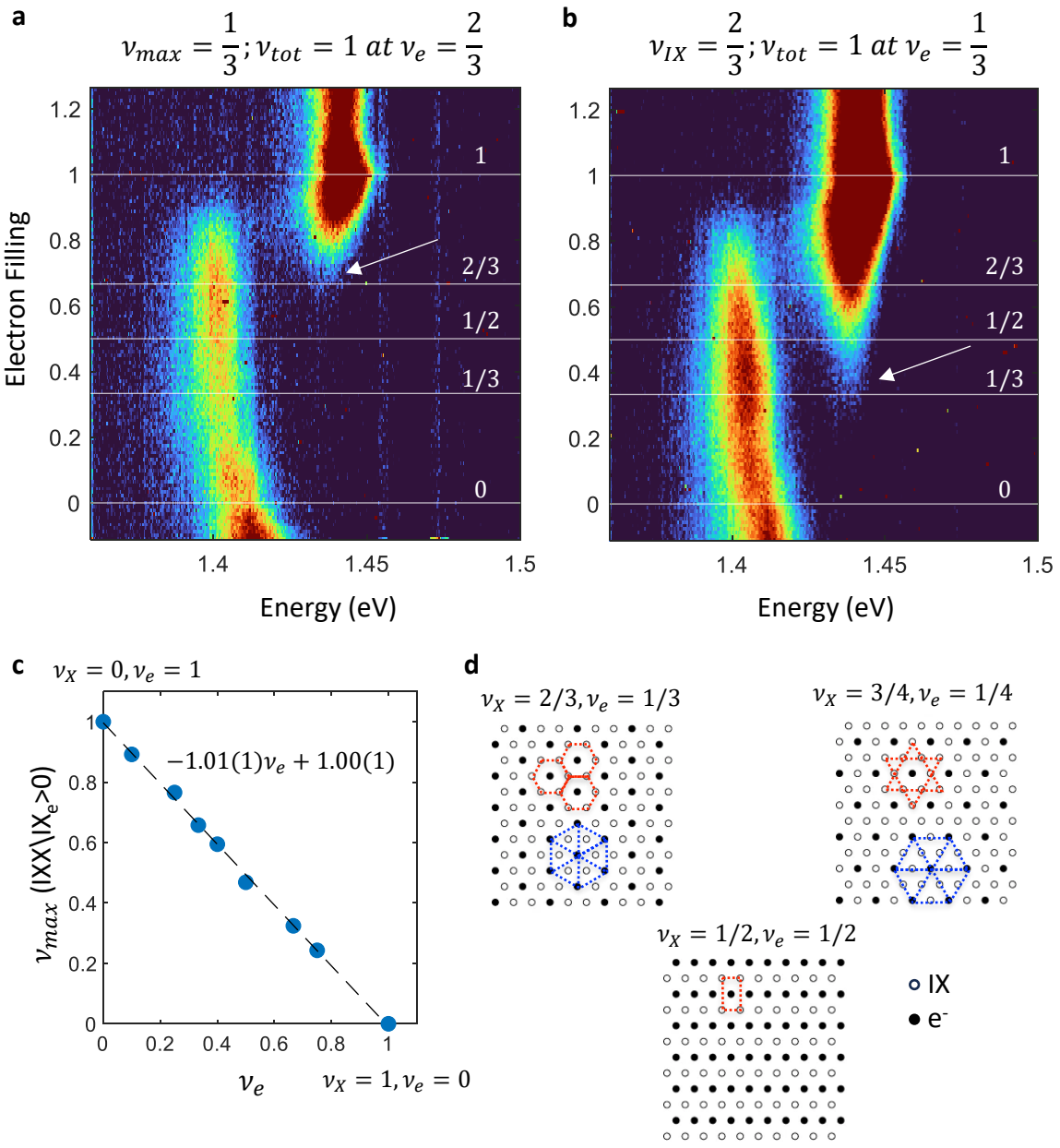

Figure 5.5: Doping and Power Induced Electron-Exciton Mott State. **a.** Doping scan of the photoluminescence spectra of the H-position with doping, using 3.7 uW of 640 nm pulsed excitation, corresponding to $\nu_{\max} = 1/3$. **b.** Doping scan of the photoluminescence spectra of the H-position with doping, using 7.4 uW of 640 nm pulsed excitation, corresponding to $\nu_{\max} = 2/3$. **c.** Plot of $\nu_{\max}$ needed to observe IXX/IX$_e$ peak as a function of electron filling ν_e. The fitted line with a slope of -1 and intercept 1 indicate that electrons and excitons are competing for the same moiré sites. **d.** Illustration of the composite electron-exciton crystals at select electron generalized Wigner crystals.

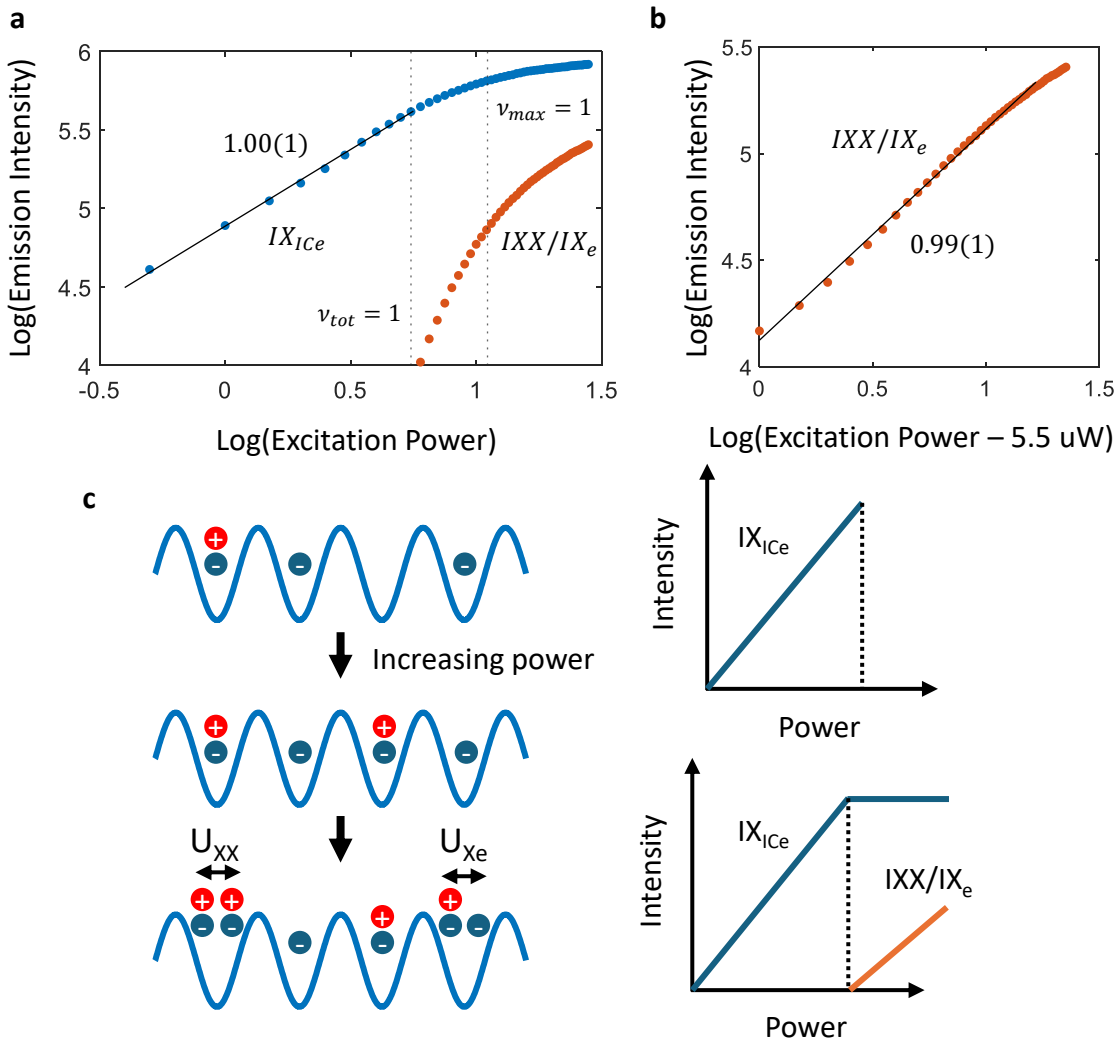

Figure 5.6: PL Intensity Scaling at Electronic Half-filling. **a.** Log-log plot of total intensity of the IX_{ICe} and IXX/IX_e peaks as a function of excitation power. The intensity of IX increases linearly (slope 1.00 ± 0.01) until the power at which IXX/IX_e becomes measurable, when IX_{ICe} starts to saturate. **b.** Log-log plot of IXX intensity against power, with an offset to the IX saturation power, which shows IXX intensity also increases linearly (slope 0.99 ± 0.01)) when the power is above the saturation value.

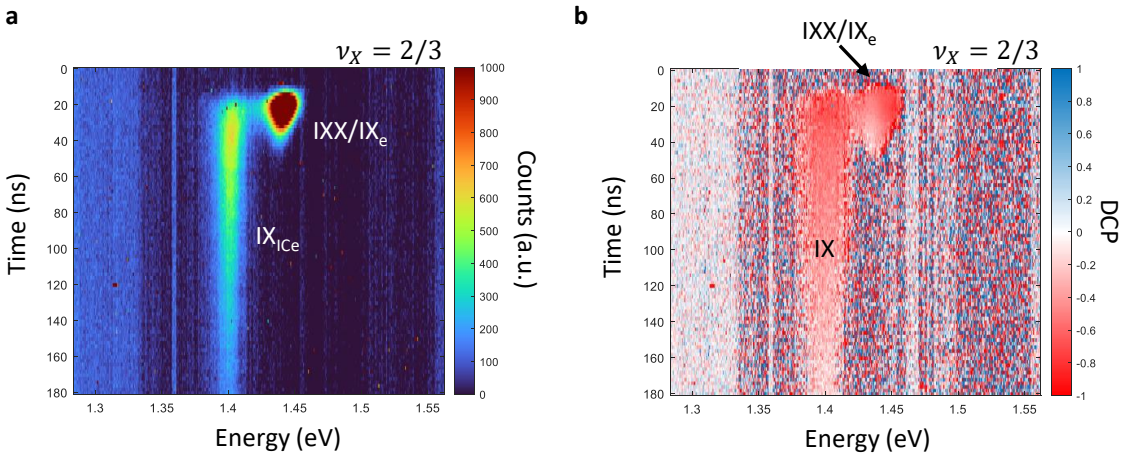

Figure 5.7: DCP of the IXX/IX$_e$ peak. **a.** TRPLS of the WSe_2/WS_2 bilayer with 2/3 electron filling, with 16 uW of σ^+ polarized excitation power. **b.** Degree of circular polarization (DCP) of the emission in panel a. The high-energy emission consists primarily of IX$_e$ and shows a high degree of DCP, with a detectable red-tail IXX contribution with no DCP.

species, as the IXX is slightly lower in energy and has strictly no DCP, as explained in Section 5.1, whereas IX$_e$ is in fact expected to have stronger DCP than the IX peak, as the presence of the electron in the same site inhibits valley-flip relaxation, as it would require the simultaneous exchange of three particles [111]. Therefore, the observed peak is indeed a mix of IXX and IX$_e$, which are too close to be spectrally resolved.

5.2.1 Excitonic Lifetime in Mixed Exciton-Electron Moiré Systems

One of the primary motivations for our study of excitonic phases is the potential of modulating the light-matter coupling properties of the excitons, depending on which phase they are in. In this section, we focus primarily on the effects of the exciton-electron interactions in mixed systems on exciton emission lifetime – for an analysis of the effects of exciton-exciton interactions on exciton emission lifetime refer to Chapter 6. In order to address this question, we measure the excitonic lifetime as a function

of electron doping in system, using the method outlined in Section 4.2.5.

Figure 5.8a shows a plot of exciton decay curves at a fixed excitation power corresponding to $\sim 5\%$ total excitonic filling. The emission time is markedly higher near insulating states (0, 1/3, 1/2, 2/3) than away from them, with a particularly long lifetime at 2/3. These measurements are suggestive of the possibility that incompressible mixed crystals feature different excitonic radiative lifetimes than when mobile electrons are present. In order to quantify the lifetime, we extract the mean emission time (MET) of the exciton as the expectation value of the time after the laser pulse a count is detected at the APD. The MET as a function of doping is shown in Figure 5.8b. We observe a clear 2/3 peak, as well as a smaller peak at 1/2 within a decreasing trend. The 1/3 state is interestingly a local minimum within a broad peak. However, the interpretation of these lifetimes requires consideration of the total emitted exciton intensity. Since the power used generates a total exciton density of only 5% of the moiré sites for each pulse, the mixed crystal picture alone would predict a constant emission intensity until the electronic filling of 95%. However, this is only true if itinerant doped electrons do not affect the non-radiative rate of the created excitons. The observed variation in exciton intensity shown in Figure 5.8b indicates that the electrons indeed affect the non-radiative rate, with exciton intensity peaks at the incompressible states. This suggests that the dominant non-radiative mechanism is electron-exciton scattering, which is enhanced by the presence of mobile electrons and suppressed near the incompressible states.

In order to extract the effect of the electrons on the radiative rate of the excitons, we must account for the variable non-radiative rate. The total intensity I we observe is a function of the branching ratio of the radiative and non-radiative rates [47]:

$$I = I_{\max} \frac{\gamma_{\text{rad}}}{\gamma_{\text{rad}} + \gamma_{\text{nr}}} \tag{5.2}$$

where γ_{rad} is the radiative emission rate, γ_{nr} is the non-radiative recombination

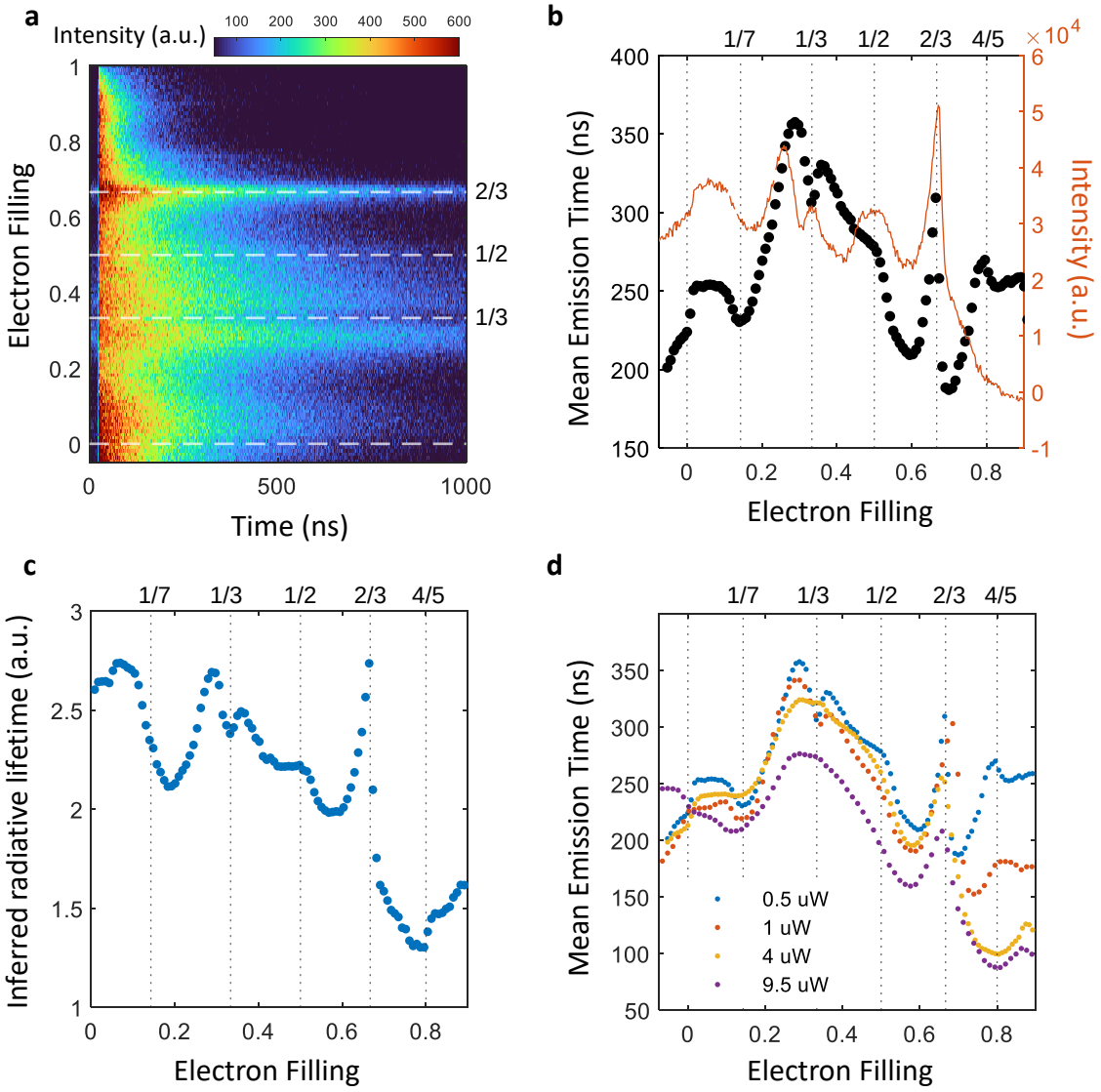

Figure 5.8: Moiré Exciton Lifetime with Itinerant Moiré Electrons. **a.** Colormap of lifetime traces as function of doping in an H-stacked position of the WSe_2/WS_2 sample. Excitation power used was 0.5 uW, corresponding to $\sim 5\%$ total filling. **b.** (*left, black*) Mean emission time (MET) as a function of electron doping, extracted from panel a. (*right, orange*) Total emission intensity of the excitons from panel a. **c.** Inferred relative radiative rate as a function of electron doping. Rate obtained using the MET and intensity information, per equation 5.3. The rate is in arbitrary units since lack of information about the non-radiative rate preludes an absolute measurement. **d.** Mean emission time as a function of excitation power. All observed powers demonstrate a qualitatively similar trend.

rate and $I_{\max}$ is the intensity we would observe if all excitons emitted radiatively ($\gamma_{\mathrm{nr}} = 0$). The MET is the inverse of the average total emission rate $\langle \gamma_{\mathrm{tot}} \rangle = \langle \gamma_{\mathrm{rad}} + \gamma_{\mathrm{nr}} \rangle = \frac{1}{MET}$. If we assume the itinerant electrons do not affect $I_{\max}$ significantly at such a low excitation power away from saturation, we can treat $I_{\max}$ as a constant, allowing us to solve for γ_{rad}:

$$\gamma_{\mathrm{rad}} = \frac{I}{I_{\max}} \gamma_{\mathrm{tot}} \tag{5.3}$$

Figure 5.8c shows the relative radiative rate γ_{rad} calculated using Equation 5.3, as a function of doping. As we have no information on $I_{\max}$, we can only evaluate γ_{rad} in arbitrary units. The radiative rate itself therefore seems to vary considerably with doping, with the rate near the incompressible states increasing close to the value of the intrinsic lifetime. This indicates that the presence of incompressible states affects the radiative lifetime directly, in addition to the non-radiative lifetime. Again, note that for this analysis $I_{\max}$ is assumed to be a constant with electron doping, which means the analysis can be only performed for low-power cases, as increasing power would lead to saturation of the moiré sites.

Next, we examine the effect of increasing the excitation power on the doping dependence of the lifetime. In the undoped regime, increasing the power leads to an increase of emission lifetime, an effect examined in-depth in Chapter 6. However, this trend is inverted as soon as doped electrons are introduced, as shown in Figure 5.8d. Along with an overall decrease in MET with increased power, some of the finer features of the graph are smoothened out at higher powers. However, the main qualitative features of the low-power case are still present, with marked increases at 1/3 and 2/3 observable at high powers as well.

In addition to the radiative lifetime, we also characterize the exciton valley dynamics as a function of electron doping. Figure 5.9b shows the DCP in direct comparison to the full emission profiles in Figure 5.9a. Clearly, the DCP lifetime increases greatly

near full electronic filling, with a rise starting near 2/3 filling. We see that the features we observe in total lifetime at 1/3 and 1/2 are not clearly reflected in the DCP data, with the exception of the 2/3 state, where excitons have a clearly longer valley lifetime. The DCP is of negative sign, since the dominant mechanism of emission is cross-polarized, as explained in the previous section. We extract a DCP decay lifetime via exponential fitting, shown in Figure 5.9c, which shows that the DCP lifetime increases by almost a factor of 2 near full filling. Figure 5.9c also shows that the initial DCP of emission, while varying with a similar trend to the lifetime, remains relatively high, ruling out the possibility that the lifetime we observe is simply due to the instrumental limitations of DCP detection. Higher excitation powers follow the same trend, with only 2/3 as a prominent peak in DCP lifetime, and significant lifetime enhancement as the filling approaches unity. This effect is similar to the significant enhancement in exciton diffusion lengths at doping near unity moiré filling recently observed in the same system [112, 113]. Large excitation powers also seem to increase the DCP lifetime at lower fillings, an effect of unclear origin.

5.3 Conclusion

Our results show that excitons in WSe_2/WS_2 moiré superlattices feature large on-site repulsion, which enables the realization of the Bose-Hubbard model [114]. Other systems that realize this model, such as ultracold atoms and GaAs-based platforms, cannot reach the < 10 nm site separation of the moiré system. Furthermore, this system is easily integrated into nanocavities and features a tunable emission energy, making it a promising candidate for an effective integrated entangled photon source, with entangled chiralities of the two photons emitted from the same site via the biexciton cascade that we observe through the absence of DCP in the IXX peak. Beyond this, we show that the Mott state extends to the mixed electron-exciton

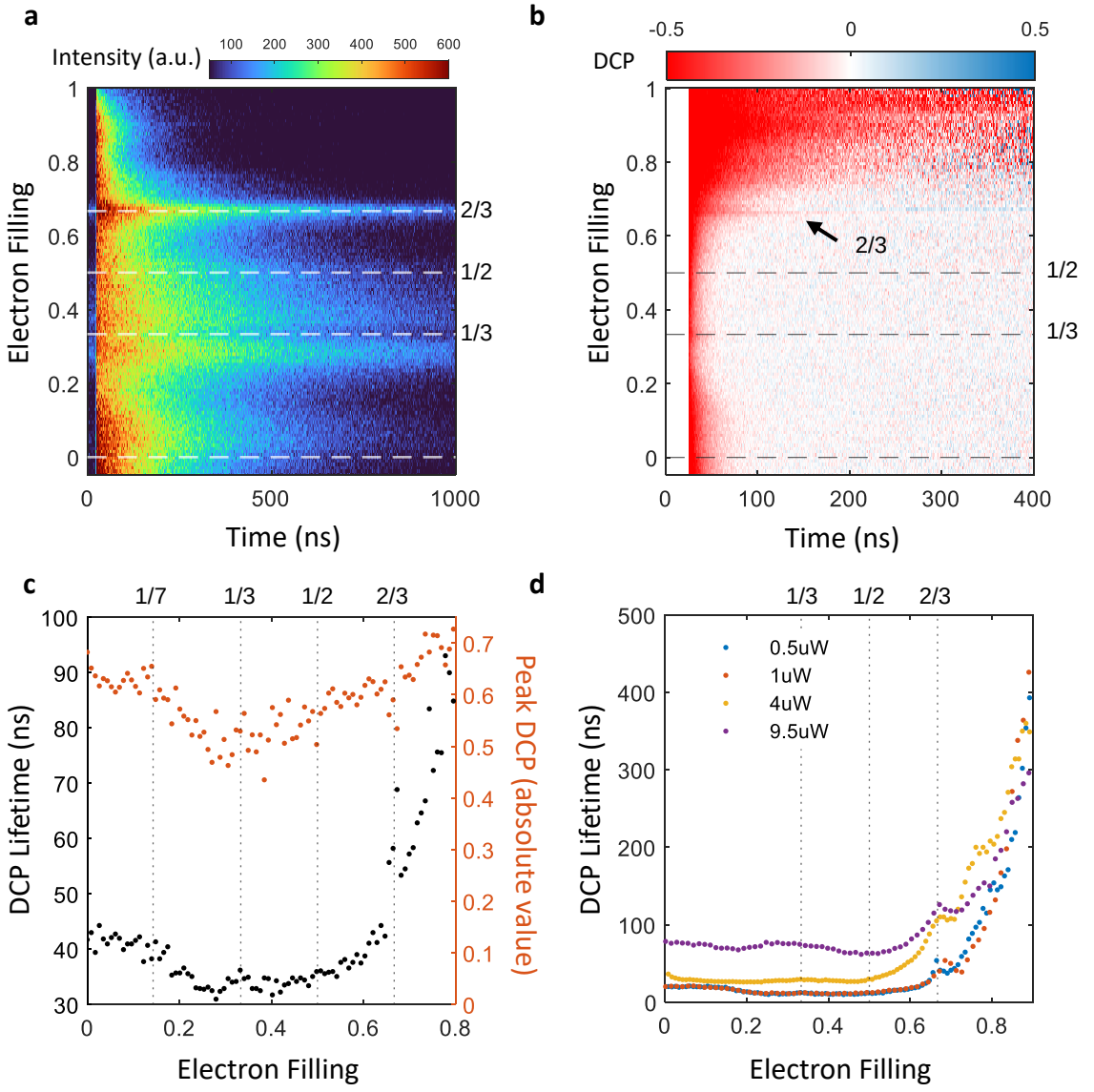

Figure 5.9: Moiré Exciton Valley Lifetime with Itinerant Moiré Electrons. **a.** Colormap of lifetime traces as function of doping in an H-stacked position of the WSe_2/WS_2 sample. Excitation power used was 0.5 uW, corresponding to $\sim$ 5% total filling. **b.** Colormap of degree of circular polarization (DCP) of data shown in panel a. **c.** (*left, black*) Extracted DCP lifetime (exponential fit) as a function of electron doping. (*right, orange*) Peak DCP at the start of emission as a function of doping. **d.** DCP lifetime as a function of excitation power. All observed powers demonstrate a qualitatively similar trend.

regime, and realize dynamic mixed electronic and excitonic crystals. Such states may have more exciting physics in store, as they allow for programmable tuning of distances between the free moiré sites, which could enable tunable collective light emission in a regime where the sites are strongly coupled by the electromagnetic vacuum [115]. We indeed observe some promising signatures of such effects in the excitonic lifetimes, but a model that can explain these observation is left as an open question. Furthermore, we observe an enhancement of exciton valley lifetime at the 2/3 filling and near-unity electronic filling states, effects whose cause is also unknown.

Chapter 6

Excitonic Ferroelectric Phase

In WSe_2/WS_2 heterobilayers, we observed significant differences in the PL spectra of R- and H-stacked species. While both exhibit the excitonic Mott insulator discussed earlier, these differences prompted us for a closer investigation, which revealed signatures of spontaneous ferroelectric ordering of excitons at sufficient densities in the H-stacked region. These results are, as of the time of writing, published as a pre-print (the same as Chapter 5) [102]. The sample under study is the same one as studied in Chapter 5 and shown in Figure 5.1 The Monte-Carlo simulations of excitonic dynamics featured in this chapter were developed by our collaborators Dr. Jan Kumlin and Professor Thomas Pohl of TU Wien.

6.1 The In-plane Quadrupolar Exciton

In addition to confining the excitons, the moiré potential can give rise to a richer internal structure of moiré excitons that results in qualitatively different excitonic properties and interactions. The moiré unit cells, which may be thought of as 'moiré atoms', can contain multiple minima for electrons and holes, allowing for different 'moiré orbitals'. For example, electrons and holes in different moiré orbitals can have an in-plane separation that greatly exceeds the out-of-plane displacement set

by the layer separation, resulting in a large static dipole moment, and consequently strong exciton-exciton interactions. Figure 6.1 shows DFT calculations from Wang et al. of ground-state electron and hole wavefunction densities in a R- and H- stacked WSe_2/WS_2 heterobilayer [106]. The figure predicts that in R-stacked samples, the in-plane position of electron and hole inside a moiré cell would be the same R_h^X position, while in H-stacked samples, the electron and hole would occupy laterally displaced positions, with the hole in the H_h^X site and electron in the H_h^h site. While these calculations are for single particle wavefunctions of electrons and holes, they are suggestive of the possibility of rather distinct excitonic species in these two scenarios. In fact, if an exciton was formed in the H-stacked sample such that the hole and electron reside in different lattice sites, its ground state would be expected to be a quadrupolar exciton. For a given position of the hole (electron) of the exciton, the electron (hole) is free to delocalize over the three equivalent neighboring sites, shown in Figure 6.1, resulting in an in-plane quadrupolar moment.

In order to investigate the quadrupolar exciton, following Wang et al., we examine more closely the doping dependence of exciton PL in the H-stacked region of the WSe_2/WS_2 sample shown in Figure 5.2. A more detailed view of the red-shift at 1/7 state is shown in Figure 6.2a. We observe the formation of a red-shifted peak with doping, labeled IX_{ICe}, with the initial IX peak disappearing completely when an electron filling of 1/7 is reached, as seen in Figure 6.2b. This feature is unique to the H-stacked case and is not seen in R-stacked samples both in our own measurements and in the literature [106, 108].

Such a state is evidence for the quadrupolar exciton in the H-stacked heterobilayer. As shown in Figure 6.2c, the 1/7 electronic filling corresponds to a Wigner crystal where the electrons are each surrounded by 6 empty sites, minimizing the electron-electron repulsion by leaving a two-site gap between neighboring electrons. This means that all empty moiré sites have exactly one neighboring site occupied by an

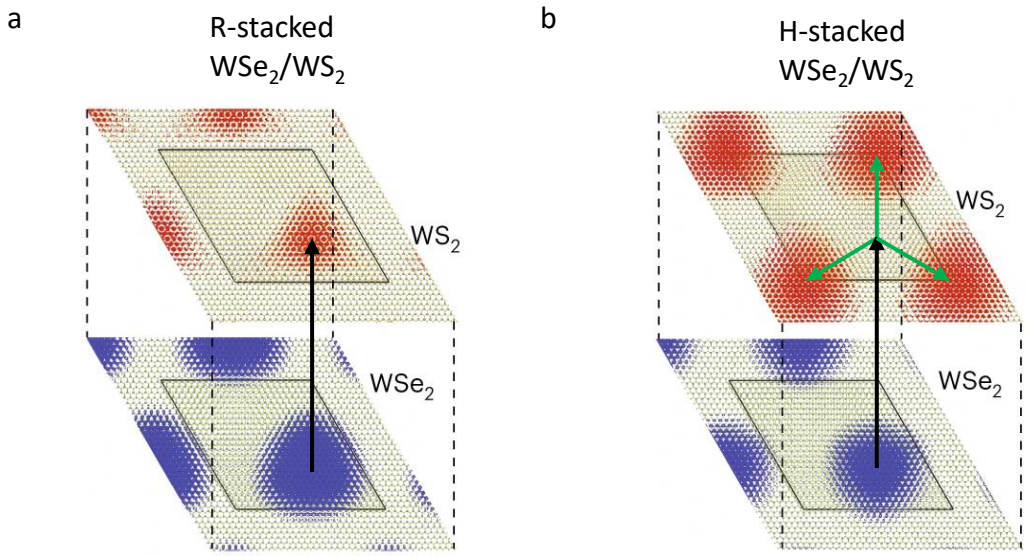

Figure 6.1: WSe_2/WS_2 Moiré Exciton DFT Calculation. Panels adapted from [106]. Calculated spatial Kohn–Sham wavefunction of the valley-moiré conduction band (bottom) and valence band (top) in **a.** R-stacked and **b.** H-stacked WSe_2/WS_2 heterobilayer, illustrating the expected spatial distributions of band-edge electrons (red) and holes (blue). Isosurface of squared wavefunction is taken at 2% of its maximum value. Black arrows indicate the out-of-plane component of the dipole moment, while the green arrows indicate the in-plane dipole components forming the quadrupolar exciton.

electron. Therefore, whenever an additional exciton is added to the system, it has a guaranteed electron neighbor. Figure 6.2d illustrates how a quadrupolar exciton neighboring an electron can change configurations, polarizing into a dipolar state, as the symmetry between the three equivalent hole sites is broken and the hole is attracted to the neighboring itinerant electron. The exciton and electron form a bound state termed the exciton-electron complex or IX_{ICe} [106]. In this way, even though the on-site interaction of an exciton electron complex is repulsive, as evidenced by the positive U_{Xe}, the cross-site interaction V_{Xe} can be attractive.

6.1.1 Density-dependent Redshift of IX

Having established the presence of quadrupolar excitons and a strong moiré potential in our sample, we studied the density dependence of IX emission in absence of electrons, with the goal of exploring potential effects of cross-site exciton-exciton interactions V_{XX}. Figure 6.3 shows the power dependence of PL spectrum under continuous-wave (CW) driving, which establishes a steady-state exciton density for a given power. As shown in Figure 6.3a, we observe a red-shifted peak to emerge at an excitation power below the critical power for creating IXX. With increasing pump power, this red-shifted exciton signal, which we denote as IX_d, rapidly exceeds the low-density IX-peak and eventually dominates the entire exciton emission at high densities. Figure 6.3b shows select line spectra from Figure 6.3a, from which we can measure the IX to IX_d redshift to be $\sim$ 15 meV, comparable to the redshift seen for V_{Xe} in Figure 6.2. Importantly, we do not observe the red-shifted IX_d peak in R-stacked regions of the sample under identical CW excitation, as seen by comparing Figures 6.3c and 6.3d, though IXX is present in both regions. This indicates that the emerging red-shifted IX_d peak originates from the excitonic in-plane dipole, which is only present in the H-stacked case. In fact, the coexistence of IX and IX_d, together with the absence of a gradual energy shift with increasing powers, rules out

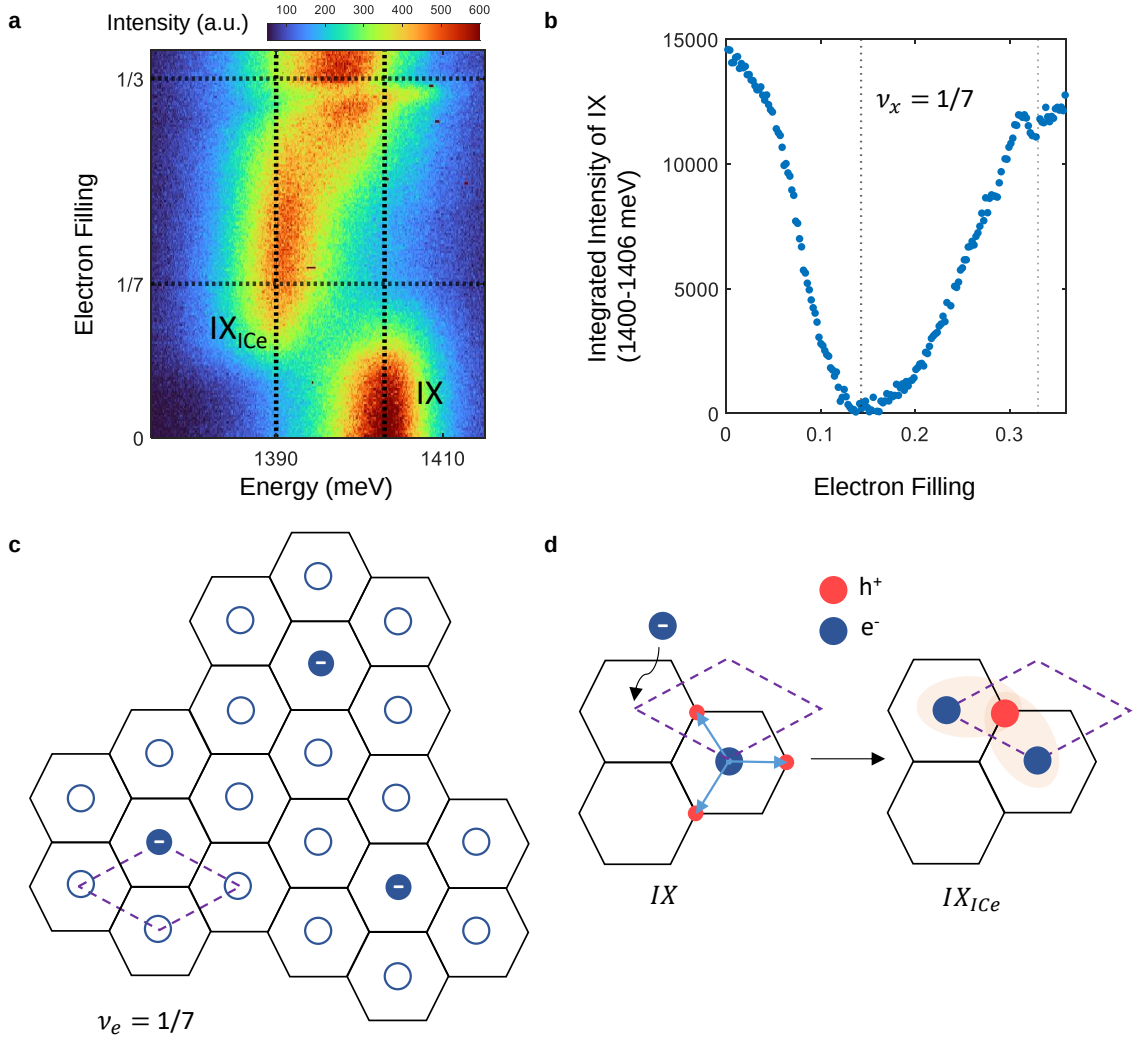

Figure 6.2: The $\nu_e = 1/7$ filling state and IX_{ICe}. **a.** Detail of doping-dependent photoluminescence from Figure 5.2, emphasizing the transition at $\nu_e = 1/7$ doping to the 13 meV red-shifted IX_{ICe}. **b.** Integrated intensity of the IX (non-redshifted) intensity. At 1/7 filling, all IX emission has been red-shifted. **c.** Schematic of 1/7 filling generalized Wigner crystal. A moiré unit cell is indicated in purple dashed lines, and the hexagonal full lines indicate the effective electronic lattice, with each electron site at the center of a hexagon. At 1/7 filling, each unfilled electron site is adjacent to one doped electron such that an IX optically generated in any unoccupied moiré cell will have a nearest-neighbor doped electron.**d.** Schematic of the formation of the IX_{ICe}, described in the main text. The addition of an IX next to a doped electron leads to the formation of an intercell electron-exciton complex.

power-dependent sample heating as a cause for the emergence of the IX_d peak.

Because of the importance of the R- and H- stacked comparison, let us clarify our assignment of H- and R-stacked regions. Because of our sample geometry (Figure 5.1), the R- and H-stacked regions have opposite slopes of the Stark shift with the out-of-plane electric field. Figure 6.4 confirms that excitons in the measured positions of the H- and R- stacking indeed have opposite dipoles. Apart from the IX_{ICe}, which is only observed in the H-stacked region, we can also confirm the stacking by considering the g-factor of the IX. Furthermore, the measurement of the IX g-factor of 10.5 ± 0.5 shown in Figure 6.5 in the H-stacked region are consistent with previous measurements of WSe_2/WS_2 R- and H- heterostructures [15, 116]. The two regions have different g-factors for reasons described in Section 2.3.4.

In order to further investigate the surprising red-shifting density-dependent behavior of the IX, we turn to the IX decay dynamics. Figures 6.6a and 6.6b show the time evolution of the total PL signal from the combined IX and IX_d peaks for different initial lattice filling fractions ν_{max}, controlled by the power P_{exc} of the excitation pulse. Up to an initial excitonic filling of $\nu_{max} \approx 0.36$, we observe a simple exponential decay with a lifetime of 160 ± 10 ns. As the filling increases beyond this value, the initial decay dynamics slows down steadily (Figure 6.6b), and the initial decay time saturates to a three times larger value of 460 ± 10 ns near the excitonic Mott state $\nu_{max} = 1$. At longer times, the excitonic decay speeds up again with a decay time that corresponds to the value found at lower initial densities. We obtain these values by fitting two exponentials (linear fits in a semi-log plot) and extracting the decay lifetimes, as shown in Figure 6.6c. We also define a transition time t_{tr} between the slow and fast emission regimes. A further increase of the excitation power past that which is necessary to establish the excitonic Mott state has no notable effect on the decay dynamics, which resembles the unit-filling behavior, as shown in the inset of Figure 6.6b. This indicates that excitons in doubly occupied sites (IXX) generated at high

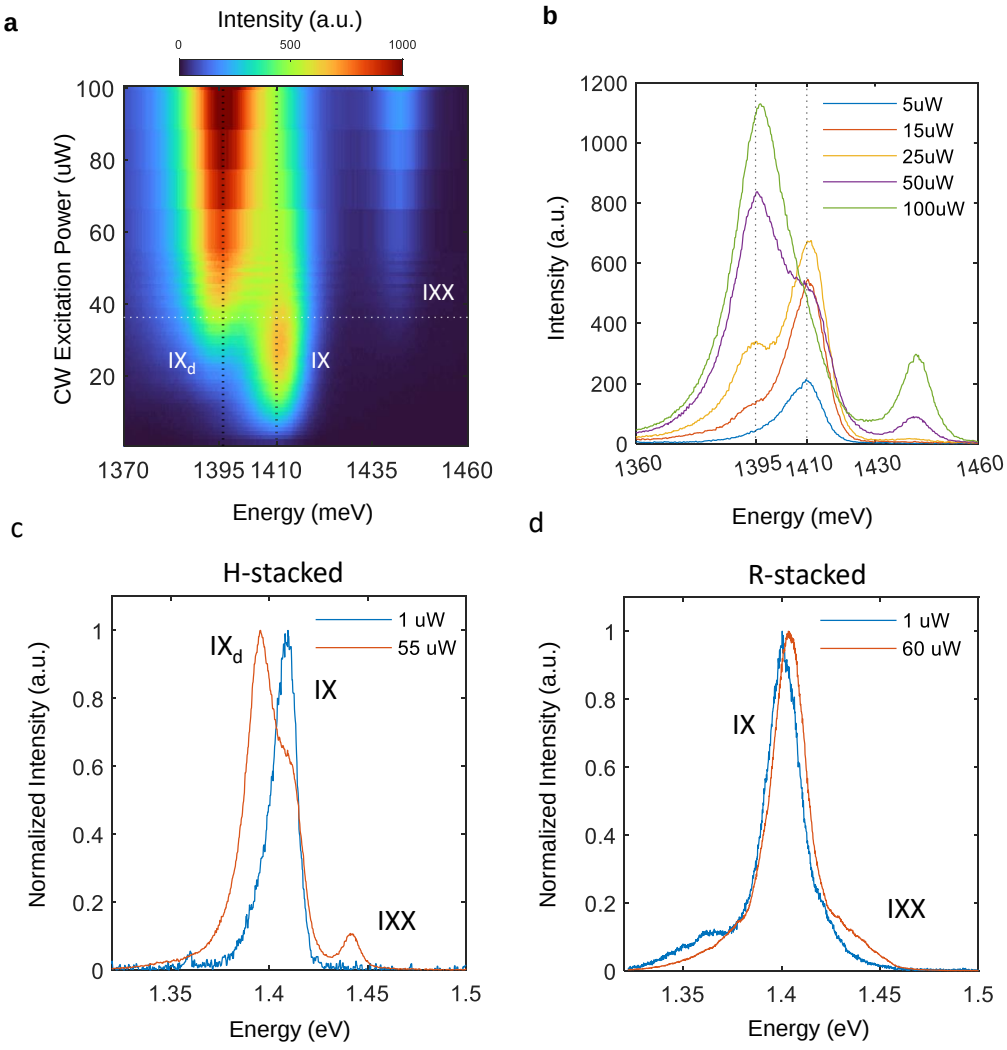

Figure 6.3: Red-shifted IX emission at high excitonic density. **a.** IX PL as a function of excitation (640nm CW laser) power at charge neutrality. The horizontal dashed line indicates the power at which IXX appears. **b.** Select spectra from panel **a** showing an IX_d red-shift of 15 meV. The IX_d peak appears before IXX and increases with power, at the expense of the IX peak. **c.** Normalized IX PL spectra at a low and high (640nm CW laser) power, in the H-stacked region of the sample. **d.** Normalized IX PL spectra at a low and high (640nm CW laser) power, in the R-stacked region of the sample.

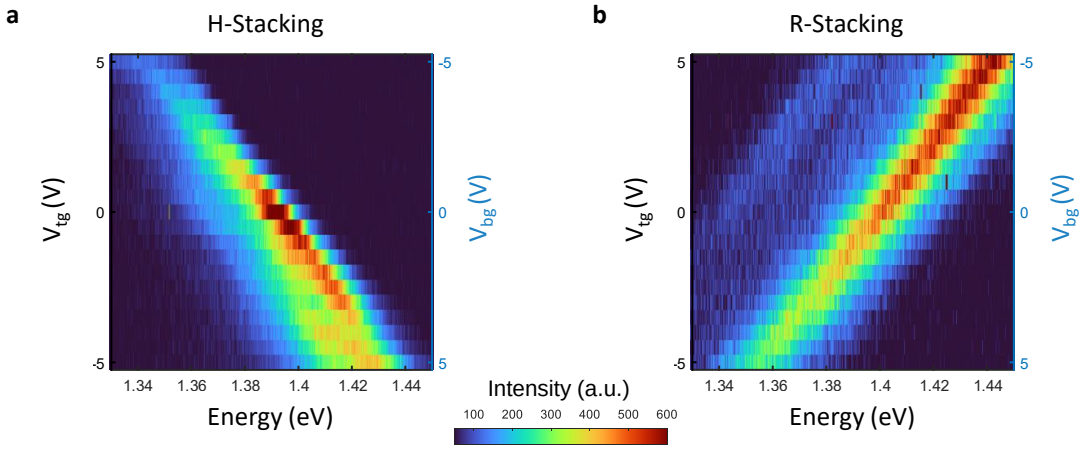

Figure 6.4: Comparison of the Stark Effect at the R- and H- stacked positions. **a.** Electric-field dependence of photoluminescence at the H-stacked position. **b.** Electric-field dependence of photoluminescence at the R-stacked position, showing the opposite dipole to the H-stacked position.

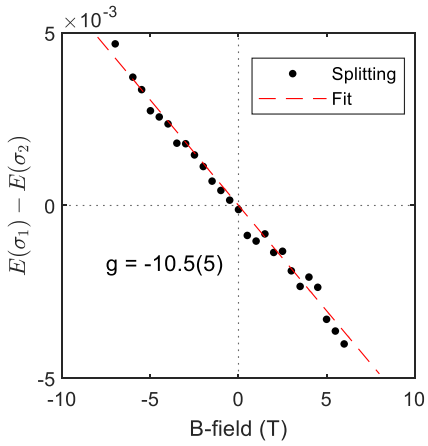

Figure 6.5: Landé g-factor of the H-stacked IX. Magnetic-field dependent splitting of the IX reveals a g factor with a magnitude of 10.5(5). Previous works established the R-stacked g-factor value as close to the monolayer value of 4 [15], and the H-stacked value to be in the 10-14 range [116].

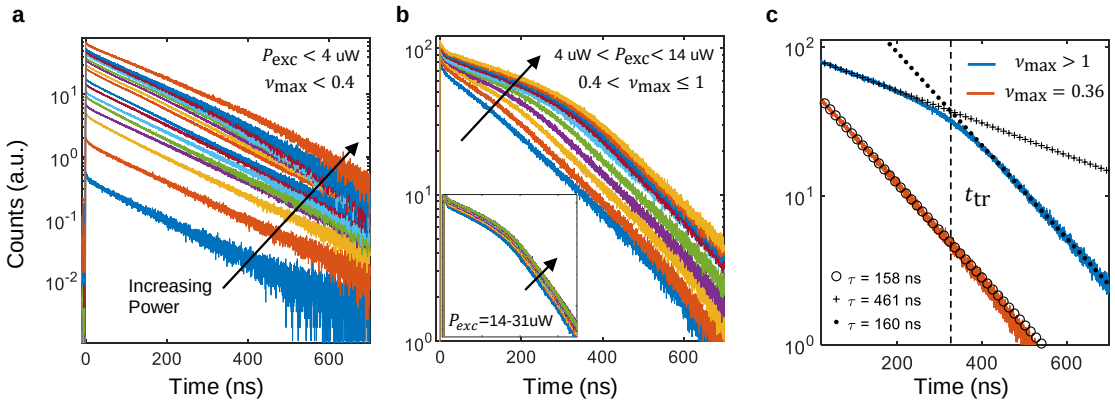

Figure 6.6: Temporally and spectrally resolved IX emission in the H-stacked region. **a.** IX emission decay for the low excitation power regime ($\nu_{\max} < 0.4$). The decay is exponential and lifetime is constant over the entire power range. The power indicated in panels **a-c** of this figure is the average excitation power, using a 640 nm, 1 MHz pulsed laser. The collected emission in panels **a-c** of this figure is filtered to only include IX and IX_d. **b.** IX emission decay for the intermediate excitation power regime ($(0.4 < \nu_{\max} < 1)$). The decay becomes initially slower, then returns to the low-density decay rate. Inset shows IX emission decay for the high excitation power regime ($\nu_{\max} > 1$). The slowing effect has saturated beyond the excitonic Mott state. Axis scaling and limits on the inset are same as in parent figure. **c.** IX emission decay of a high (blue) and low (orange) excitation density case. The fits show the slow and fast decay rates occurring at the high and low density case, respectively. Dashed line indicates the time of transition $t_{\rm tr}$ from the slow to the fast decay regime, corresponding to a density $\nu_{\rm tr}$.

excitation power undergo rapid decay, leaving behind a near-unit-filled lattice. The observed decay dynamics, indeed, come as a surprise, as an increased exciton density often accelerates decay because of non-radiative processes [117, 118] and fast decay processes typically tend to first deplete the rapidly decaying components, generically leading to fast decay followed by a slow decay [119, 120, 121].

For a more detailed analysis, we fit the data in Figure 6.6a,b by two exponentials in the same manner shown in Figure 6.6c and obtain the transition time, $t_{\rm tr}$ for each excitation power. By integrating the decay curve before and after this point, we are able to determine the filling fraction, $\nu_{\rm tr}$, of excitons that have not decayed at the transition time, as we can determine the initial filling fraction using the method

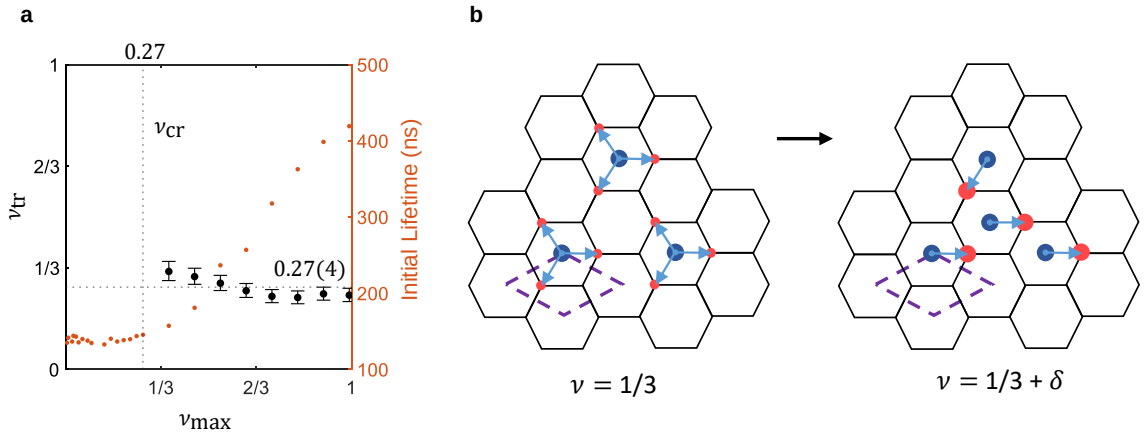

Figure 6.7: IX Decay Dynamics Transition near 1/3 Filling. **a.** Left axis (black) shows the transition fraction ν_{tr} as a function of the inital density ν_{max}. Dashed line indicates the mean observed ν_{tr} of 0.27 (4). Note that ν_{tr} is expressed in units of ν_{max}. Error bars derived from the range of possible intersection point of the two fits, using the uncertainties of the fitted parameters. Right axis (orange) shows the initial (first 100 ns) lifetime of emission as a function of the initial density ν_{max}. The power at which $\nu_{max} = \nu_{cr}$ is indicated by the dashed line, and coincides with the point where a slower initial lifetime is first measured. **b.** Schematic of quadrupolar excitons at 1/3 filling. Moire unit cell is indicated in purple dashed lines, and the hexagonal full lines indicate the effective electronic lattice, with each electron site at the center of a hexagon. At 1/3 filling, assuming a homogeneous exciton distribution, every empty site is adjacent to at least one quadrupolar exciton. When an additional exciton is added, it necessarily resides next to three neighbors and may form an attractive state.

outlined in Section 5.1. Figure 6.7a shows ν_{tr} as a function of the initial filling ν_{max}, and demonstrates that the exciton decay rate changes dynamically at the same filling fraction of $\approx 0.27 \pm 0.04$. In the same panel, we also show the initial decay lifetime as a function of ν_{max}. As discussed above, the initial decay time remains independent of filling until a critical value ν_{cr} followed by a gradual increase to a three-fold value at $\nu_{max} = 1$. Remarkably, this critical value $\nu_{cr} \approx \nu_{tr}$ coincides with the filling fraction at which the dynamical transition between the two decay regimes occurs. This provides strong experimental evidence that the observed decay characteristics is indeed related to the exciton density, causing a slowdown of photon emission above a lattice filling of $\sim 1/3$.

6.1.2 Modelling the IX Decay Dynamics

In order to understand the slow-to-fast transition of the decay, we first focus on the filling fraction $\nu_{\mathrm{tr}} \approx 1/3$, which marks the transition between faster asymptotic decay and slower initial decay. As depicted in Figure 6.7b, for fillings above $\nu_{\mathrm{max}} = 1/3$, there would be a guaranteed overlap of either electrons or holes if all excitons were to remain quadrupolar. For two adjacent excitons the strong onsite Coulomb repulsion between holes ($\sim$ 40 meV, as measured in Figure 5.2) exceeds the energy gain from hybridizing the three states of each exciton. This implies a constraint on hole delocalization leading to a destabilization of the quadrupolar IX in favor of a polarized dipolar IX, as shown in Figure 6.7b. Therefore, for $\nu_{\mathrm{max}} > 1/3$, the ratio of dipolar to quadrupolar excitons increases. Indeed, this critical density is close to the observed values of ν_{tr} and ν_{c} for the transition between slow and fast decay.

Let us now consider the effect of such a polarization of the quadrupolar exciton on its radiative decay rate. For a given electron position in the lattice, an isolated moiré exciton ($\nu_{\mathrm{X}} < 1/3$) can bind in one of three degenerate states, corresponding to different orientations of the excitonic dipole (static) and which we denote as $|1\rangle$, $|2\rangle$, and $|3\rangle$, as shown in Figure 6.8a. The rate, γ_{d} of photon emission from each of these polarized dipolar states is proportional to the square of the transition dipole moment ($\hat{d}$)

$$\gamma_{\mathrm{d}} \propto |\langle i|\hat{d}|0\rangle|^2 \quad , \, i = 1, 2, 3 \tag{6.1}$$

where $|0\rangle$ denotes the vacuum state at a given site. Owing to their threefold rotational symmetry, we expect isolated moiré excitons to form a hybridized superposition state $|Q\rangle = \frac{1}{\sqrt{3}}(|1\rangle + |2\rangle + |3\rangle)$. In fact, this quadrupolar exciton can be considered as a few-body superradiant state (Figure 6.8b), which – due to its deep sub-wavelength

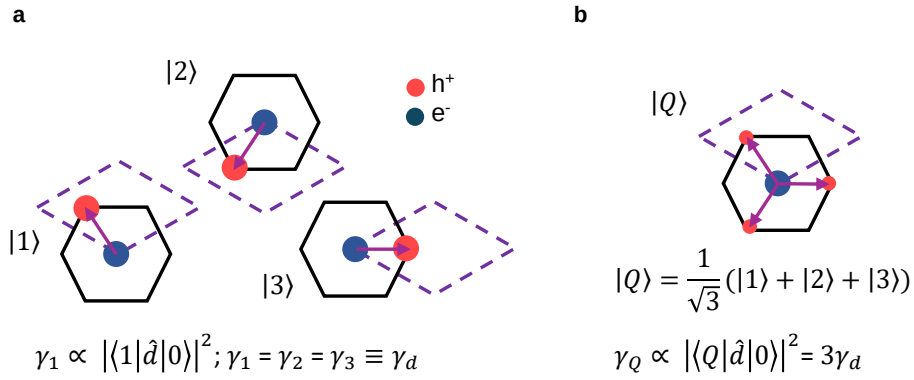

Figure 6.8: Diagram of Quadrupolar and Dipolar IX Lifetimes. Diagram of decay rates of excitons with static in-plane **a.** dipolar and **b.** quadrupolar moments. Excitons with a static dipolar moment form a triply-degenerate basis, due to the triangular symmetry of the H-stacked potential. The oscillating dipole moment of the static quadrupolar state (γ_{Q}) is an equal superposition of the oscillating dipole moments of the static dipolar states (γ_{d}), and is expected to have a 3x faster collective decay rate ($\gamma_{\mathrm{Q}} = 3\gamma_{\mathrm{d}}$). Purple dashed lines indicate moire lattice edges.

spatial extent – features a collectively enhanced photon emission rate

$$\gamma_Q \propto |\langle Q|\hat{d}|0\rangle|^2 = \left|\frac{\langle 1| + \langle 2| + \langle 3|}{\sqrt{3}}\hat{d}|0\rangle\right|^2 = 3\gamma_d. \tag{6.2}$$

Note that the transition dipole moment ($\hat{d}$) is unrelated to the static dipole, such that the polarization of emitted photons does not depend on the orientational state ($|i\rangle$) of the static dipole. Hence, we conclude that the fully hybridized quadrupolar exciton should decay three times faster than a polarized dipolar exciton.

In order to fully characterize our measured decay time dynamics, we also turn our attention to the period while IXX is still bright. Figure 6.9a shows the lifetimes of the IXX peak in comparison to the significantly longer-lived IX peak. Recalling that the IXX is a doubly-excited state of the moiré site, the substantial presence of IXX at small delays from the excitation laser means that the IX signal is suppressed. Each IXX decay event is correspondingly an addition of an IX site to the system. This

creates a brief non-monotonic 'hump' at the beginning of the IX trace, as seen in Figure 6.9b. In order to account for the observed non-monotonic IX emission at early times in high excitation power experiments, we made a simple differential equation model which shows how the rapid decay of the initial IXX population 're-pumps' the IX numbers and leads to the initial 'hump' in our lifetime measurements. The data shown in Figure 6.9b was taken at the highest measured power, where we can approximate the initial population to be fully IXX across the whole excitation spot. Then, we can initialize the populations of IX and IXX as:

$$N_{\mathrm{IX}}(t=0)=0; N_{\mathrm{IXX}}(t=0)=10000;$$

where 10000 is an approximate number of sites in our excitation spot.

Since we know the radiative rates of IX and IXX, γ_{IX} and γ_{IXX}, we can employ related rates equations, solving for N_{IX} and N_{IXX} as functions of time:

$$N_{\mathrm{IXX}}(t+dt)=N_{\mathrm{IXX}}(t)(1-\gamma_{\mathrm{IXX}}dt)$$

$$N_{\mathrm{IX}}(t+dt)=N_{\mathrm{IX}}(t)(1-\gamma_{\mathrm{IX}}dt)+N_{\mathrm{IXX}}(t)\gamma_{\mathrm{IXX}}(t)dt$$

We numerically evaluate the result with a time step much smaller than the lifetimes ($dt = 0.01$ ns). In Figure 6.9b, we compare the calculated intensity of IX emission as a function of time ($I_{\mathrm{calc}} = -N_{\mathrm{IX}}(t)\gamma_{\mathrm{IX}}$) to the observed emission data and find good agreement. This effect was also accounted for in comparing our data to simulations in Figure 6.13, by using the point immediately after the hump as the starting point for our analysis, avoiding the effect of IXX.

In order to further examine our claim of dipole-dipole intercell interactions, we study the time-resolved PL spectra (TRPLS) in the H-stacked region using the method from Section 4.2.6 in order to compare the energies from IX and $\mathrm{IX_d}$ in

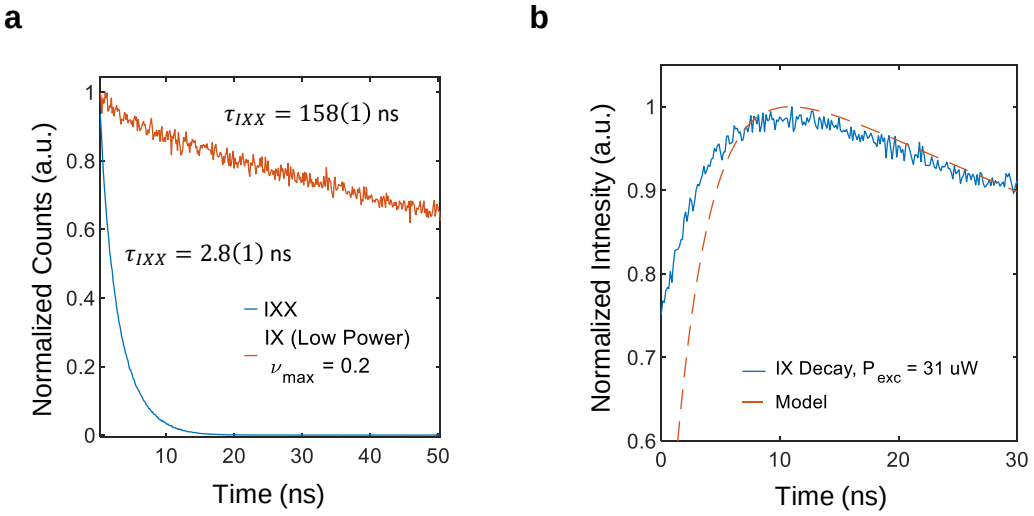

Figure 6.9: Effect of IXX on Measured IX Dynamics. **a.** Comparison of lifetime of IX and IXX. IXX lifetime is about two orders of magnitude shorter. **b.** Comparison of early (first 30 ns) decay profile of IX at a high excitation power (31 uW) and the IXX 're-pumping' model.

the two lifetime regimes. Figure 6.10a shows the TRPLS at low excitation power, where we observe a single exponential decay rate at $3\gamma_d$, as in Figure 6.6a. The energy of emission shifts red by $\sim$ 3 meV (Figure 6.6b) from the initial emission to the long-time limit, suggesting that the decreasing density is reducing the long-range z-dipole repulsion, an effect also observed in R-stacked samples (Figure 6.3d). The high-power measurements indeed show the presence of IX_d, as shown in Figure 6.6c. In fact, the spectrum at early times is entirely dominated by IX_d, with the emission energy then gradually transitioning into IX. Comparing the energy spectra with the lifetime dynamics, as in Figure 6.6d reveals that the period of red-shift back to the IX energy coincides with the slow emission regime in lifetime. The observed time evolution is therefore consistent with a ferroelectric phase at high excitonic densities that feature a lowered energy due to the in-plane attraction of aligned dipolar excitons, and whose energy rises as excitons decay until a filling of $\sim 1/3$ where the system starts to become primarily composed of isolated, quadrupolar excitons. We

also confirm that the TRPL measurements are consistent with our lifetime decays by comparing the integrated TRPL counts in the same spectral region as our filters for the lifetime measurements with the decay traces from the APD in Figure 6.11.

As the observed IX_d peak has a similar energy to the IX_e observed in Figure 5.2, it is important that we investigate the possibility of unintentional photo-doping as a reason for our observations of a red-shifted peak at higher excitation powers. Figure 6.12 shows a comparison of an intrinsic (undoped) decay curve past full excitonic filling and a doped decay curve with electron doping slightly above the 1/7 filling and the same excitation power. We see that, though the emission is red-shifted by IX_e, the slow to fast lifetime trend is not observed.

In order to quantitatively analyze our results we developed microscopic simulations of the observed decay dynamics using a Monte Carlo approach, which is detailed in Appendix B. For a given spatial configuration of excitons in the lattice, we perform a Monte Carlo sampling of their dipoles, including the orientational constraint due to electron-electron and hole-hole on-site repulsion. This yields corresponding decay rates which are used to propagate the system via Monte Carlo sampling of stochastic quantum jumps. For example, if an exciton is able to rotate to all three dipolar positions without impeding on other, already present excitons, the decay rate of that exciton is the full $3\gamma_d$. However, if one of the sites is blocked, then only two configurations are allowed and the rate is $2\gamma_d$. Lastly, an exciton completely surrounded has the decay rate γ_d. In order to obtain a base understanding of the slow-down phenomenon, this simulation only accounts for on-site energy U_{XX}, without considering V_{XX}, which we will consider later. The excitons were assumed to avoid being nearest neighbors up to a filling of 1/3, as our proposed attractive interaction is short range ($\sim 1/r^6$), whereas the dipolar repulsion from their z-direction permanent dipole component (see Figure 6.1) scales as ($\sim 1/r^3$), making it dominant at low densities. The simulation outputs an expected decay trace as a function of initial density, as

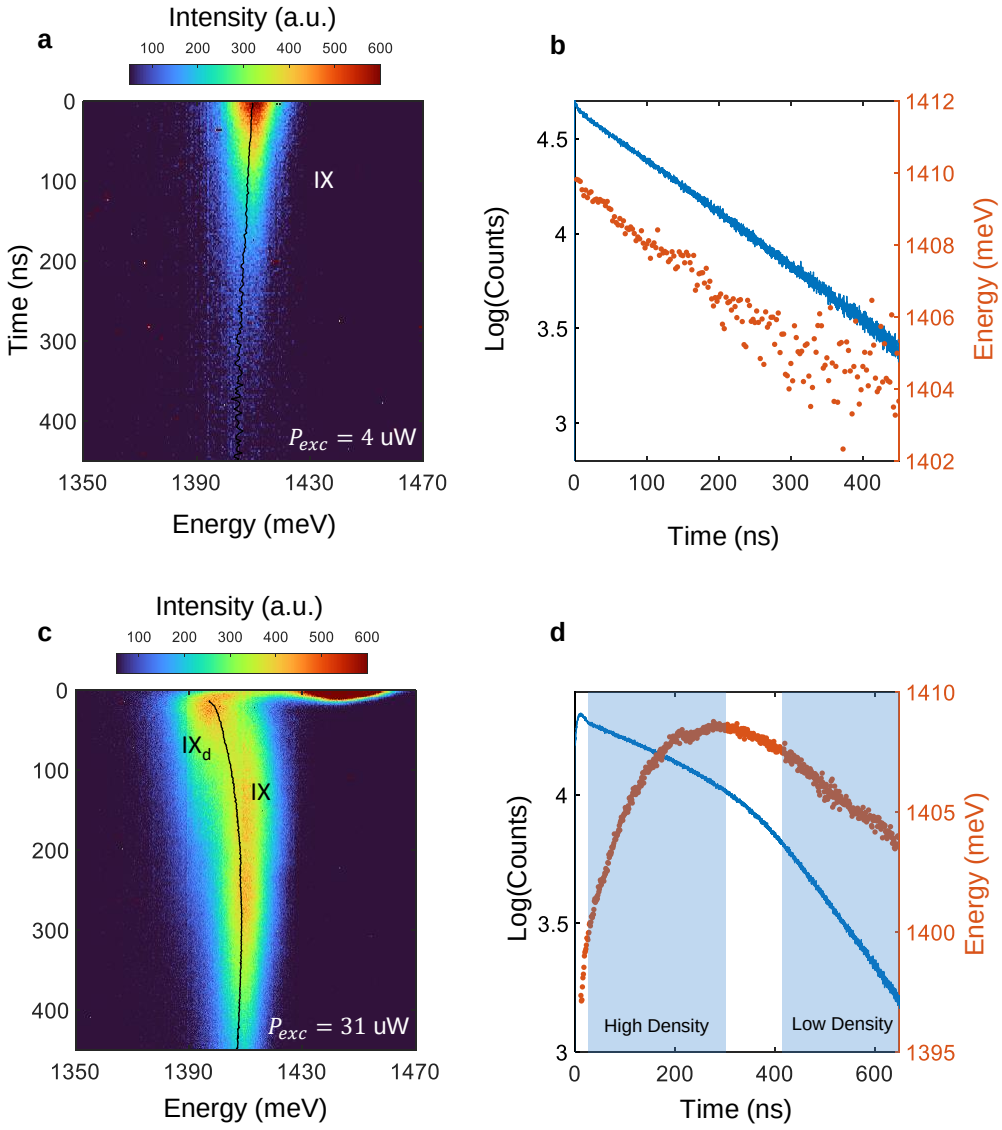

Figure 6.10: TRPLS Measurement of IX Dynamics. **a.** Time-resolved IX spectrum at $\nu_{\max} = 0.4$, using a 640nm pulsed laser. Black line indicates fitted peak center. **b.** Time-resolved IX spectrum at $\nu_{\max} > 1$, using a 640nm pulsed laser. Black line indicates fitted peak center. **c.** Decay profile and fitted peak center position of the data in panel **b**. The emission center is initially red-shifted and blue-shifts during the period where the decay is slow.

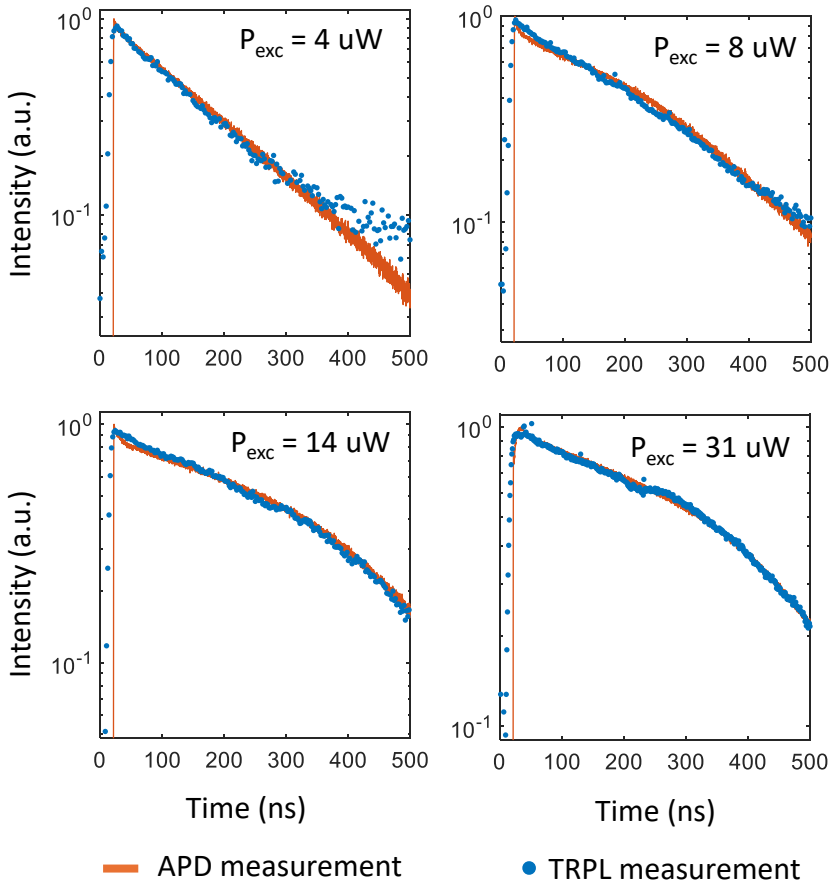

Figure 6.11: TRPLS and APD Measurement Comparison. APD-collected lifetime measurements and the integrated intensity of TRPLS with the same filtered emission range overlap well. Intensities normalized to maximal values.

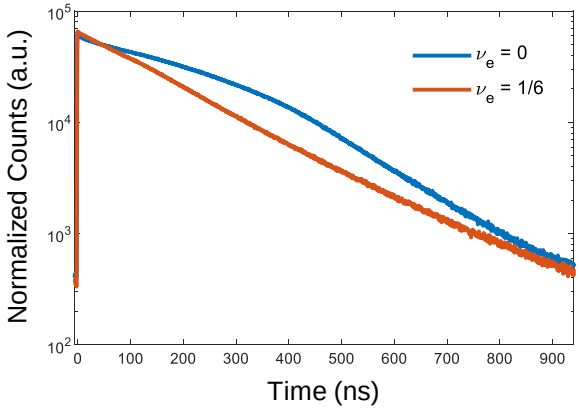

Figure 6.12: Comparison of undoped and 1/6 electron-doped exciton lifetime (14 uW, 1MHz pulsed, 640 nm excitation).

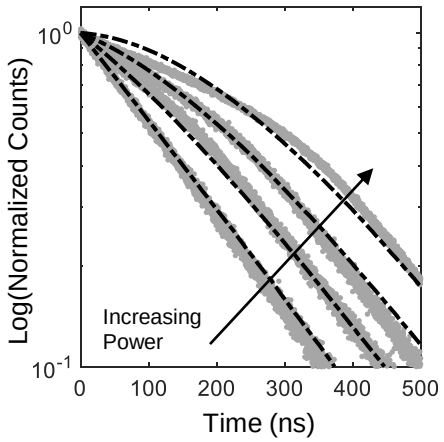

Figure 6.13: Monte-Carlo Modeling of IX Decay. The model (black dashed line) is compared against the decay data (gray). The initial exciton fillings for the data are, in ascending order: 0.16, 0.54, 0.72 and 1; the initial exciton fillings for the simulated data are, in ascending order: 0.13, 0.53, 0.7 and 0.83. The highest density for the simulated traces is reduced compared to the experimental data to account for the measured exciton loss during the period when IXX is still bright, which modifies the decay trace and precludes direct comparison of the traces.

shown in Figure 6.13, where we compare the model to our data. We find fairly good agreement with our data, especially considering the simplicity of the model. At high densities, the simulations yield non-exponential decay dynamics not observed experimentally, and do not reproduced the extended slow regime we observe. This suggests additional weaker orientational constraints due to intercell dipole-dipole interactions that maintain the excitons in a dipolar polarization that are not accounted for.

In order to accurately match the initial conditions of our simulation to our data, we must estimate the average excitonic filling over our collection spot, accounting for the non-uniform intensity profile our excitation beam, rather than simply rely on $\nu_{\max}$, which is a measure of excitonic density only at the center of the beam. In fact, a closer look at the saturation behavior from Figure 5.3 reveals that the transition is 'smeared' compared to the idealized sharp saturation, as shown more clearly by examining the intensity on a linear scale in Figure 6.14. Taking a Gaussian profile excitation intensity (Figure 6.14a), we are able to match the smeared-out saturation

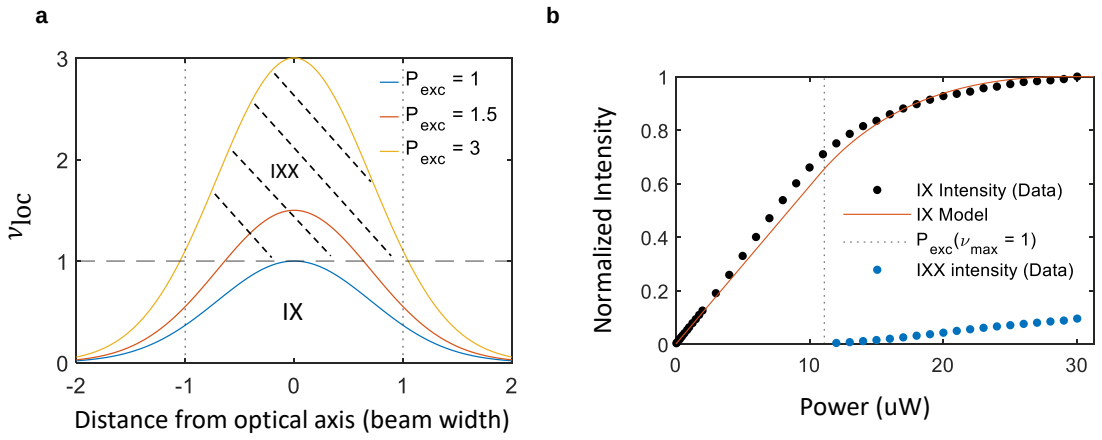

Figure 6.14: Gaussian Excitation Beam Profile Correction to Exciton Density Estimation. **a.** Model of Gaussian excitation beam leading to nonuniform local excitation density across the excitation spot. The excitation power P_{exc} is expressed in units of $P_{exc}(\nu_{max} = 1)$. **b.** Comparison of measured IX intensity to the model in panel a.

behavior reasonably well (Figure 6.14b) and obtain a better quantitative estimate of the initial exciton density ν_X for our simulations. We emphasize that the deviation from the filling estimate obtained through ν_{max} is significant only when saturation begins at higher powers.

We use the $P_{exc}(\nu_{max} = 1)$ power as the estimate of the power needed to locally achieve full filling only at the beam center, and therefore obtain ν_{max} (P_{exc}) by proportionality to this power, much like in Chapter 5. Due to the chromatic abberation of the setup, the excitation spot is larger than the collection spot when using the 640 nm excitation laser, since we optimize our focal length to the collection wavelength of 880 nm. The total filling ν_X in the collection spot is then calculated as a 2D integral, discarding the excess power that would go into forming IXX:

$$\nu_X = \int_0^R \max(\nu_{loc}(x), 1)\ 2\pi r dr, \tag{6.3}$$

where ν_{loc} is the local filling density, given by the Gaussian, and R is the collection spot cutoff. We assume the collection spot has a sharp cutoff, which leads to a

reasonable agreement with the saturation behavior at high excitation powers in our measurements (Figure 6.14b). Using R as the only free parameter in our model, we fit the Gaussian model to the measured intensity, and find that a value of R that equals 1 standard deviation of the Gaussian spot fits the data well. This allows for a more precise mapping of the observed IX intensity to the initial conditions of our simulations.

The Monte-Carlo simulations were extended into the energy domain as well, simulating the evolution of the emitted peak energy as a function of time. Using the same method as described for Figure 6.13 to find the microscopic exciton configurations during the simulated decay dynamics, one can determine the energy of emitted photons from the dipole-dipole interaction energy at every Monte Carlo step. Including a Gaussian linewidth of $\Delta E = 10\,\mathrm{meV}$ to account for typical broadening effects and averaging over many Monte-Carlo runs, we obtain the time-evolving emission spectra. The details of the simulation are given in Appendix B.

Figure 6.15a,b shows the comparison of our measured TRPL spectra and the simulation. There is an observable difference in the extent of the early redshift we measure at 31 uW and 14 uW, despite the fact that both of these powers are above $\mathrm{P_{exc}}(\nu_{\mathrm{max}} = 1) = 11.1(1)$ uW. This is expected in the context of the observation in Figure 6.14 that our IX intensity does not fully saturate across the collection spot at $\mathrm{P_{exc}}(\nu_{\mathrm{max}} = 1)$ due to the Gaussian profile of the excitation beam. Therefore, the observed red shift is also expected to saturate only when the IX density reaches unity filling in the entire collection spot. Using the same initial fillings, the calculations capture the essential features of our TRPLS measurements. In particular, experiment and theory show the characteristic change of the emission spectrum due to the formation of a ferroelectric phase of ordered dipoles at high densities, and that a complete conversion of IX to IX_d is expected at the highest density regime, which matches our measurements (Figure 6.15b). We find that an in-plane dipole moment corresponding

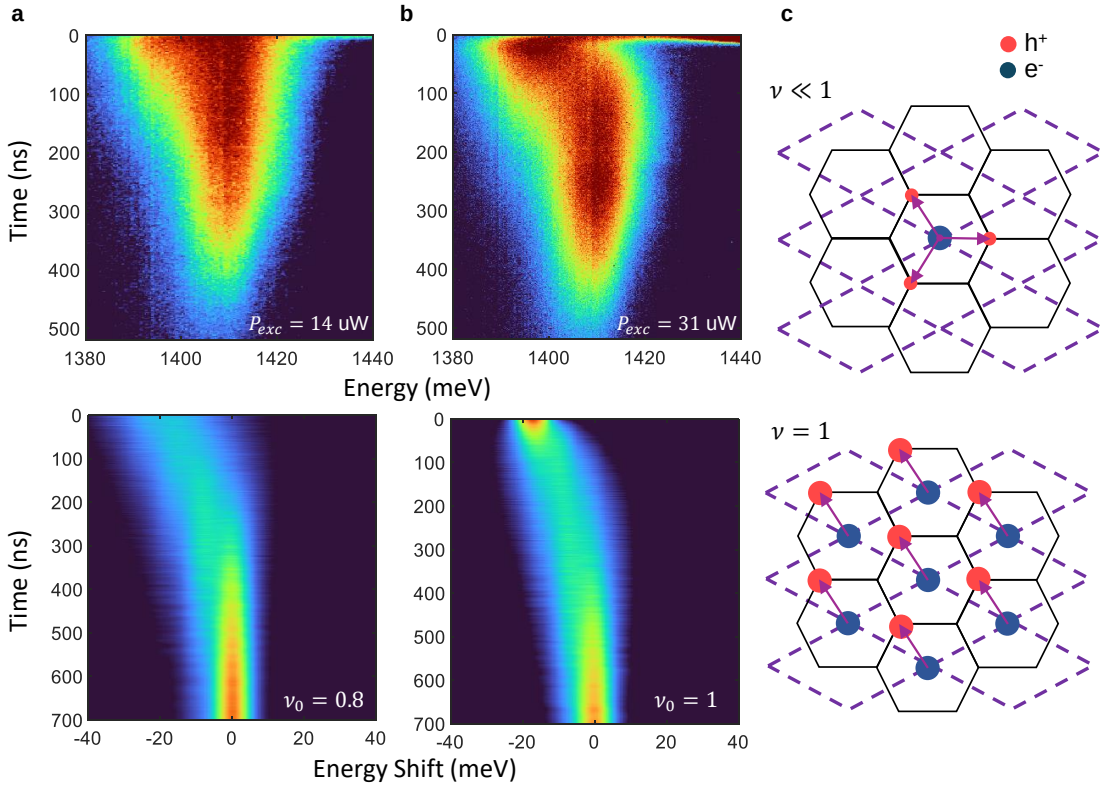

Figure 6.15: Model of the Density-dependent IX Lifetime and Energy Dynamics in the H-stacked Region. **a.** Comparison of measured (top) time-dependent PL at $P_{\text{exc}} = 14$ uW to simulation (bottom). Simulation panels show intensity-normalized spectra to emphasize the emission energy. **b.** Comparison of measured (top) time-dependent PL at $P_{\text{exc}} = 31$ uW to simulation (bottom). **c.** Diagram of transition from quadrupolar, low density exciton to an ferroelectric phase at unit filling.

to ∼70% of the distance between the single-particle potential minima of the electron and hole shown in Figure 6.1 reproduces the observed ≃ 15 meV redshift in the fully polarized ferroelectric phase. Owing to electron-hole attraction, such a reduction in the excitonic electron-hole separation appears reasonable since the moiré-potential depth is comparable to the exciton binding energy [57, 122].

6.2 Conclusion

Our observations reveal a rich interplay between onsite Coulomb interactions, finite range dipole-dipole interactions, and collective photon coupling of excitons that emerges from the presence of in-plane excitonic dipole moments in moiré materials. The physics of ferroelectricity in two-dimensional materials has recently attracted substantial interest, motivated by broad scientific and technological perspectives [123]. The demonstrated dynamical transition to ferroelectric ordering could be combined with an in-plane electric field to tune the spontaneous macroscopic polarization in an optically active quantum material. We also show a mechanism of exciton lifetime acceleration very akin to Dicke superradiance [124], but manifesting due to quantum tunneling of the exciton, rather than mediated by virtual photons.

Chapter 7

Out-of-plane Quadrupolar Excitons and the Excitonic Antiferroeletric Correlations in TMD Trilayers

In this chapter, we study heterotrilayers of WS_2/WSe2/WS_2. Previously, in Chapters 5 and 6, the sample under study featured a trilayer region, where the outer layers were placed in a mutually AB stacking. However, it is also possible to stack the outer layer in an AA configuration. Such a system restores the mirror symmetry about the middle layer. Therefore, is can be expected that, with strong tunneling, charge carriers might delocalize over the outer layer. We exploit this effect to create a new kind of exciton - the out-of-plane quadrupolar exciton, and study its high density behavior. This work was previously published in the journal Nature Materials [125], concurrently with related work from a Stanford group [126]. The DFT calculations featured in this chapter were performed by Dr. Jin Zhang and Professor Angel Rubio of the Max Plank Institute for the Structure and Dynamics of Matter.

7.1 Out-of-plane Quadrupolar Excitons

While in a heterobilayer the static out-of-plane dipole moment of the IX is fixed by the sample geometry, in the heterotrilayer we can exploit the quantum tunneling of electrons to modify this internal structure and add the layer degree of freedom to the IX. Figure 7.1a shows an image of such a sample, which were fabricated using the tear-and-stack technique in order to guarantee no twist angle between the outer layers. As seen from the image, the samples contain both heterobilayer and heterotrilayer regions. Figure 7.1b shows a diagram of the sample. As discussed in Section 2.3.1, the outer gates allow us to apply doping and out-of-plane electric field to the sample. In this chapter, we study 3 different heterotrilayers of WS_2/WSe2/WS_2 with the outer layers aligned at 0°, labeled Sample 1, Sample 2 and Sample 3.

Figure 7.1c illustrates the kinds of excitations in our system. In the heterobilayer, region, the excitons are confined and forced into a dipolar arrangement. However, in the trilayer section, the layer is a degree of freedom for the electron, making two degenerate dipolar states possible, with the direction of the dipole pointing up or down, which we can label as $|\uparrow\rangle$ and $|\downarrow\rangle$. The quadrupolar state forms when the electron tunnels and delocalizes over the two layers and is therefore an equal superposition of the two dipolar states. Since the states are degenerate, the two eigenstates of the total system are a symmetric superposition of the two, which we call the symmetric quadrupolar exciton

$$|Q_s\rangle = \frac{1}{2}(|\uparrow\rangle + |\downarrow\rangle),$$

and the antisymmetric superposition

$$|Q_a\rangle = \frac{1}{2}(|\uparrow\rangle - |\downarrow\rangle).$$

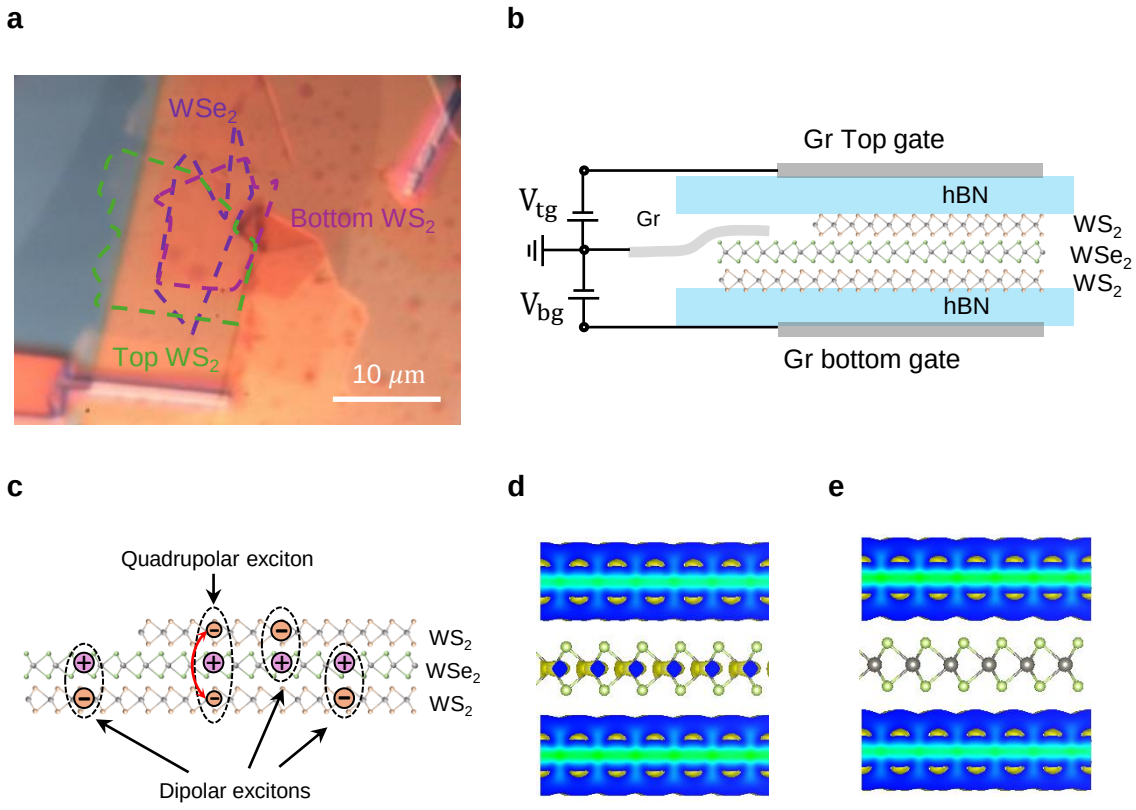

Figure 7.1: Sample Details. **a.** Brightfield image of a trilayer sample. **b.** Schematic of the trilayer sample **c.** Diagram of a quadrupolar and dipolar excitons. **d.** Electron wave-function distribution in symmetric quadrupolar excitons, when delocalized across the two WS_2 layers with a finite weight in the middle WSe_2 layers. **e.** Electron wavefunction distribution in antisymmetric quadrupolar excitons, which is delocalized across the two WS_2 layers with a vanishing weight in the middle WSe_2 layers.

Figures 7.1d,e show the DFT-calculated electron wavefunction of the two configurations (see Appendix C). Notably, the symmetric superposition has a finite weight in the middle layer as an antinode of the symmetric state, whereas the antisymmetric state has a vanishing weight in the middle layer.

In order to characterize these excitons, we begin by studying their photoluminescence (PL). Figure 7.2a shows a comparison between a representative trilayer and bilayer spectrum. We see that the trilayer spectrum shows a three-peak structure., whereas the bilayer shows a single-peak structure with an additional red shoulder. Notably, the energy of the brightest trilayer peak is significantly red-shifted com-

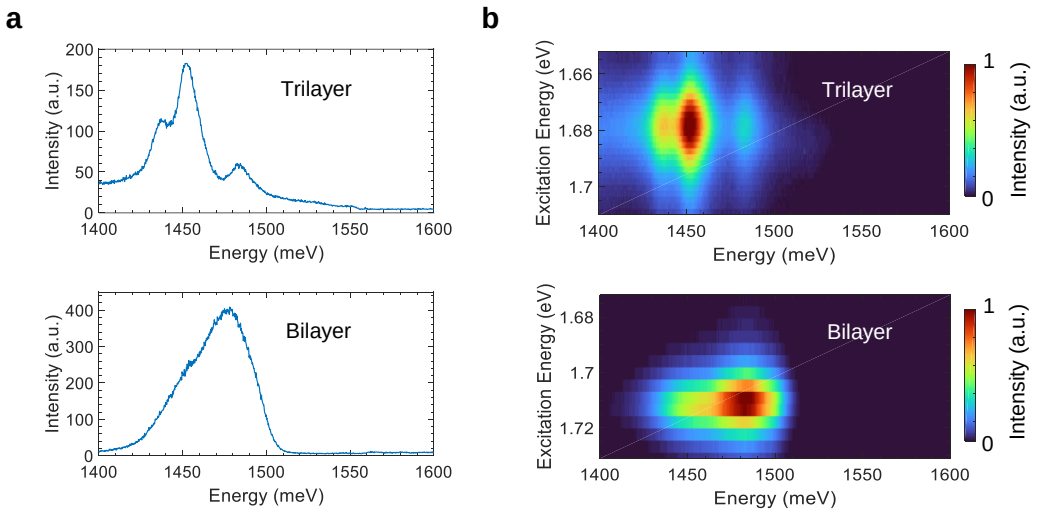

Figure 7.2: Photoluminescence Spectra of Bilayer and Trilayer Regions. **a.** Representative photoluminescence (PL) spectra from the trilayer (top) and bilayer sample regions (bottom). The trilayer shows a three-peak structure, different than the bilayer emission. Excitation was 40 μW of 1.68 eV (1.71 eV) laser for the trilayer (bilayer). The bilayer peak is bluer than the strongest trilayer peak. **b.** Photoluminescence excitation spectroscopy of the trilayer and bilayer region at E = 0. Both regions show one resonance, which is 1.68 eV (1.71 eV) for the trilayer (bilayer).

pared to the bilayer. Figure 7.2a shows the photoluminescence excitation (PLE) spectrum of the trilayer and bilayer. While both resonances are near the typical hBN-encapsulated monolayer WSe_2 value, the bilayer resonance is found at 730 nm (1.71 eV), the trilayer resonance is red-shifted to about 740 nm (1.68 eV).

In order to understand the PL spectra, it is instructive to identify the stacking angle between the outer WSe_2 and the middle WS_2 layers and characterize the moiré potential in the trilayer region. Figure 7.3a,b show that the bilayer region features cross-polarized emission and a g-factor of ~ 14, which are consistent with an H-stacked position, as the analysis in Chapter 6 shows. Therefore, the red shoulder of the bilayer emission in Figure 7.2a may be from the ferroelectric excitons. More importantly, a doping scan of the trilayer region in Figure 7.3c shows no signs of electronic Mott or generalized Wigner states, suggesting that the moiré potential in the trilayer is weak.

Previous work on calculating trilayer moiré potentials emphasized its fragility, in that even in the presence of small lateral strains, the potential would become quasiperiodic and shallow [127]. Therefore, we can conclude that the excitons in the trilayer are not moiré excitons, but free excitons like the scattered states shown in Figure 2.15. This conclusion is also supported by the fact that in samples 2 and 3 we also observe the same three-peak structure with $\Delta E_1 \sim 15$ meV and $\Delta E_2 \sim 30$ meV we observe in sample 1. This kind of uniformity is expected in free excitons, whereas the details of the moiré would likely lead to less homogeneous spectra across samples.

Next, we turn to the electric field $\vec{E}$ dependence of the PL in the bilayer and trilayer regions. The bilayer and the trilayer region are under the same set of gates and hence are subject to nominally the same $\vec{E}$. As shown in Figure 7.4, the PL from the bilayer region shifts linearly, displaying both red and blueshifts depending on the direction of $\vec{E}$. Thus, the bilayer emission behaves as expected for dipolar excitons with an energy shift $\delta\mathcal{E} = -\vec{d}\cdot\vec{E}$ [118]. Moreover, the sign of the slope of the energy shift, $d\mathcal{E}/dE_z$, which is proportional to the dipole moment, is consistent with the layer ordering in the bilayer region. In stark contrast, the PL from trilayer region redshifts for either direction of $\vec{E}$, with a characteristic nonlinear shape as seen in Figure 7.4b. Unlike the dipolar exciton in the bilayer region, $d\mathcal{E}/dE_z$ (or the magnitude of dipole moment) in the trilayer region steadily increases from zero with increasing $|\vec{E}|$, for small $|\vec{E}|$. This behavior is consistent with that of a quadrupolar exciton, which also has a vanishing dipole moment at zero $\vec{E}$, as the diagram in Figure 7.1c indicates.

To gain a qualitative understanding of the nonlinear redshift, we start by considering uncoupled top and bottom dipolar excitons with opposite dipole moments. Under an applied $\vec{E}$, the energy of the two dipolar excitons should shift in opposite directions, resulting in 'X'-shaped dispersing branches, as shown in Figure 7.4c. If we assume a finite hybridization of the two branches due to layer-hybridization of electrons, the intersecting 'X'-like branches should turn into an avoided crossing

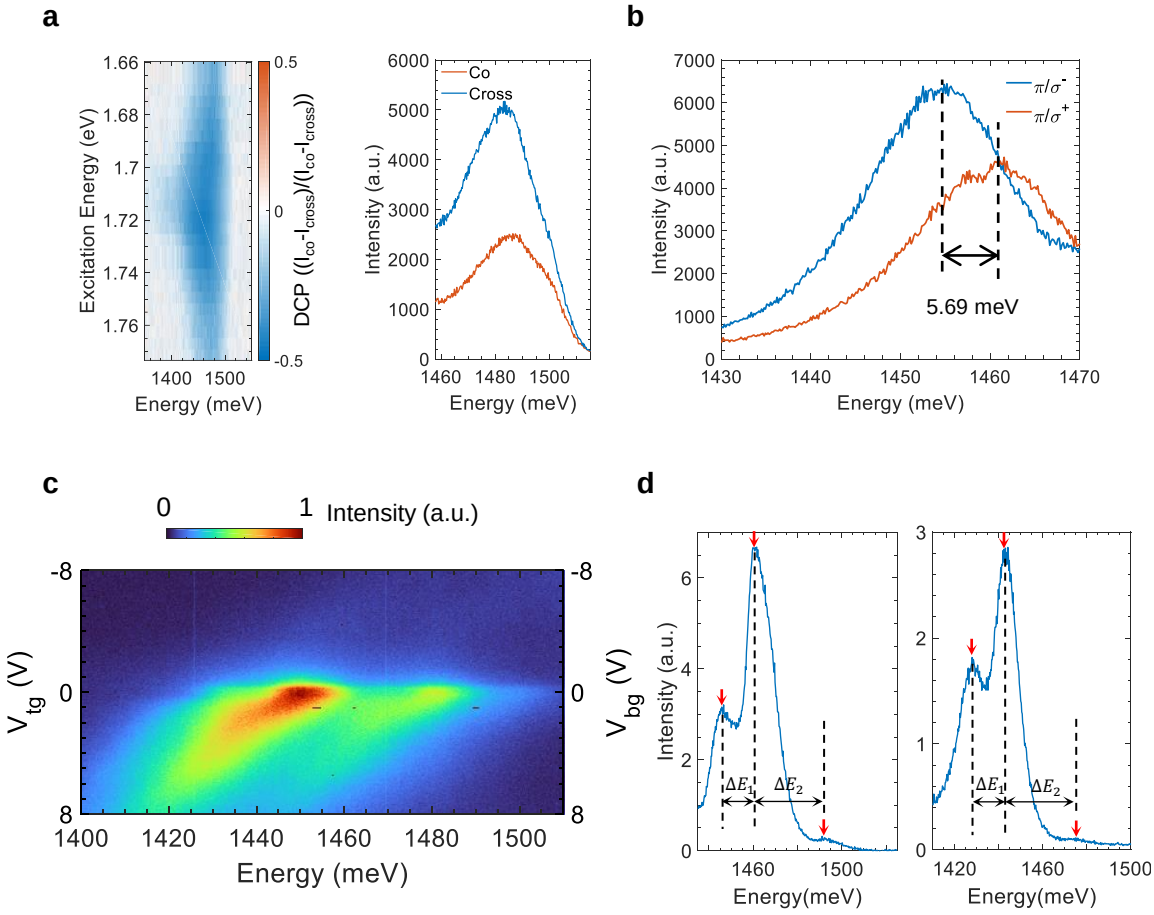

Figure 7.3: Characterization of Sample Stacking Angle and Moiré Potential. **a.** Cross-polarized excitation from the bilayer region of Sample 1, indicating that the middle layer is in a H-stacked configuration relative to the outer layers. **b.** Zeeman splitting of the bilayer region of Sample 1 for a magnetic field of 7 T, indicating a g-factor of 14, also indicating H-stacking. **c.** Doping scan of emission of the trilayer region of Sample 1. Lack of electronic Mott states indicates no significant moiré potential is present. **d.** PL spectrum of trilayer regions of Sample 2 (left) and Sample 3 (right). Both show three peak structures with $\Delta E_1 \sim 15$ meV and $\Delta E_2 \sim 30$ meV.

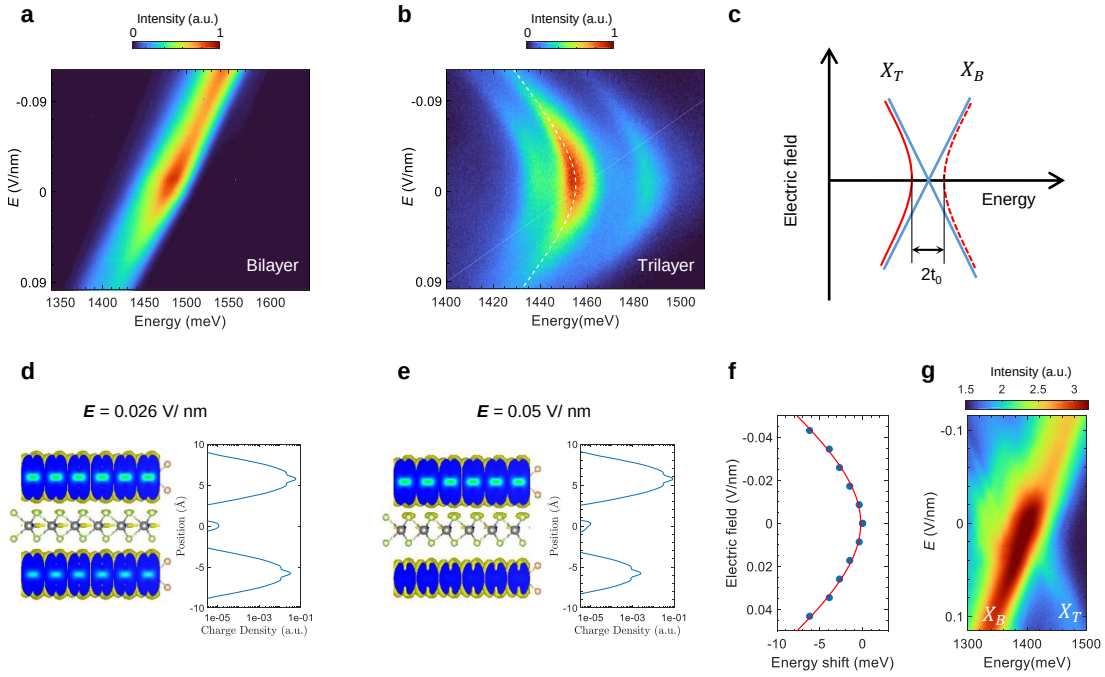

Figure 7.4: Electrical field tunable dipole hybridization in quadrupolar excitons. **a.** Electric field ($\vec{E}$) dependent PL of bilayer excitons in Sample 1. The peak blueshifts or redshifts depending on the direction of the out-of-plane electric field. **b.** $\vec{E}$-dependent PL of trilayer excitons in Sample 1. The dashed white line is a hyperbolic fit of the main peak. The three-peak structure only redshifts with electric field. **c.** Hybridization of the top and bottom dipoles. X_B (X_T) is the bottom (top) dipole and t_0 is the tunnelling strength at zero electric field. The solid red line is the lower energy symmetric branch, and the dashed red line is the higher energy antisymmetric branch. **e, d.** DFT calculation of the electron charge density across the layers at **d** $\vec{E} = 0.026$V/nm and **e** $\vec{E} = 0.05$V/nm. When $\vec{E}$ is increased, the electron density is shifted from the bottom layer to the top layer, and the electron density in the middle layer is reduced. **f.** The solid blue dots represent the shifts of the quadrupolar exciton interband transition energy as a function of $\vec{E}$ from DFT calculations. The red line shows the hyperbolic fit in **(b)**. **g.** $\vec{E}$-dependent PL of an AB stacked trilayer. The top and bottom dipoles do not hybridize. The excitation power is 40 μW for **(a)** and **(b)**, and the excitation energies are 1.71 eV and 1.68 eV, respectively. The excitation power is 5 μW for **(g)** with energy 1.685 eV.

where the lower (higher) energy branch corresponds to the symmetric (antisymmetric) superposition of top and bottom dipolar excitons – quadrupolar excitons [128]. In this case, the lower (higher) energy symmetric (antisymmetric) branch only redshifts (blueshifts), asymptotically merging with the dipolar branch. Thus, we conclude that the redshifting of PL in the trilayer region is consistent with a symmetric quadrupolar exciton. The antisymmetric quadrupolar branch is at higher energy and is expected to be much weaker in emission under non-resonant excitation due to relaxation to the symmetric branch. Furthermore, oscillator strength, which is characterized by electron-hole overlap, is drastically reduced for the antisymmetric quadrupolar exciton because of the presence of a node in the electronic wavefunction at the location of the hole in the WSe_2 layer, whereas the finite wavefunction density of the symmetric state indicates a substantial oscillator strength. The combination of these two effects possibly renders the antisymmetric quadrupolar exciton optically dark in our experiments.

If we assume that the tunnel coupling remains constant with the out-of-plane electric field, then the quadrupolar exciton can be considered as a hybridized state of two possible dipolar excitons - top ($|\Psi_t\rangle$) and bottom ($|\Psi_b\rangle$). Therefore the dipolar basis can be written as:

$$\begin{bmatrix} |\Psi_t\rangle \\ |\Psi_b\rangle \end{bmatrix}$$

Assuming the external E-field points along the direction of the top dipole, the dipolar excitons' Stark shifts are given by:

$$\Delta E_{\mathrm{t}} = -\alpha(e\vec{E} \cdot \vec{d_0})$$

$$\Delta E_{\mathrm{b}} = +\alpha(e\vec{E} \cdot \vec{d_0}),$$

where e is the elementary charge of the electron, $\vec{E}$ is the external E-field, $\vec{d_0}$ is the bare dipole moment of the dipolar excitons, and α is a parameter that accounts for the effects of screening inside the material. Given a hybridization strength between the two dipolar states of t_0, we can write the Hamiltonian in this basis:

$$H_d = \begin{bmatrix} -\alpha(e\vec{E}\cdot\vec{d_0}) & -t_0 \\ -t_0 & +\alpha(e\vec{E}\cdot\vec{d_0}) \end{bmatrix}$$

Upon diagonalization, we find two eigenstates, the symmetric ($|\Psi_s\rangle$) and antisymmetric ($|\Psi_a\rangle$) quadrupolar excitons:

$$\begin{bmatrix} |\Psi_s\rangle \\ |\Psi_a\rangle \end{bmatrix}$$

with the Hamiltonian:

$$H_q = \begin{bmatrix} -\sqrt{\alpha^2(e\vec{E}\cdot\vec{d_0})^2 + t_0^2} & 0 \\ 0 & +\sqrt{\alpha^2(e\vec{E}\cdot\vec{d_0})^2 + t_0^2} \end{bmatrix}.$$

As argued above, we observe only the symmetric branch of the quadrupolar exciton due to its lower energy and higher oscillator strength, and therefore the characteristic hyperbolic Stark shift of the quadrupolar exciton is given by:

$$\Delta E_s = -\sqrt{\alpha^2(e\vec{E}\cdot\vec{d_0})^2 + t_0^2}.$$

We convert the voltage into E-field using the Stark shift of dipolar excitons in the bilayer region and thus $\alpha = 1$ for the bilayer. However, for the trilayer, $\alpha = 0.58$ by fitting the asymptotic line using the same E-field as the bilayer, which is found to be similar across the studied samples. Using the above picture, we can get a rough estimate of the strength of hybridization or tunnel coupling, t_0, between the

two dipolar excitons by fitting the energy shift of the symmetric quadrupolar branch using a hyperbolic function, $\mathcal{E}(\vec{E}) = -\sqrt{t_0^2 + \alpha^2(e\vec{E} \cdot \vec{d_0})^2}$, which yields $t_0 = 16 \pm 5$ meV, assuming that the branch reaches an asymptotic line at maximum $\vec{E}$, where d_0 is the bare dipole moment.

While the above analysis is performed assuming a constant hybridization, t_0, of opposite dipolar excitons, we can obtain a more accurate picture by considering how the layer-hybridized electronic wavefunction evolves with $\vec{E}$. Under an out-of-plane electric field, we can assume that the hole distribution remains unchanged and hence the excitonic energy shift is primarily determined by the changes to the electronic wavefunction. To this end, our collaborators performed DFT simulations to calculate the electronic wavefunction of the symmetric state as a function of $\vec{E}$ (see Appendix C). Figure 7.4d,e show the electronic charge distributions at two values of $\vec{E}$. As expected, with increasing $|\vec{E}|$, the electronic charge distribution becomes asymmetric about the hole in the middle WSe_2 layer, resulting in an increased dipole moment. We calculate the energy shift for the symmetric quadrupolar exciton from this $\vec{E}$-dependent dipole moment as shown in Figure 7.4f. We find very good agreement with our experimental results at the level of DFT calculation, due to similar binding energy of symmetric and antisymmetric branches [128]. We also note that the DFT calculations neglect moiré potential-related effects, as we found the moiré potential to be negligible from the analysis of Figure 7.3. We observe similar $\vec{E}$-dependent nonlinear redshift of PL in the other two samples, as shown in Figure 7.5 which leads us to conclude that it is a generic feature of AA stacked WS2/WSe2/WS2 heterotrilayers.

To further confirm that the observed behavior in the trilayer region is indeed due to tunnel coupling, we also study the sample with AB stacking order of the outer WS_2 layers, which should suppress layer hybridization due to spin-conserving tunneling. This is the same sample featured in Chapter 5 and Chapter 6, and described in

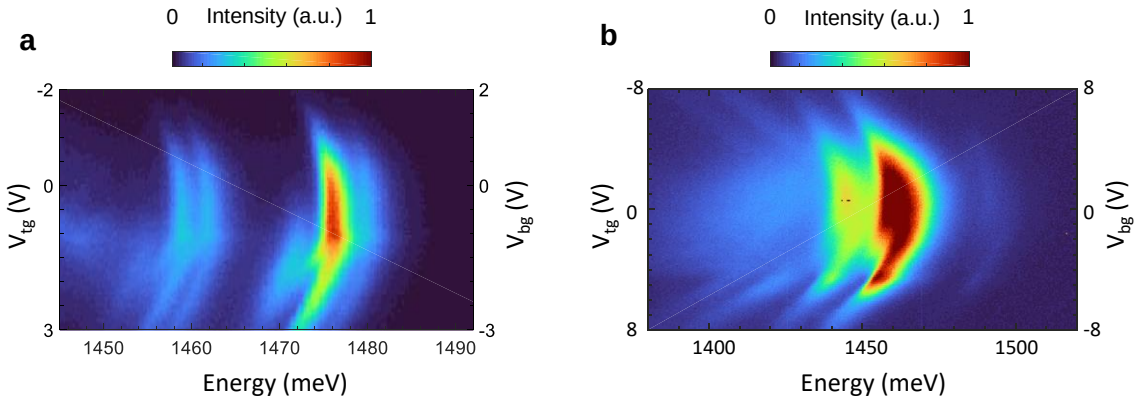

Figure 7.5: Quadrupolar Excitons Across Samples. Electric field scans of PL from **a.** sample 3 and **b.** sample 2, showing the characteristic hyperbolic energy dependence on $\vec{E}$.

Figure 5.1. As shown in Figure 7.4g, we observe dipolar exciton-like response under $\vec{E}$ with the PL displaying linear red and blueshift depending on the direction of $\vec{E}$, as expected from a lack of tunnel coupling. As a result, the AB stacked trilayer is decoupled into bilayers. This is consistent with DFT calculations, as shown in Figure A.1.

7.1.1 Tunable Lifetime of Quadrupolar Excitons

Having established the existence of quadrupolar excitons in heterotrilayers, we study the implications of the quadrupolar exciton wavefunction on light-matter coupling. A key quantity in determining the latter is the overlap of electron and hole wavefunction, which determines the radiative lifetime of the exciton. Owing to the tunneling of electrons through the WSe_2 barrier which hosts holes, the symmetric quadrupolar exciton has a larger electron-hole overlap compared to the dipolar exciton. As the electron-hole overlap in the symmetric quadrupolar exciton depends sensitively on $\vec{E}$, it can be tuned to control excitonic radiative lifetime and hence light-matter coupling.

To test this hypothesis, we performed time-resolved PL lifetime measurement of

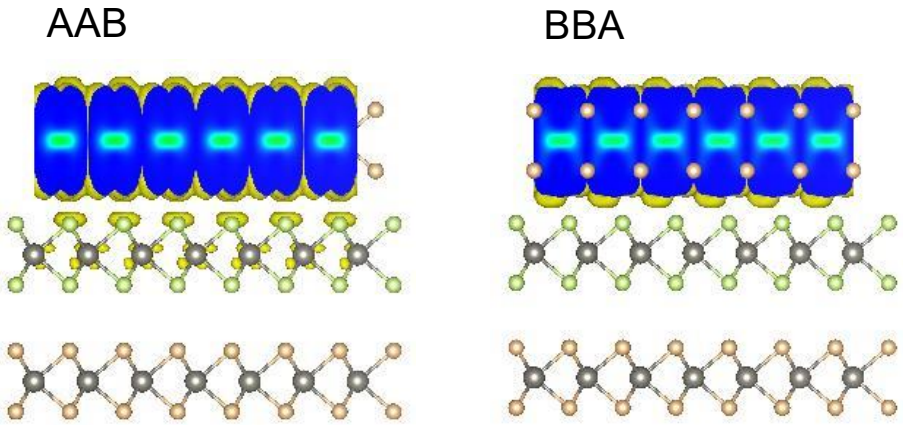

Figure 7.6: DFT Calculation of Electronic Wavefunction for AB Stacked Trilayers. DFT calculations show that, for an AB stacking of the outer layers, the electron cannot hybridize across the layers regardless of the way the top layer is translated with respect to the bottom two, which is the difference between the AAB and BBA case.

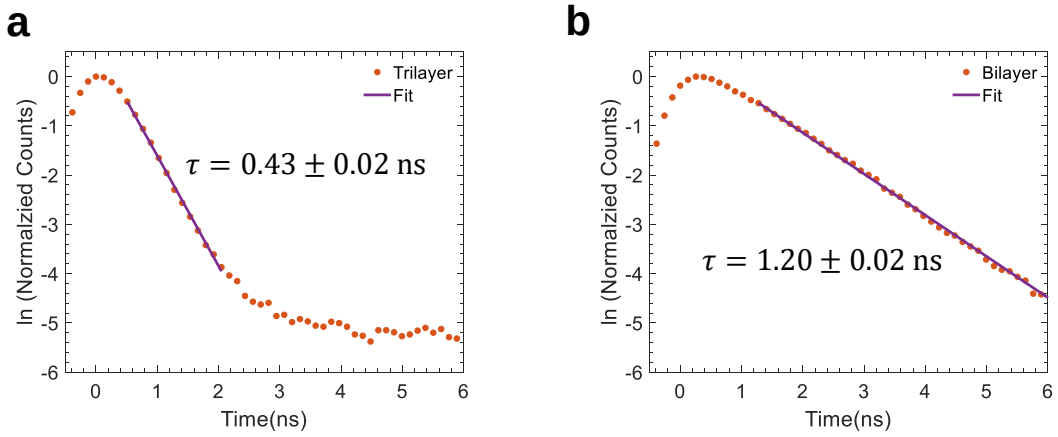

Figure 7.7: Lifetime Comparison of **a.** trilayer PL and **b.** bilayer PL in sample 1.

the emission from bilayer and trilayer regions as a function of $\vec{E}$. Firstly, we compare the PL lifetimes in the trilayer and bilayer regions, and find that the lifetime in the trilayer region (0.43(2) ns) is shorter than in the bilayer region (1.20(2) ns), as shown in Figure 7.7, which is in line with our analysis above.

Next, we analyze the electric-field dependence of the quadrupolar exciton lifetime in the trilayer region of Sample 2. As shown in Figure 7.8a and c, with increasing $|\vec{E}|$, PL lifetime of the heterotrilayer steadily increases from ~ 0.4 to 0.7 ns. As the PL lifetime depends on both radiative and non-radiative lifetimes, an increase in PL lifetime could arise from a reduction in non-radiative processes or an increase in radiative lifetime, or a combination thereof. The presence of a small out-of-plane electric field should have a minor effect on the non-radiative lifetime. In fact, any unintentional doping under $\vec{E}$ will only decrease the non-radiative lifetime by carrier-induced relaxation. Thus, we attribute this increase in lifetime to reduction in electron-hole overlap of the quadrupolar exciton with a polarizing $|\vec{E}|$. In contrast, Figure 7.8b,d show that the bilayer region lifetime has negligible change for $\vec{E} < 0$. The decrease in PL lifetime of bilayer region for $\vec{E} > 0.03$ V/nm is consistent with the observed reduction in PL intensity in Figure 7.4a possibly arises from non-radiative relaxation due to unintentional carrier doping. The trilayer region of Sample 1 also shows an increased lifetime with $\vec{E}$ but by a smaller amount, as shown in Figure 7.9.

7.2 Excitonic Out-of-plane Antiferroeletric Correlations

7.2.1 Quadrupolar to Dipolar Density-Driven Transition

As neutral quasiparticles, excitons in general interact weakly, but dipolar excitons can interact strongly via dipole-dipole interactions at sufficiently large excitonic den-

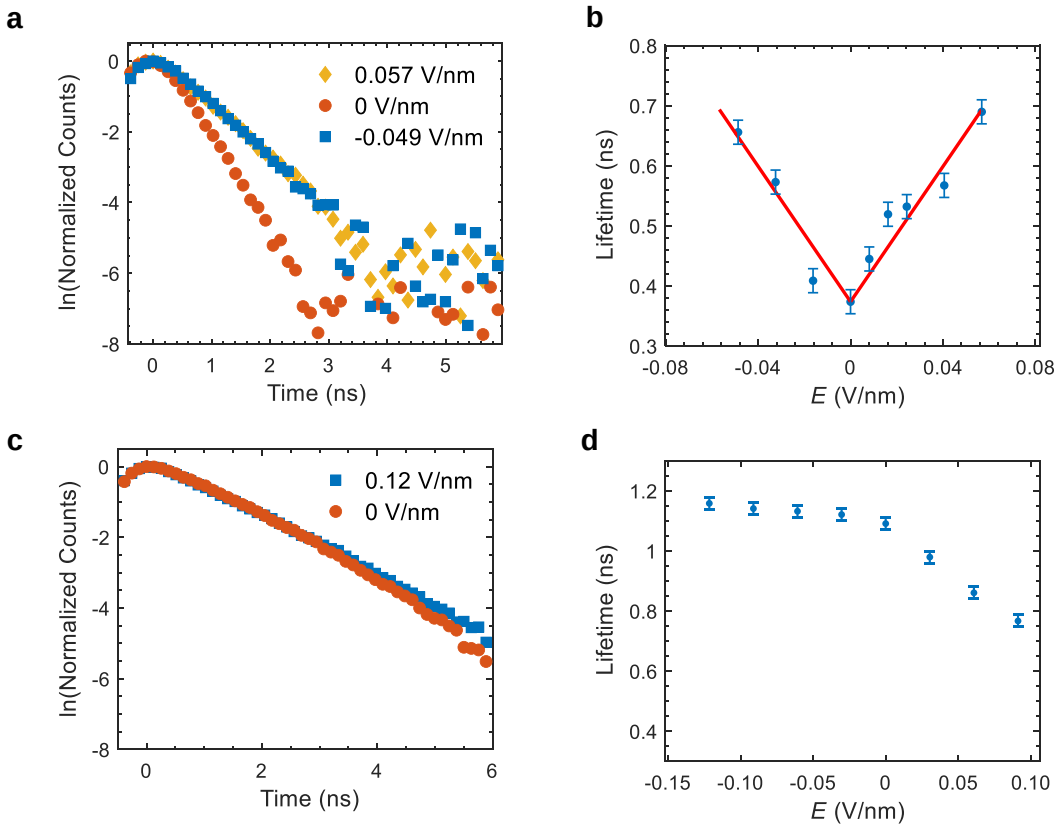

Figure 7.8: Electric-field Tunable Lifetime of the Quadrupolar Exciton. All data in this figure is from Sample 2. **a.** Time-resolved PL of the trilayer exciton with a positive, negative and zero $\vec{E}$. **b.** Time-resolved PL of the bilayer exciton as a function of $\vec{E}$. **c.** Fitted lifetime of the trilayer exciton as a function of $\vec{E}$. Error bars ($\pm$0.02 ns) indicate uncertainty of the exponent in a single exponential fit. The trilayer exciton lifetime increases with $\vec{E}$ in either direction. The red line is the linear fit of lifetime versus $\vec{E}$, which gives a slope of 5.7 $\pm$ 0.6 ns/(V/nm) at negative voltage and a slope of 5.7 $\pm$ 0.5 ns/(V/nm) at positive voltage. **d.** Fitted lifetime of the bilayer exciton as a function of $\vec{E}$. Error bars ($\pm$0.02 ns) indicate uncertainty of the exponent in a single exponential fit. The bilayer lifetime has negligible $\vec{E}$ dependence, and the apparent lifetime reduction on the positive field side is due to non-radiative decay caused by slight unintentional doping.

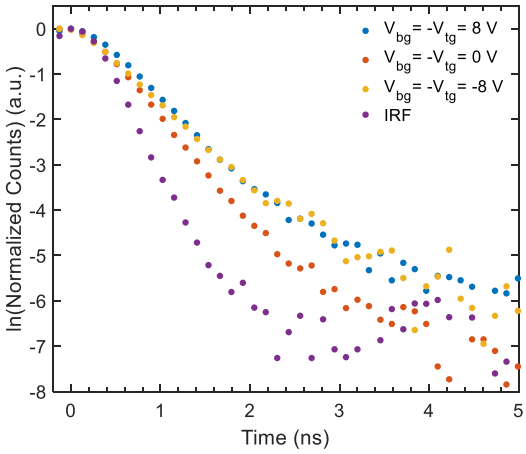

Figure 7.9: Electric-field Tunable Lifetime of the Quadrupolar Exciton in Sample 1. The fitted lifetime at V_{bg} = 8, 0, -8 V is 0.53, 0.43, 0.55 with an error bar of ± 0.02 ns, respectively. Both directions of the electric field increase the lifetime of the quadrupolar exciton. All the lifetime measurements are above the IRF of 0.27 ± 0.02 ns.

sities [19, 110, 21]. Whereas interlayer dipolar excitons in heterobilayers interact repulsively, repulsive quadrupolar interactions between hybridized excitons in heterotrilayers are expected to be weaker. However, the additional WS_2 layer can qualitatively modify the picture such that exciton-exciton interactions and excitonic internal structure couple strongly resulting in correlated excitonic phases and quantum phase transitions between them [128]. Exciton-exciton interactions can be studied by varying the steady-state excitonic density, n_{ex}, which can be efficiently varied, for example, by changing the intensity of the excitation laser resonant with the intralayer excitonic resonance.

Figure 7.10 shows $\vec{E}$-dependence of PL spectra in trilayer regions of Sample 3 as the excitation laser intensity, resonant with the intralayer WSe_2 exciton, is increased. The power dependence of integrated intensity of trilayer emission shows an almost linear dependence on excitation power up to 1 mW, ruling out significant saturation-induced heating or photo-doping (see Figure 7.11). At a low power of 35 μW (Figure

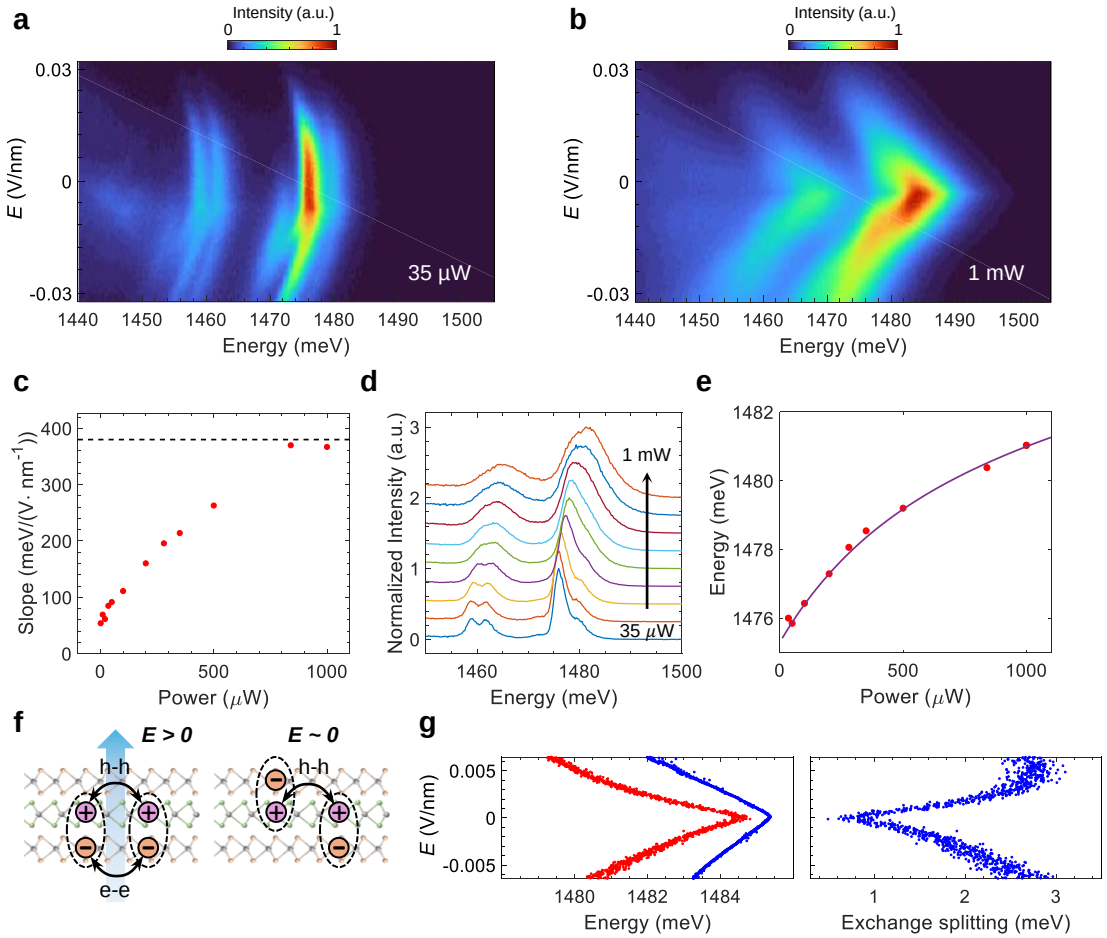

Figure 7.10: Density-driven Quadrupolar to Dipolar Exciton Transition. Data from Sample 3. **a.** Electric field dependence of PL with a low excitation power of 35 μW. Peak energies have a hyperbolic dependence on the gate voltage. **b.** Electric field dependent PL with a high power of 1 mW. Peak energies have a linear dependence on the gate voltage. The laser excitation energy for both **(a)** and **(b)** is 1.696 eV. **c.** Fitted quadrupolar exciton energy shift slope of the top half branches as a function of incident power. The slope increases with the power. The dashed horizontal line is the asymptotic line slope of low power at high $\vec{E}$. **d.** Normalized spectra from 8.4 mV/nm under excitation power of 35, 50, 100, 200, 280, 350, 500, 840, and 1000 μW. **e.** Extracted energies of the strongest peaks from panel **(d)**. The peak energies blue-shift under increased power. The peak energy error bar is ± 0.03 meV. The purple curve is the fitted line according to the model elaborated in Section 7.2.2. **f.** Schematics of exchange interactions at $\vec{E} > 0$ and $\vec{E} \sim 0$. Both electron-electron and hole-hole exchange interactions exist for $\vec{E} > 0$ whereas only hole-hole exchange interactions exist for $\vec{E} \sim 0$. **g.** Zoomed-in electric field dependence of co- (blue dot) and cross-polarized (red dot) strongest peak energies (left) and their energy splitting (right) at 1 mW.

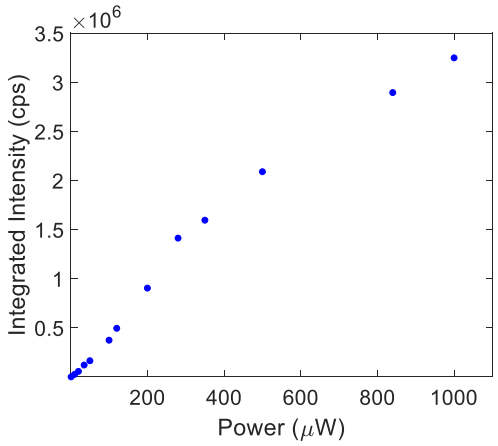

Figure 7.11: Power Dependence of Integrated Intensity of Trilayer Emission. The integrated intensity has a linear dependence on the excitation power up to 1 mW, which implies no saturation induced heating or photo-doping.

7.10a), the electric field dependence of PL energy has the characteristic nonlinear redshift of the hybridized quadrupolar exciton, as discussed above. However, the electric field dependence at a high power of 1 mW exhibits a linear shift, reminiscent of dipolar excitons (Figure 7.10b). To quantitatively visualize the evolution of quadrupolar excitons to dipolar excitons, we extract the slope of the energy shift versus $\vec{E}$, which is proportional to the average dipole moment. Figure 7.10c shows that the slope increases with power and saturates around 1 mW with a maximum slope of $\sim$370 $\pm$ 10 meV/(V/nm), which is comparable to the slope (380 $\pm$ 10 meV/(V/nm)) at low powers in the large $\vec{E}$ limit.

The transition from quadrupolar excitons to dipolar excitons with increased power suggests that the two anti-parallel dipoles become de-hybridized with increased n_{ex}. Further evidence for de-hybridization is provided by blueshift of decoupled top and bottom dipoles with respect to the symmetric quadrupolar excitons, consistent with the hybridization picture of Figure 7.4c. The PL spectra at different powers in Figure 7.10d track the blue-shift of the trilayer excitons from low to high power at a finite $\vec{E}$ (8.4 mV/nm above the turning point). The peak energies are extracted and

plotted in Figure 7.10e, showing a blueshift of $\sim$ 6 meV. As repulsive quadrupolar interactions are weak, the blueshift likely arises from Pauli exclusion owing to the fermionic nature of electron and hole comprising the exciton. Figure 7.10e also shows the modeled blueshift, using a model that accounts for both the Coulomb and exchange interactions, and which we elaborate in the next section.

7.2.2 Modelling the Antiferroelectric State

Having demonstrated an interaction-induced transition from quadrupolar to dipolar excitons at finite $\vec{E}$, we consider the nature of the excitonic phase near $\vec{E} \sim 0$ and high n_{ex}. As expected, the emission blueshifts at $\vec{E} = 0$ as well, as shown in Figure 7.12. When the hybridization is overcome by many-body interactions, the degenerate layer-pseudospin recovers full SU(2) symmetry. Based on a classical electrostatic model, Slobodkin et al. [128] predicts an antiferroelectric staggered phase wherein quadrupolar excitons can reduce their energy by spontaneously breaking layer pseudospin and translation symmetries at sufficiently high densities. However, it is not clear whether quantum fluctuations, which are large in 2D, destroy such long range order. Moreover, the underlying triangular moiré lattice, if present, could frustrate the antiferroelectric state. On the other hand, fluctuating antiferroelectric correlations could develop even in the absence of long range order. Such antiferroelectric correlations will alter the wavefunction of excitons and thereby modify the excitonic exchange interactions, which can be detected through many-exciton exchange-induced valley splitting [20]. As depicted in Figure 7.10f, the reduced overlap of electrons, due to their localization in opposite layers in the antiferroelectric configuration of dipolar excitons, suppresses the exchange interaction compared to parallel dipolar and quadrupolar excitons. Figure 7.10g shows the valley splitting of co- and cross-polarized emission as a function of **E** under circularly polarized excitation, which creates valley-polarized excitons. Indeed, below a small **E** of $\sim$ 4 mV/nm (an energy

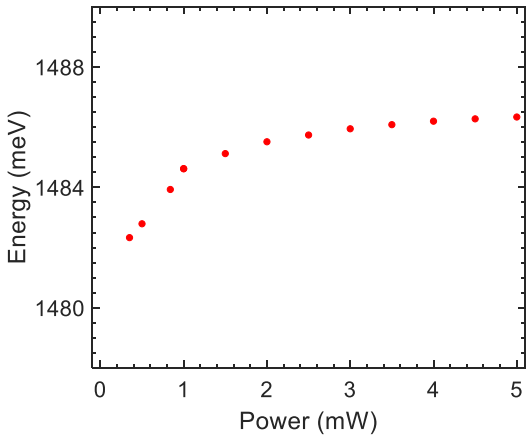

Figure 7.12: Energy Shifts of Quadrupolar Excitons at Higher Power and Zero Electric Field. Data from Sample 3.

scale of $\sim$ 1.5 meV, using the dipole moment at the corresponding power in Figure 7.10c) of either polarity, we observe a reduction in exchange splitting from 2.5 meV to 0.5 meV consistent with an antiferroelectric configuration.

We model the changes in the internal degree of freedom due to the effects of $\vec{E}$ and exciton-exciton interactions using a two-body model including the effect of density-dependent dehybridization. As seen in Figure 7.13, our model predicts antiferroelectric correlations between two excitons for $\vec{E} \sim 0$ and $n_{ex} \sim 10^{12}$ cm^{-2}. The model captures both the blueshift (Figure 7.10e) and the abovementioned increase in linearity of energy shift with electric field reasonably well (see Figure 7.13d,e). Our model agrees with the data for $n_{ex} \sim 10^{12}$cm^{-2} at 1 mW of excitation power.

We develop the quantum two-body model and include many-body effects arising from the fermionic nature of electrons and hole comprising the exciton in accordance by adapting the results of Schmitt-Rink et al. [129] to explain de-hybridization induced transition to dipolar-like behavior with electric field and observed blue shift. Briefly, Pauli exclusion effects causes an excitonic phases-space filling effect and weakening of electron-hole attraction leading to a decrease in binding energy [129, 130]. Considering the exciton as a superposition of electron-hole pairs with momenta ex-

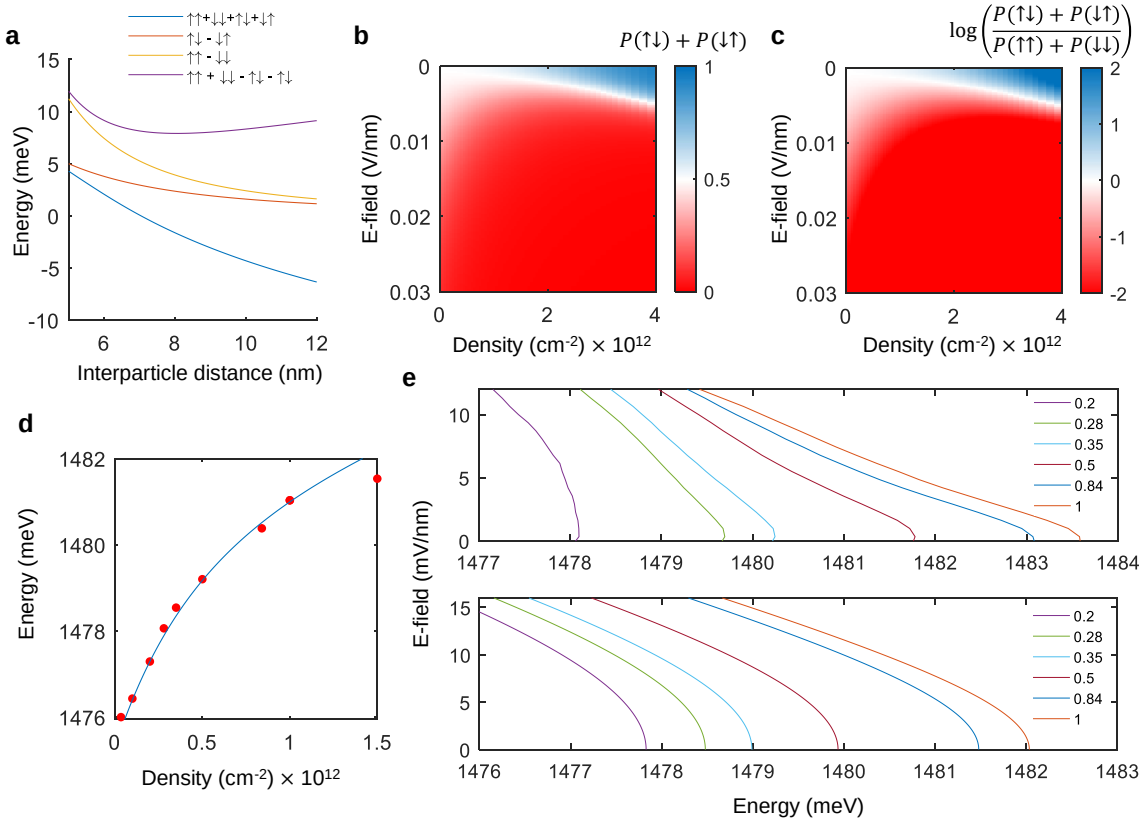

Figure 7.13: Model of Exciton De-hybridization and Antiferroelectric Correlations. **a.** Eigenvalues of the 4-state system of two excitons as a function of their interparticle distance. **b.** 'Phase diagram' of the exciton system under E-field and varying exciton density. The color scale indicates the probability that the excitons are in an antiferroelectric configuration. **c.** Same plot as in panel **(b)**, but with the color bar indicating the logarithm of the ratio of probabilities that the system is found in an antiferroelectric configuration versus an ferroelectric configuration. **d.** Energy of exciton emission at different densities in absence of external electric field. Red points are data and the blue line is the model output. The density of excitons for the data is determined by setting the exciton density at 1 mW of excitation power of 1.696 eV laser to be 10^{12} cm^{-2}, and the other powers use the same conversion factor. **e.** Top panel shows extracted trilayer PL peak positions as a function of E-field at different powers. Legend shows excitation powers of 1.696 eV laser in units of mW. Bottom panel shows the modeled trilayer PL peak positions as a function of E-field at different powers. Legend shows densities in units of 10^{12} cm^{-2}. Both model and data show a faster slope saturation with power.

tending up to inverse of Bohr radius. With higher excitonic densities, the probability that an electron-pair entering this superposition is already occupied keeps increasing, thereby effectively blocking the low momenta states near the band minima. As the hybridization is largest at the K-point and decreases for larger momenta [128], excitons created at high densities experience reduced hybridization due to this phase-space filling effect. Following Schmitt-Rink et al., we assume a density dependent hybridization of the form -

$$t(n) = \frac{t_0}{\left(1 + n/k_0^2\right)^{3/2}},$$

which corresponds to a exponentially decaying tunneling amplitude in real-space with a characteristic length scale of r_0 ($\sim 1/k_0$, where k_0 is the k-space decay scale for hybridization) and the density of exciton $n \sim 1/r^2$, where r is the inter-exciton distance.

Let us express a single trilayer exciton state as the following coherent superposition:

$$|\Psi_X\rangle = \alpha\,|\uparrow\rangle + \beta\,|\downarrow\rangle$$

where $|\uparrow\rangle$ and $|\downarrow\rangle$ correspond to fully polarized dipolar exciton states with opposite dipole moments. Then, a two-exciton state can be expressed as:

$$|\Psi_{XX}\rangle = \alpha\,|\uparrow\uparrow\rangle + \beta\,|\uparrow\downarrow\rangle + \gamma\,|\downarrow\uparrow\rangle + \delta\,|\downarrow\downarrow\rangle = \begin{pmatrix} \alpha \\ \beta \\ \gamma \\ \delta \end{pmatrix}$$

Using this basis, and including an external E-field aligned with the bottom exciton, we can write the Hamiltonian of the two-exciton state when the excitons are at distance r, and have a density-dependent hopping energy t associated with flipping a

dipole:

$$H_0 = \begin{pmatrix} U_{p,p}(n) - 2\vec{d}\cdot\vec{E} & t(n) & t(n) & 0 \\ t(n) & U_{p,-p}(n) & 0 & t(n) \\ t(n) & 0 & U_{p,-p}(n) & t(n) \\ 0 & t(n) & t(n) & U_{p,p}(n) + 2\vec{d}\cdot\vec{E} \end{pmatrix}$$

The effect of Pauli exclusion is also to weaken electron-hole interaction with n which can be thought as a many-body excitonic "screening" [129] and also raises the energy of the system by $\delta E_{ex} \sim E_b a_B^2 n$ leading to the final form of our density-dependent Hamiltonian:

$$H(n) = H_0(n) + \delta E_{ex}(n) I$$

Diagonalizing this Hamiltonian yields four eigenstates, which at $n \to 0$ asymptotically approach the following forms (listed in order of increasing energy):

$$|\Psi_1\rangle = 1/2\,|\uparrow\uparrow\rangle + 1/2\,|\uparrow\downarrow\rangle + 1/2\,|\downarrow\uparrow\rangle + 1/2\,|\downarrow\downarrow\rangle$$

$$|\Psi_2\rangle = 1/\sqrt{2}\,|\uparrow\downarrow\rangle - 1/\sqrt{2}\,|\downarrow\uparrow\rangle$$

$$|\Psi_3\rangle = 1/\sqrt{2}\,|\uparrow\uparrow\rangle - 1/\sqrt{2}\,|\downarrow\downarrow\rangle$$

$$|\Psi_4\rangle = 1/2\,|\uparrow\uparrow\rangle - 1/2\,|\uparrow\downarrow\rangle - 1/2\,|\downarrow\uparrow\rangle + 1/2\,|\downarrow\downarrow\rangle$$

These states can be intuitively understood as follows: $|\Psi_1\rangle$ is the state when both excitons are symmetric quadrupolar excitons; $|\Psi_2\rangle$ is the case when both excitons are dipolar and anti-aligned; $|\Psi_3\rangle$ is the case when both excitons are dipolar and aligned; finally, $|\Psi_4\rangle$ is the state when both excitons are antisymmetric quadrupolar excitons. In the $n \to 0$ limit, $|\Psi_2\rangle$ and $|\Psi_3\rangle$ become degenerate as the interactions vanish and t_0 is the only remaining energy scale (Figure 7.13a). For finite n (as well as $\vec{E}$), these states change their character. At $n \to \infty$, the states $|\Psi_1\rangle$ and $|\Psi_2\rangle$ become degenerate,

both having become the classical anti-aligned dipolar superposition, since $t(\infty) \to 0$. Similarly, $|\Psi_3\rangle$ and $|\Psi_4\rangle$ merge at $n \to \infty$ into a single branch that corresponds to the classical aligned dipolar state. Therefore, our model captures the expected limiting cases, where the ground state at low densities is the quadrupolar exciton, and the ground state at very high densities is an anti-aligned dipolar configuration.

Using $r_0 \sim 3$ nm (corresponding to a $k_0 \sim$ one-tenth of the Brillouin zone), $t = 8.5$ meV and $n \sim 10^{12}$ cm^{-2} at excitation power of 1 mW, we obtain the energy of the ground state as a function of density which reasonably matches our observed blueshift at $\vec{E} = 0$ (Figure 7.13d). The model also allows us to examine how the weights of the antiparallel components of the ground state $|\Psi_1\rangle$ (i.e. $|\beta|^2 + |\gamma|^2$) evolve as a function of density and out-of-plane electric field, as compared to the parallel components ($|\alpha|^2$ and $|\delta|^2$) (Figure 7.13b,c). This rough 'phase diagram' shows that at low densities ($n_{ex} < 10^{11}$ cm^{-2}), the quadrupolar excitons (characterized by a roughly equal superposition of antiparallel and parallel components) are robust against polarization, requiring E = 30 mV/nm to reach near-polarization ($|\alpha|^2 \geq 0.9$), which is comparable to the $\sim$ 30 mV/nm at which the PL slope saturates in our data. When $n_{ex} \sim$ 1-2 $\times$ 10^{12} cm^{-2}, the hybridization strength t decreases and the quadrupolar exciton becomes easier to saturate, with the required E-field to reach $|\alpha|^2 \geq 0.9$ falling to E = 7-10 mV/nm. At the same time, the antiferroelectric correlation increases (Figure 7.13b,c), reaching a normalized difference between antiferroelectric and ferroelectric configurations, $(|\beta|^2 + |\gamma|^2) - (|\alpha|^2 + |\delta|^2)$, of $\sim 33\%$ at $n_{ex} \sim 2\times$ 10^{12} cm^{-2}. Therefore, the model captures the experimental result of the decrease in the E-field needed to saturate the dipole moment at higher densities (Figure 7.13e) and predicts increased antiferroelectric correlations at high excitation powers. We note that the antiferroelectric configuration is favored by 'intralayer' kinetic energy (ignored in our model) wherein a simultaneous exchange of electrons will cause fluctuations of the antiferroelectric configuration, thus, reducing the threshold of n_{ex} needed to observe

antiferroelectric correlations even further.

7.3 Conclusion

In conclusion, we have demonstrated the observation of an unconventional exciton formed as symmetric coherent superposition of oppositely oriented dipolar excitons in a vdW heterotrilayer and featuring an out-of-plane quadrupolar moment. An external electric field can modify the wavefunction of the quadrupolar exciton wavefunction and change its dipole moment to achieve tunable light-matter interactions. For example, the sizable oscillator strength of symmetric quadrupolar excitons allows for efficient coupling to optical cavity modes and the resulting quadrupolar polaritons can be used for electrically tunable light-matter coupling and polariton-polariton interactions [131, 132, 133]. In addition, trilayers with additional electrical degrees of freedom could utilize the antiferroelectric correlatiosn demonstrated here for unconventional capacitors with diverging differential capcicatene near aa critical poitn where the antiferroelectric correlations start [134].

Chapter 8

Summary and Outlook

In this thesis, we focused on novel excitonic phases in van der Waals (vdW) semiconductor transition metal dichalcogenides (TMDs). TMDs provide an excellent platform for studying novel excitonic species and ways in which they can spontaneously arrange – the confinement to the 2D plane leads to strong interactions; the indirect nature of the excitons gives them long lifetimes; and the twist-angle, number of layers, external gating and choice of materials are all interesting degrees of freedom enabling a rich phase space to explore. The remarkable optical properties of the TMD monolayer allow for efficient generation of high excitonic densities and analysis of their physics by measuring the absorption and photoluminescence emission spectra, enabling us to learn much about the internal structure and interactions of the excitons spectroscopically. Interlayer excitons in TMD heterostructures can be studied in solid-state regimes with length scales smaller than those in cold atoms systems, and in the context of a tunable moiré potential, enabling the search for new physics.

Our work focused on the search for novel excitonic phases in these systems. Firstly, we showed a realization of the Bose-Hubbard model and the excitonic Mott insulator it predicts in TMD heterobilayers in the form of the excitonic Mott insulator. We extend this result by also investigating a mixed exciton-electron Mott insulating

phase, realizes field-tunable lattices of excitonic emitters embedded in a electronic Wigner crystal. Secondly, we showed evidence for spontaneous symmetry breaking, in-plane ferroelectric phase near the Mott insulating state arising from strong cross-site interactions between moiré excitons, and their signatures in the decay dynamics of the excitons. Lastly, we observed a novel out-of-plane quadrupolar exciton in TMD trilayers, and observed signatures of Coulomb and exchange interaction-driven antiferroelectric correlations.

However, our work leaves many questions unresolved as well as suggests exciting future opportunities. We will expand on a few of these which are relevant in the context of this thesis:

In the case of the excitonic and mixed Mott insulator, there is still the open matter of what the excitonic states look like when embedded in an electronic Wigner crystal. We find evidence of reduced polaron formation via the PL blueshift and enhancement at fractionally-filled states, but their effect of the interlayer excitons are an open question, as we have just begun to understand the intercell complexes that form in these systems, with models in active development [135]. One interesting direction future work might take is investigating the diffusion and valley-relaxation dynamics of the excitons in these states, since recent work suggests exciton diffusivity can actually be enhanced at highly electron doped states [112, 113].

Since the excitonic sites in such systems are defined as the negative lattice to the electron crystal, the capacity to embed optically active sites in a well-defined geometry suggests the possibility of tuning the nature of the coupling between those sites. If these sites were made to couple strongly via the electromagnetic vacuum, the fact that they are separated by distances much less than the wavelength of the emitted light suggest the possibility of collective optical effects such as super- or sub-radiance [115, 136]. Such strong coupling is not observed in our system, as the IX lifetimes are long, but the coupling could be enhanced by use of cavities or by relying

on the much shorter-lived intra-layer excitons in a moiré potential, such as in Type-I heterostructures [58] or by the recently developed technique of using twisted hBN to impart a moiré pattern on a monolayer [137].

While the effects that electrons can impart on the excitons are important, one can put the problem on its head by asking how the excitons in turn affect the itinerant electrons. An exciting recent prediction is the capacity of circularly polarized excitation light imparting a ferromagnetic order to itinerant electrons in H-stacked WS_2/WSe_2 heterostructures [138]. Therefore, our platform may allow for optically induced magnetism in the generalized Wigner crystals.

Regarding our work on the in-plane excitonic ferroelectric, the most obvious continuation is to fully characterize and confirm that the system indeed undergoes a *bona-fide* phase transition by measuring the hysteresis under in-plane electric field that a ferroelectric state is expected to have. The application of substantial, uniform in-plane fields to the sample presents technical challenges in sample fabrication due to the geometry, but these are not insurmountable. As our observations are limited to establishing local ferroelectric correlations, it would be interesting to observe what kinds of long-range order and ferroelectric domains can be formed in our system, and what the dynamics of higher order excitations of the systems such as domain walls might look like, which could be addressed via microwave spectroscopy.

Another exciting direction is the possibility of imparting the moiré pattern of the heterostructure hosting the ferroelectric state onto a nearby monolayer. Since the charge carriers in the excitonic ferroelectric state are separated in-plane under optical pumping, a nearby layer with a monolayer hBN spacer, which typically entirely suppresses the moiré pattern [139], might be overcome when the carriers are optically separated, as the mechanism of the moiré potential would be strictly electrostatic, as opposed to relying on direct-contact charge transfer.

The three-way degeneracy of the dipole in the H-stacked sample is also reminis-

cent of the $q = 3$ 2D quantum Potts model [140], but in the electric (rather than magnetic) dipole realization. The phase space of such models is still not entirely understood, and the studied system could prove a convenient experimental realization. Moreover, we have not touched on the magnetic regime of the excitons in our study. If the ferroelectric state is pumped by circularly polarized light, we may also realize a multiferroic state, as the excitons would be polarized both in the electric dipole and valley degree of freedom.

Similarly to the in-plane ferroelectric, the out-of-plane antiferroelectric state that we observe at high densities in trilayers, and the dynamics of the transition into the state, are still not fully clear. The presence of long-range antiferroelectric order is difficult to establish, especially with such a local order parameter, and may require the use of scanning-probe techniques. Another approach would be to focus on the electronic sector, where such antiferroelectric states are predicted to lead to a divergent differential capacitance of the system [134]. The challenge in such an approach is the fabrication of the trilayer with hBN spacers needed to suppress tunneling currents in the system, as well as the formation of Ohmic contacts of sufficient quality to each layer.

Also, the nature of the moiré potential in trilayers is still an open question, as the phase space increases significantly with the presence of two twist angles. While some work has been done to understand this 'moiré of moiré' [127, 141], the current consensus is that such samples are very sensitive to strain and twist angle variations, and it is not clear whether out-of-plane quadrupolar excitons can be formed in systems with strong moiré potentials such that they exhibit strong confinement, such as in heterobilayers.

It is my sincere hope that these exciting systems continue to yield insight into new areas of condensed matter physics.

Appendix A

Transfer Matrix Determination of Optimal hBN Thickness

We use the open source tmm package [142] to calculate the absorption of a TMD layer encapsulated by hBN flakes of varying thicknesses, on a 300 nm SiO_2/Si substrate. Refractive index reference files obtained from 'www.refractiveindex.info'.

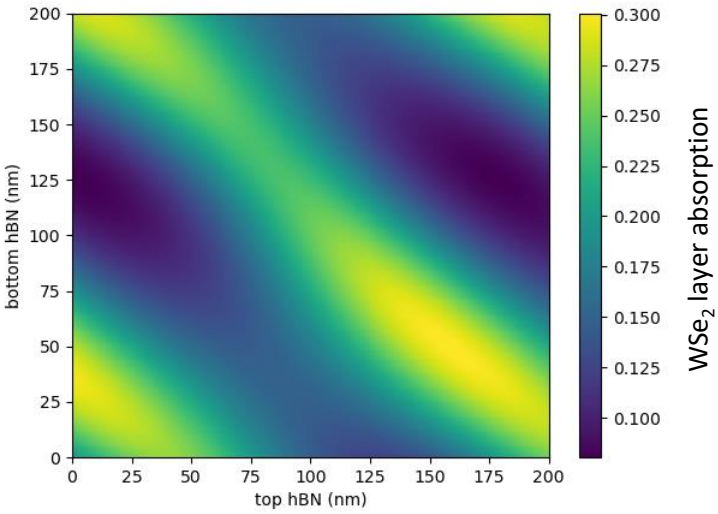

Figure A.1: Ray-Transfer-Matrix Calculation of hBN-encapsulated WSe_2 Absorption. The strong absorption near 30 nm thickness for both layers offers a good balance between sufficient electrical insulation and strong absorption.

Appendix B

Monte-Carlo Simulation of Dipolar and Quadrupolar Exciton Decay Dynamics

The Monte-Carlo simulations of excitonic dynamics featured in this chapter were developed by our collaborators Dr. Jan Kumlin and Professor Thomas Pohl of TU Wien, who also provided the write-up in this appendix.

The emission lifetime and emission spectra simulations were performed using a Monte Carlo sampling and quantum jump approach on a triangular lattice with 30×30 sites under periodic boundary conditions. Excitons were treated as dipolar particles occupying distinct lattice sites, initialized in one of three possible hole configurations. For filling fractions below $\nu = 1/3$, we avoid the occupation of nearest-neighbor sites due to the dipolar repulsion and the fact that there is no slowdown in the decay measured below these filling fractions. Emission rates were determined by local exciton densities, with recombination probabilities calculated dynamically. For example, excitons with no occupied neighboring sites decayed with a rate of $\gamma_{\mathrm{Q}} = 6.3\,\mathrm{MHz}$ (lifetime $\tau_{\mathrm{Q}} = 160\,\mathrm{ns}$), while those with fully occupied neighboring

sites had a reduced rate $\gamma_{\mathrm{d}} = \gamma_{\mathrm{Q}}/3 = 2.1\,\mathrm{MHz}$ (lifetime $\tau_{\mathrm{d}} = 480\,\mathrm{ns}$), matching experimentally obtained high- and low-density lifetimes. Intermediate rates were assigned proportionally based on available hole states. The evolution followed a Lindblad master equation with dissipative recombination dynamics simulated through stochastic quantum jumps. Emission spectra were obtained by tracking energy shifts during the exciton decay, incorporating only nearest-neighbor Coulomb interactions. Quantitative agreement with the experimental data is obtained by reducing the in-plane distance of electrons and holes by a factor of 0.7 compared to their single-particle potential minima.

Model: We model the experimental system by considering a triangular lattice with N lattice sites occupied by M excitons. Due to the strong on-site interaction $\mathrm{U_{XX}}$, each lattice site can be occupied by at most one exciton. On each occupied moiré lattice site, for a fixed position of the electron, the hole can be in three different configurations 1, 2, or 3, as shown in Fig. 4a in the main text. We describe the creation of such an exciton at a position $\mathbf{r}_i$ on the lattice by the operator $c^\dagger_{e,i} c^\dagger_{h_\alpha,i}$, where $c^\dagger_{e,i}$ describes the creation of an electron at position $\mathbf{r}_i$ and $c^\dagger_{h_\alpha,i}$ with $\alpha \in \{1,2,3\}$ describes the creation of the corresponding hole in configuration α. Note that all three hole configurations have the same energy.

If two neighbouring lattice sites are occupied by excitons, certain hole configurations are energetically blue-shifted due to the large overlap of the respective hole wavefunctions and the associated large (repulsive) Coulomb energy, $\mathrm{U_{hh}}$.

We describe the system by the Hamiltonian

$$H = \sum_{\langle i,j \rangle} \sum_{\alpha,\beta \in 1,2,3} V_{ij}^{\alpha\beta} c^\dagger_{h_\alpha,i} c^\dagger_{h_\beta,j} c_{h_\beta,j} c_{h_\alpha,i}\,, \tag{B.1}$$

where the first sum runs over nearest neighbours and $V_{ij}^{\alpha\beta}$ denotes the interaction energy between hole configuration α on site i and hole configuration β on site j. As

this interaction energy is the largest scale in our problem, we take it to be infinite whenever the hole wavefunctions overlap for two configurations α and β and zero if not.

In the following, we restrict our analysis to the subspace of eigenstates of zero energy with respect to this Hamiltonian. These eigenstates can, for a given number M of excitons, be charazterized by a spatial configuration $\mathbf{R}_M = \{\mathbf{r}_1, \cdots, \mathbf{r}_M\}$ of the position of the excitons, as well as a hole configuration $\boldsymbol{\alpha} = \{\alpha_1, \cdots \alpha_M\}$ which has zero energy with respect to the Hamiltonian (B.1). The states are then given by

$$|\varphi_{\mathbf{R}_M,\boldsymbol{\alpha}}\rangle = \prod_{i=1}^{M} c_{e,i}^{\dagger} c_{h_\alpha,i}^{\dagger} |\emptyset\rangle \equiv |\alpha_1, \ldots, \alpha_M\rangle \ , \tag{B.2}$$

where $|\emptyset\rangle$ is the vacuum state with no excitons present.

For a fixed spatial configuration $\mathbf{R}_M$, we take the state

$$|\Psi_{\mathbf{R}_M}\rangle = \frac{1}{\sqrt{\mathcal{N}_{\mathbf{R}_M}}} \sum_{\boldsymbol{\alpha}} |\varphi_{\mathbf{R}_M,\boldsymbol{\alpha}}\rangle \tag{B.3}$$

to be the strongly correlated many-body state of the electron-hole system. Here, $\mathcal{N}_{\mathbf{R}_M}$ is a normalization constant and the sum runs over all hole configurations with zero interaction energy. Note that the hole delocalization will give rise to a collective decay rate which can be up to three times γ_d.

In order to do so, we note that, while the sum over hole configurations is coherent, different spatial configurations of excitons do not share any coherence and we write the full many-body density matrix for M excitons as

$$\rho^{(M)} = \sum_{\mathbf{R}_M} |\Psi_{\mathbf{R}_M}\rangle \langle \Psi_{\mathbf{R}_M}| \ . \tag{B.4}$$

The dissipative dynamics of the system is given by the Lindbladian master equation

$$\partial_t \rho = \gamma_d \sum_i \left(\sigma_i^- \rho \sigma_i^+ - \frac{1}{2} \left\{ \sigma_i^+ \sigma_i^-, \rho \right\} \right), \tag{B.5}$$

where ρ is the many-body density matrix of the exciton system and $\sigma_i^- = \sum_\alpha c_{h_\alpha,i} c_{e,i}$ describes local photon emission due to electron-hole recombination. Note that while the decay described by Eq. (B.5) is completely local, the delocalization of holes on a single site opens up the possibility of an enhancement of the emission rate if the hole is fully or partially delocalized.

Since the dynamics is completely incoherent, we can decompose the many-body density matrix ρ into different sectors labeled by the exciton number as

$$\rho = \bigoplus_{M=0}^{N} \rho^{(M)} . \tag{B.6}$$

Monte-Carlo Simulations: In order to simulate the dissipative dynamics of the complicated many-body system, we use a combination of Monte-Carlo sampling to approximate the states Eq. (B.3) and the quantum jump formalism, which will be outlined in the following.

As there is no coherent evolution in the master equation (B.5), we can describe our system by a series of exciton emission processes at some random times t_j. At any time t between these emission processes, the system has a fixed number of excitons and we assume that the state of the system is described by the density matrix Eq. (B.4).

Since our Lindblad master equation does not contain any coherent evolution, we can use a simple scheme to calculate the jump times t_j and the overall dynamics. To this end, assume we are at some time t in a state $|\Psi_{\mathbf{R}_M}(t)\rangle$. For this state, we calculate the emission rate γ_i for a given site i by

$$\gamma_i = \gamma_d \left\langle \Psi_{\mathbf{R}_M}(t) \right| \sigma_i^+ \sigma_i^- \left| \Psi_{\mathbf{R}_M}(t) \right\rangle = \frac{\gamma_d}{\mathcal{N}_{\mathbf{R}_M}} \sum_{\boldsymbol{\alpha}} \sum_{\boldsymbol{\beta}} \prod_{j \neq i} \langle \alpha_j | \beta_j \rangle \left\langle \alpha_i \right| \sigma_i^+ \sigma_i^- \left| \beta_i \right\rangle$$
$$= \frac{\gamma_d}{\mathcal{N}_{\mathbf{R}_M}} \sum_{\boldsymbol{\alpha}} \sum_{\beta_i} \left\langle \alpha_i \right| \sigma_i^+ \sigma_i^- \left| \beta_i \right\rangle$$
$$= \frac{\gamma_d}{\mathcal{N}_{\mathbf{R}_M}} \sum_{\boldsymbol{\alpha}'} \sum_{\alpha_i} \eta(\boldsymbol{\alpha}', \alpha_i) \,, \tag{B.7}$$

where $\boldsymbol{\alpha}' = \boldsymbol{\alpha} \backslash \{\alpha_i\}$ and $\eta(\boldsymbol{\alpha}, \alpha_i)$ is unity if the local configuration α_i is allowed given the global configuration $\boldsymbol{\alpha}'$ without including site i. Thus, the second sum can either take the value 3, 2, or 1, depending on the neighboring sites.

Given the local emission rates, we can calculate the total emission rate

$$\Gamma = \sum_i \gamma_i \,, \tag{B.8}$$

where the sum runs only over the occupied sites (alternatively, we can weigh every term by its electron occupation). The total emission rate Γ determines the jump time $t_j = t + t^*$ when one of the excitons recombines with

$$t^* = -\frac{\ln r}{\Gamma} \,, \tag{B.9}$$

with $0 \leq r \leq 1$ being a random number. The exciton which recombines is determined according to the probability distribution given by

$$p_i = \frac{\gamma_i}{\Gamma} \,. \tag{B.10}$$

After the exciton recombination, we assume that the hole delocalization process is very fast such that the new state of the system is again well described by the state $\left| \Psi_{\mathbf{R}'_{M-1}}(t + t^*) \right\rangle$ and Eq. (B.4), with the new spatial configuration $\mathbf{R}'_{M-1}$, where the

exciton that has decayed is removed.

The whole simulation procedure can then be summarised by the following steps:

(1) Given a number of excitons M, randomly chose an initial configuration $\mathbf{R}_M$. Below a filling fraction of 1/3, we use an additional nearest-neighbour exclusion for the excitons to take into account the effect of the static dipole-dipole interactions. This is also motivated by the fact that the emission dynamics does not change for low filling fractions.

(2a) Initialize all holes in the same, but randomly chosen, configuration, that is $\alpha_i = \alpha$, with $\alpha \in \{1, 2, 3\}$.

(2b) Scramble the hole configurations by randomly selecting one of the occupied sites and bring the hole into another allowed configuration. Repeat this step a sufficient number of times to generate one of the states in Eq. (B.2). This concludes the initialization step.

(3) Calculate the emission rate, jump time, and chose the exciton that decays according to Eqs. (B.8), (B.9), and (B.10), respectively.

(4) Repeat step (3) for the new spatial configuration $\mathbf{R}'_{M-1}$ with one exciton less until no more excitons are present.

(5) Repeat steps (1)-(4) for many randomly chosen initial spatial configurations and average over the different trajectories.

For the simulations, we use a triangular lattice with $N = 30 \times 30$ sites with periodic boundary conditions and chose the initial number of excitons M according to the filling factor $\nu = M/N$.

Calculation of emission energy: In order to calculate the emission spectrum using the formalism above, we calculate the electrostatic energy difference ΔE of the hole configuration $\boldsymbol{\alpha}$ immediately before the jump and the configuration $\boldsymbol{\alpha}'$ right

after the jump (where, say, the exciton at position $\mathbf{r}_i$ has been removed). The energy difference is then simply given by the interaction energy of that site i in the current configuration with its surrounding. Due to the fast decay ($\sim 1/r^3$) of Coulomb interaction, we take only the nearest-neighbouring sites into account, such that the energy difference for a given hole configuration $\boldsymbol{\alpha}$ is given by

$$\Delta E^{(\boldsymbol{\alpha})} = -\frac{e^2}{4\pi\varepsilon_0\varepsilon_r}\sum_j \left\{ \frac{1}{|\mathbf{r}_i - \mathbf{r}_j|} + \frac{1}{\left|\left(\mathbf{r}_i + \mathbf{r}_{\alpha_i}^{(h)}\right) - \left(\mathbf{r}_j + \mathbf{r}_{\alpha_j}^{(h)}\right)\right|} - \frac{1}{\left|\mathbf{r}_i - \left(\mathbf{r}_j + \mathbf{r}_{\alpha_j}^{(h)}\right)\right|} - \frac{1}{\left|\left(\mathbf{r}_i + \mathbf{r}_{\alpha_i}^{(h)}\right) - \mathbf{r}_j\right|} \right\}, \tag{B.11}$$

where the sum runs over all occupied nearest-neighbour sites of site i, $\mathbf{r}_i$ denote the electron position, and $\mathbf{r}_{\alpha_i}^{(h)}$ denote the hole position relative to the electron position given a hole configuration α_i.

Similar to the calculations of the emission rate, we obtain a sequence of emission energies $\Delta E(t_j)$. In the limit of $N_{\text{traj}} \to \infty$, we would get a distribution $p(\Delta E)$ at every time t. To account for the finite number of trajectories, we bin different times to approximate this distribution and calculate the spectra shown in Fig. 4d, e in the main text. We made sure that the binning process does not affect the emission spectrum.

Appendix C

DFT Calculations of Trilayer Wavefunctions

The DFT calculations were performed by our collaborators, Dr. Jin Zhang and Professor Angel Rubio of the Max Plank Institute, who also provided the write-up in this appendix. The ab initio calculations were performed within the Vienna Ab initio Simulation Package (VASP)[143] using a projector-augmented wave (PAW) pseudopotential in conjunction with the Perdew–Burke–Ernzerhof (PBE)[144] functionals and a plane-wave basis set with an energy cutoff at 400 eV. The unit cells are chosen to consist $WS_2/WSe_2/WS_2$ trilayers with a lattice constant of 3.154 Å and interlayer spacing of 5.9 Å or 6.2 Å. A vacuum region of 20 Å is applied to avoid artificial interaction between the periodic images along the vertical direction. The first Brillouin zone of the heterostructure was sampled using a 15×15×1 k-point grids. The structures at ground states were fully relaxed until the force on each atom was < 0.01 eV Å^{-1}. The van der Waals interactions were included using the opt88 functional [145]. For the structures with modified interlayer hybridizations, the interlayer distances were artificially modulated to get insight into the influence various stackings. Spin-orbital couplings are included in the calculations of electronic structures.

Bibliography

[1] Nathan P Wilson, Wang Yao, Jie Shan, and Xiaodong Xu. Excitons and emergent quantum phenomena in stacked 2d semiconductors. *Nature*, 599(7885):383–392, 2021.

[2] John R Schaibley, Hongyi Yu, Genevieve Clark, Pasqual Rivera, Jason S Ross, Kyle L Seyler, Wang Yao, and Xiaodong Xu. Valleytronics in 2d materials. *Nature Reviews Materials*, 1(11):1–15, 2016.

[3] Haifeng Kang, Jingwen Ma, Junyu Li, Xiang Zhang, and Xiaoze Liu. Exciton polaritons in emergent two-dimensional semiconductors. *ACS nano*, 17(24):24449–24467, 2023.

[4] Jinwoong Hwang, Wei Ruan, Yi Chen, Shujie Tang, Michael F Crommie, Zhi-Xun Shen, and Sung-Kwan Mo. Charge density waves in two-dimensional transition metal dichalcogenides. *Reports on Progress in Physics*, 87(4):044502, 2024.

[5] Dong Qiu, Chuanhui Gong, SiShuang Wang, Miao Zhang, Chao Yang, Xianfu Wang, and Jie Xiong. Recent advances in 2d superconductors. *Advanced Materials*, 33(18):2006124, 2021.

[6] Yuqiang Fang, Jie Pan, Dongqin Zhang, Dong Wang, Hishiro T Hirose, Taichi Terashima, Shinya Uji, Yonghao Yuan, Wei Li, Zhen Tian, et al. Discovery of

superconductivity in 2m ws2 with possible topological surface states. *Advanced Materials*, 31(30):1901942, 2019.

[7] Yuan Cao, Valla Fatemi, Shiang Fang, Kenji Watanabe, Takashi Taniguchi, Efthimios Kaxiras, and Pablo Jarillo-Herrero. Unconventional superconductivity in magic-angle graphene superlattices. *Nature*, 556(7699):43–50, 2018.

[8] Lei Wang, En-Min Shih, Augusto Ghiotto, Lede Xian, Daniel A Rhodes, Cheng Tan, Martin Claassen, Dante M Kennes, Yusong Bai, Bumho Kim, et al. Correlated electronic phases in twisted bilayer transition metal dichalcogenides. *Nature materials*, 19(8):861–866, 2020.

[9] Jiaqi Cai, Eric Anderson, Chong Wang, Xiaowei Zhang, Xiaoyu Liu, William Holtzmann, Yinong Zhang, Fengren Fan, Takashi Taniguchi, Kenji Watanabe, et al. Signatures of fractional quantum anomalous hall states in twisted mote2. *Nature*, 622(7981):63–68, 2023.

[10] Heonjoon Park, Jiaqi Cai, Eric Anderson, Yinong Zhang, Jiayi Zhu, Xiaoyu Liu, Chong Wang, William Holtzmann, Chaowei Hu, Zhaoyu Liu, et al. Observation of fractionally quantized anomalous hall effect. *Nature*, 622(7981):74–79, 2023.

[11] Yihang Zeng, Zhengchao Xia, Kaifei Kang, Jiacheng Zhu, Patrick Knüppel, Chirag Vaswani, Kenji Watanabe, Takashi Taniguchi, Kin Fai Mak, and Jie Shan. Thermodynamic evidence of fractional chern insulator in moiré mote2. *Nature*, 622(7981):69–73, 2023.

[12] Patrick A Lee, Naoto Nagaosa, and Xiao-Gang Wen. Doping a mott insulator: Physics of high-temperature superconductivity. *Reviews of modern physics*, 78(1):17–85, 2006.

[13] Yang Xu, Song Liu, Daniel A Rhodes, Kenji Watanabe, Takashi Taniguchi, James Hone, Veit Elser, Kin Fai Mak, and Jie Shan. Correlated insulating

states at fractional fillings of moiré superlattices. *Nature*, 587(7833):214–218, 2020.

[14] Emma C Regan, Danqing Wang, Chenhao Jin, M Iqbal Bakti Utama, Beini Gao, Xin Wei, Sihan Zhao, Wenyu Zhao, Zuocheng Zhang, Kentaro Yumigeta, et al. Mott and generalized wigner crystal states in wse2/ws2 moiré superlattices. *Nature*, 579(7799):359–363, 2020.

[15] Yanhao Tang, Lizhong Li, Tingxin Li, Yang Xu, Song Liu, Katayun Barmak, Kenji Watanabe, Takashi Taniguchi, Allan H MacDonald, Jie Shan, et al. Simulation of hubbard model physics in wse2/ws2 moiré superlattices. *Nature*, 579(7799):353–358, 2020.

[16] Yuya Shimazaki, Ido Schwartz, Kenji Watanabe, Takashi Taniguchi, Martin Kroner, and Ataç Imamoğlu. Strongly correlated electrons and hybrid excitons in a moiré heterostructure. *Nature*, 580(7804):472–477, 2020.

[17] Tomasz Smoleński, Pavel E Dolgirev, Clemens Kuhlenkamp, Alexander Popert, Yuya Shimazaki, Patrick Back, Xiaobo Lu, Martin Kroner, Kenji Watanabe, Takashi Taniguchi, et al. Signatures of wigner crystal of electrons in a monolayer semiconductor. *Nature*, 595(7865):53–57, 2021.

[18] You Zhou, Jiho Sung, Elise Brutschea, Ilya Esterlis, Yao Wang, Giovanni Scuri, Ryan J Gelly, Hoseok Heo, Takashi Taniguchi, Kenji Watanabe, et al. Bilayer wigner crystals in a transition metal dichalcogenide heterostructure. *Nature*, 595(7865):48–52, 2021.

[19] Pasqual Rivera, Kyle L Seyler, Hongyi Yu, John R Schaibley, Jiaqiang Yan, David G Mandrus, Wang Yao, and Xiaodong Xu. Valley-polarized exciton dynamics in a 2d semiconductor heterostructure. *Science*, 351(6274):688–691, 2016.

[20] Weijie Li, Xin Lu, Jiatian Wu, and Ajit Srivastava. Optical control of the valley zeeman effect through many-exciton interactions. *Nature Nanotechnology*, 16(2):148–152, 2021.

[21] Malte Kremser, Mauro Brotons-Gisbert, Johannes Knörzer, Janine Gückelhorn, Moritz Meyer, Matteo Barbone, Andreas V Stier, Brian D Gerardot, Kai Müller, and Jonathan J Finley. Discrete interactions between a few interlayer excitons trapped at a mose2–wse2 heterointerface. *npj 2D Materials and Applications*, 4(1):8, 2020.

[22] Zhe Sun, Alberto Ciarrocchi, Fedele Tagarelli, Juan Francisco Gonzalez Marin, Kenji Watanabe, Takashi Taniguchi, and Andras Kis. Excitonic transport driven by repulsive dipolar interaction in a van der waals heterostructure. *Nature photonics*, 16(1):79–85, 2022.

[23] Roscoe G Dickinson and Linus Pauling. The crystal structure of molybdenite. *Journal of the American Chemical Society*, 45(6):1466–1471, 1923.

[24] Kostya S Novoselov, Da Jiang, F Schedin, TJ Booth, VV Khotkevich, SV Morozov, and Andre K Geim. Two-dimensional atomic crystals. *Proceedings of the National Academy of Sciences*, 102(30):10451–10453, 2005.

[25] Li F Mattheiss. Band structures of transition-metal-dichalcogenide layer compounds. *Physical Review B*, 8(8):3719, 1973.

[26] Marco Bernardi, Can Ataca, Maurizia Palummo, and Jeffrey C Grossman. Optical and electronic properties of two-dimensional layered materials. *Nanophotonics*, 6(2):479–493, 2017.

[27] Sajedeh Manzeli, Dmitry Ovchinnikov, Diego Pasquier, Oleg V Yazyev, and Andras Kis. 2d transition metal dichalcogenides. *Nature Reviews Materials*, 2(8):1–15, 2017.

[28] Brian SY Kim, Tien Dat Ngo, Yasir Hassan, Sang Hoon Chae, Soon-Gil Yoon, and Min Sup Choi. Advances and applications of oxidized van der waals transition metal dichalcogenides. *Advanced Science*, 11(43):2407175, 2024.

[29] Can Ataca, Hasan Sahin, and Salim Ciraci. Stable, single-layer mx2 transition-metal oxides and dichalcogenides in a honeycomb-like structure. *The Journal of Physical Chemistry C*, 116(16):8983–8999, 2012.

[30] Carmem M Gilardoni, Freddie Hendriks, Caspar H van der Wal, and Marcos HD Guimarães. Symmetry and control of spin-scattering processes in two-dimensional transition metal dichalcogenides. *Physical Review B*, 103(11):115410, 2021.

[31] Chao-Xing Liu. Unconventional superconductivity in bilayer transition metal dichalcogenides. *Physical review letters*, 118(8):087001, 2017.

[32] Robert O Jones. Density functional theory: Its origins, rise to prominence, and future. *Reviews of modern physics*, 87(3):897–923, 2015.

[33] Woojoo Lee, Yi Lin, Li-Syuan Lu, Wei-Chen Chueh, Mengke Liu, Xiaoqin Li, Wen-Hao Chang, Robert A Kaindl, and Chih-Kang Shih. Time-resolved arpes determination of a quasi-particle band gap and hot electron dynamics in monolayer mos2. *Nano letters*, 21(17):7363–7370, 2021.

[34] AC Dias, Fanyao Qu, David L Azevedo, and Jiyong Fu. Band structure of monolayer transition-metal dichalcogenides and topological properties of their nanoribbons: Next-nearest-neighbor hopping. *Physical Review B*, 98(7):075202, 2018.

[35] Di Xiao, Ming-Che Chang, and Qian Niu. Berry phase effects on electronic properties. *Reviews of modern physics*, 82(3):1959–2007, 2010.

[36] Ming-Che Chang and Qian Niu. Berry curvature, orbital moment, and effective quantum theory of electrons in electromagnetic fields. *Journal of Physics: Condensed Matter*, 20(19):193202, 2008.

[37] Takahiro Fukui, Yasuhiro Hatsugai, and Hiroshi Suzuki. Chern numbers in discretized brillouin zone: efficient method of computing (spin) hall conductances. *Journal of the Physical Society of Japan*, 74(6):1674–1677, 2005.

[38] Ming-Che Chang and Qian Niu. Berry phase, hyperorbits, and the hofstadter spectrum. *Physical review letters*, 75(7):1348, 1995.

[39] Di Xiao, Wang Yao, and Qian Niu. Valley-contrasting physics in graphene: magnetic moment and topological transport. *Physical review letters*, 99(23):236809, 2007.

[40] Di Xiao, Gui-Bin Liu, Wanxiang Feng, Xiaodong Xu, and Wang Yao. Coupled spin and valley physics in monolayers of mos 2 and other group-vi dichalcogenides. *Physical review letters*, 108(19):196802, 2012.

[41] Kin Fai Mak, Kathryn L McGill, Jiwoong Park, and Paul L McEuen. The valley hall effect in mos2 transistors. *Science*, 344(6191):1489–1492, 2014.

[42] Kyung-Han Kim and Hyun-Woo Lee. Berry curvature in monolayer mos 2 with broken mirror symmetry. *Physical Review B*, 97(23):235423, 2018.

[43] Andor Kormányos, Viktor Zólyomi, Neil D Drummond, Péter Rakyta, Guido Burkard, and Vladimir I Fal'Ko. Monolayer mos 2: Trigonal warping, the γ valley, and spin-orbit coupling effects. *Physical Review B—Condensed Matter and Materials Physics*, 88(4):045416, 2013.

[44] Wang Yao, Di Xiao, and Qian Niu. Valley-dependent optoelectronics from inver-

sion symmetry breaking. *Physical Review B—Condensed Matter and Materials Physics*, 77(23):235406, 2008.

[45] Grant Aivazian, Zhirui Gong, Aaron M Jones, Rui-Lin Chu, Jiaqiang Yan, David G Mandrus, Chuanwei Zhang, David Cobden, Wang Yao, and Xiaodong Xu. Magnetic control of valley pseudospin in monolayer wse 2. *Nature Physics*, 11(2):148–152, 2015.

[46] Daniele Guerci, Massimo Capone, and Michele Fabrizio. Exciton mott transition revisited. *Physical Review Materials*, 3(5):054605, 2019.

[47] Claus F Klingshirn. *Semiconductor optics*. Springer Science & Business Media, 2012.

[48] Diana Y Qiu, Felipe H Da Jornada, and Steven G Louie. Optical spectrum of mos 2: many-body effects and diversity of exciton states. *Physical review letters*, 111(21):216805, 2013.

[49] Miguel M Ugeda, Aaron J Bradley, Su-Fei Shi, Felipe H Da Jornada, Yi Zhang, Diana Y Qiu, Wei Ruan, Sung-Kwan Mo, Zahid Hussain, Zhi-Xun Shen, et al. Giant bandgap renormalization and excitonic effects in a monolayer transition metal dichalcogenide semiconductor. *Nature materials*, 13(12):1091–1095, 2014.

[50] Thomas Garm Pedersen, Kjeld Pedersen, and Thomas Brun Kriestensen. Optical matrix elements in tight-binding calculations. *Physical Review B*, 63(20):201101, 2001.

[51] Ting Cao, Gang Wang, Wenpeng Han, Huiqi Ye, Chuanrui Zhu, Junren Shi, Qian Niu, Pingheng Tan, Enge Wang, Baoli Liu, et al. Valley-selective circular dichroism of monolayer molybdenum disulphide. *Nature communications*, 3(1):887, 2012.

[52] Kin Fai Mak, Keliang He, Jie Shan, and Tony F Heinz. Control of valley polarization in monolayer mos2 by optical helicity. *Nature nanotechnology*, 7(8):494–498, 2012.

[53] Hualing Zeng, Junfeng Dai, Wang Yao, Di Xiao, and Xiaodong Cui. Valley polarization in mos2 monolayers by optical pumping. *Nature nanotechnology*, 7(8):490–493, 2012.

[54] Hongyi Yu, Gui-Bin Liu, and Wang Yao. Brightened spin-triplet interlayer excitons and optical selection rules in van der waals heterobilayers. *2D Materials*, 5(3):035021, 2018.

[55] Gui-Bin Liu, Di Xiao, Yugui Yao, Xiaodong Xu, and Wang Yao. Electronic structures and theoretical modelling of two-dimensional group-vib transition metal dichalcogenides. *Chemical Society Reviews*, 44(9):2643–2663, 2015.

[56] Matthew Yankowitz, Jiamin Xue, Daniel Cormode, Javier D Sanchez-Yamagishi, K Watanabe, T Taniguchi, Pablo Jarillo-Herrero, Philippe Jacquod, and Brian J LeRoy. Emergence of superlattice dirac points in graphene on hexagonal boron nitride. *Nature physics*, 8(5):382–386, 2012.

[57] Sara Shabani, Dorri Halbertal, Wenjing Wu, Mingxing Chen, Song Liu, James Hone, Wang Yao, Dmitri N Basov, Xiaoyang Zhu, and Abhay N Pasupathy. Deep moiré potentials in twisted transition metal dichalcogenide bilayers. *Nature Physics*, 17(6):720–725, 2021.

[58] Jed Kistner-Morris, Ao Shi, Erfu Liu, Trevor Arp, Farima Farahmand, Takashi Taniguchi, Kenji Watanabe, Vivek Aji, Chun Hung Lui, and Nathaniel Gabor. Electric-field tunable type-i to type-ii band alignment transition in mose2/ws2 heterobilayers. *Nature Communications*, 15(1):4075, 2024.

[59] Hui Fang, Corsin Battaglia, Carlo Carraro, Slavomir Nemsak, Burak Ozdol, Jeong Seuk Kang, Hans A Bechtel, Sujay B Desai, Florian Kronast, Ahmet A Unal, et al. Strong interlayer coupling in van der waals heterostructures built from single-layer chalcogenides. *Proceedings of the National Academy of Sciences*, 111(17):6198–6202, 2014.

[60] Pasqual Rivera, John R Schaibley, Aaron M Jones, Jason S Ross, Sanfeng Wu, Grant Aivazian, Philip Klement, Kyle Seyler, Genevieve Clark, Nirmal J Ghimire, et al. Observation of long-lived interlayer excitons in monolayer mose2–wse2 heterostructures. *Nature communications*, 6(1):6242, 2015.

[61] Zefang Wang, Yi-Hsin Chiu, Kevin Honz, Kin Fai Mak, and Jie Shan. Electrical tuning of interlayer exciton gases in wse2 bilayers. *Nano letters*, 18(1):137–143, 2018.

[62] Alberto Ciarrocchi, Dmitrii Unuchek, Ahmet Avsar, Kenji Watanabe, Takashi Taniguchi, and Andras Kis. Polarization switching and electrical control of interlayer excitons in two-dimensional van der waals heterostructures. *Nature photonics*, 13(2):131–136, 2019.

[63] Chenhao Jin, Eric Yue Ma, Ouri Karni, Emma C Regan, Feng Wang, and Tony F Heinz. Ultrafast dynamics in van der waals heterostructures. *Nature nanotechnology*, 13(11):994–1003, 2018.

[64] Kyle L Seyler, Pasqual Rivera, Hongyi Yu, Nathan P Wilson, Essance L Ray, David G Mandrus, Jiaqiang Yan, Wang Yao, and Xiaodong Xu. Signatures of moiré-trapped valley excitons in mose2/wse2 heterobilayers. *Nature*, 567(7746):66–70, 2019.

[65] Qinghai Tan, Abdullah Rasmita, Zhaowei Zhang, Hongbing Cai, Xiangbin Cai, Xuran Dai, Kenji Watanabe, Takashi Taniguchi, Allan H MacDonald, and

Weibo Gao. Layer-dependent correlated phases in wse2/mos2 moiré superlattice. *Nature Materials*, 22(5):605–611, 2023.

[66] Jonas E Zimmermann, Marleen Axt, Fabian Mooshammer, Philipp Nagler, Christian Schuller, Tobias Korn, Ulrich Hofer, and Gerson Mette. Ultrafast charge-transfer dynamics in twisted mos2/wse2 heterostructures. *ACS nano*, 15(9):14725–14731, 2021.

[67] Xiaoping Hong, Jonghwan Kim, Su-Fei Shi, Yu Zhang, Chenhao Jin, Yinghui Sun, Sefaattin Tongay, Junqiao Wu, Yanfeng Zhang, and Feng Wang. Ultrafast charge transfer in atomically thin mos2/ws2 heterostructures. *Nature nanotechnology*, 9(9):682–686, 2014.

[68] Yongji Gong, Junhao Lin, Xingli Wang, Gang Shi, Sidong Lei, Zhong Lin, Xiaolong Zou, Gonglan Ye, Robert Vajtai, Boris I Yakobson, et al. Vertical and in-plane heterostructures from ws 2/mos 2 monolayers. *Nature materials*, 13(12):1135–1142, 2014.

[69] Michal Baranowski, Alessandro Surrente, L Klopotowski, Joanna M Urban, Nan Zhang, Duncan K Maude, Kamil Wiwatowski, Sebastian Mackowski, Yen-Cheng Kung, Dumitru Dumcenco, et al. Probing the interlayer exciton physics in a mos2/mose2/mos2 van der waals heterostructure. *Nano letters*, 17(10):6360–6365, 2017.

[70] Sukhendu Maity, K Sarkar, and Praveen Kumar. Layered heterostructures based on mos2/mose2 nanosheets deposited on gan substrates for photodetector applications. *ACS Applied Nano Materials*, 6(6):4224–4235, 2023.

[71] Elyse Barré, Ouri Karni, Erfu Liu, Aidan L O'Beirne, Xueqi Chen, Henrique B Ribeiro, Leo Yu, Bumho Kim, Kenji Watanabe, Takashi Taniguchi, et al. Op-

tical absorption of interlayer excitons in transition-metal dichalcogenide heterostructures. *Science*, 376(6591):406–410, 2022.

[72] Ying Jiang, Shula Chen, Weihao Zheng, Biyuan Zheng, and Anlian Pan. Interlayer exciton formation, relaxation, and transport in tmd van der waals heterostructures. *Light: Science & Applications*, 10(1):72, 2021.

[73] Samuel Brem, Christopher Linderalv, Paul Erhart, and Ermin Malic. Tunable phases of moiré excitons in van der waals heterostructures. *Nano letters*, 20(12):8534–8540, 2020.

[74] Chenhao Jin, Emma C Regan, Aiming Yan, M Iqbal Bakti Utama, Danqing Wang, Sihan Zhao, Ying Qin, Sijie Yang, Zhiren Zheng, Shenyang Shi, et al. Observation of moiré excitons in wse2/ws2 heterostructure superlattices. *Nature*, 567(7746):76–80, 2019.

[75] Kha Tran, Galan Moody, Fengcheng Wu, Xiaobo Lu, Junho Choi, Kyounghwan Kim, Amritesh Rai, Daniel A Sanchez, Jiamin Quan, Akshay Singh, et al. Evidence for moiré excitons in van der waals heterostructures. *Nature*, 567(7746):71–75, 2019.

[76] Ouri Karni, Elyse Barré, Vivek Pareek, Johnathan D Georgaras, Michael KL Man, Chakradhar Sahoo, David R Bacon, Xing Zhu, Henrique B Ribeiro, Aidan L O'Beirne, et al. Structure of the moiré exciton captured by imaging its electron and hole. *Nature*, 603(7900):247–252, 2022.

[77] Mohammad Jafar Molaei, Mohammad Younas, and Mashallah Rezakazemi. A comprehensive review on recent advances in two-dimensional (2d) hexagonal boron nitride. *ACS Applied Electronic Materials*, 3(12):5165–5187, 2021.

[78] HH Fang, B Han, C Robert, MA Semina, D Lagarde, E Courtade, T Taniguchi, K Watanabe, T Amand, B Urbaszek, et al. Control of the exciton radiative life-

time in van der waals heterostructures. *Physical review letters*, 123(6):067401, 2019.

[79] Junhao Ni, Quangui Fu, Kostya Ken Ostrikov, Xiaofeng Gu, Haiyan Nan, and Shaoqing Xiao. Status and prospects of ohmic contacts on two-dimensional semiconductors. *Nanotechnology*, 33(6):062005, 2021.

[80] Kin Fai Mak, Keliang He, Changgu Lee, Gwan Hyoung Lee, James Hone, Tony F Heinz, and Jie Shan. Tightly bound trions in monolayer mos2. *Nature materials*, 12(3):207–211, 2013.

[81] Jason S Ross, Sanfeng Wu, Hongyi Yu, Nirmal J Ghimire, Aaron M Jones, Grant Aivazian, Jiaqiang Yan, David G Mandrus, Di Xiao, Wang Yao, et al. Electrical control of neutral and charged excitons in a monolayer semiconductor. *Nature communications*, 4(1):1474, 2013.

[82] Meinrad Sidler, Patrick Back, Ovidiu Cotlet, Ajit Srivastava, Thomas Fink, Martin Kroner, Eugene Demler, and Atac Imamoglu. Fermi polaron-polaritons in charge-tunable atomically thin semiconductors. *Nature Physics*, 13(3):255–261, 2017.

[83] Yilei Li, Jonathan Ludwig, Tony Low, Alexey Chernikov, Xu Cui, Ghidewon Arefe, Young Duck Kim, Arend M Van Der Zande, Albert Rigosi, Heather M Hill, et al. Valley splitting and polarization by the zeeman effect in monolayer mose 2. *Physical review letters*, 113(26):266804, 2014.

[84] Ajit Srivastava, Meinrad Sidler, Adrien V Allain, Dominik S Lembke, Andras Kis, and Atac Imamoğlu. Valley zeeman effect in elementary optical excitations of monolayer wse 2. *Nature Physics*, 11(2):141–147, 2015.

[85] David MacNeill, Colin Heikes, Kin Fai Mak, Zachary Anderson, Andor Kormányos, Viktor Zólyomi, Jiwoong Park, and Daniel C Ralph. Breaking

of valley degeneracy by magnetic field in monolayer mose 2. *Physical review letters*, 114(3):037401, 2015.

[86] Cedric Robert, Hanan Dery, Lei Ren, Dinh Van Tuan, Emmanuel Courtade, Min Yang, Bernhard Urbaszek, Delphine Lagarde, Kenji Watanabe, Takashi Taniguchi, et al. Measurement of conduction and valence bands g-factors in a transition metal dichalcogenide monolayer. *Physical Review Letters*, 126(6):067403, 2021.

[87] Thorsten Deilmann, Peter Krüger, and Michael Rohlfing. Ab initio studies of exciton g factors: monolayer transition metal dichalcogenides in magnetic fields. *Physical review letters*, 124(22):226402, 2020.

[88] Tomasz Woźniak, Paulo E Faria Junior, Gotthard Seifert, Andrey Chaves, and Jens Kunstmann. Exciton g factors of van der waals heterostructures from first-principles calculations. *Physical Review B*, 101(23):235408, 2020.

[89] Jonathan Förste, Nikita V Tepliakov, Stanislav Yu Kruchinin, Jessica Lindlau, Victor Funk, Michael Förg, Kenji Watanabe, Takashi Taniguchi, Anvar S Baimuratov, and Alexander Högele. Exciton g-factors in monolayer and bilayer wse2 from experiment and theory. *Nature communications*, 11(1):4539, 2020.

[90] Fengyuan Xuan and Su Ying Quek. Valley zeeman effect and landau levels in two-dimensional transition metal dichalcogenides. *Physical Review Research*, 2(3):033256, 2020.

[91] Dmitrii Unuchek, Alberto Ciarrocchi, Ahmet Avsar, Zhe Sun, Kenji Watanabe, Takashi Taniguchi, and Andras Kis. Valley-polarized exciton currents in a van der waals heterostructure. *Nature nanotechnology*, 14(12):1104–1109, 2019.

[92] Daniel N Shanks, Fateme Mahdikhanysarvejahany, Trevor G Stanfill, Michael R Koehler, David G Mandrus, Takashi Taniguchi, Kenji Watanabe, Brian J

LeRoy, and John R Schaibley. Interlayer exciton diode and transistor. *Nano Letters*, 22(16):6599–6605, 2022.

[93] Dmitrii Unuchek, Alberto Ciarrocchi, Ahmet Avsar, Kenji Watanabe, Takashi Taniguchi, and Andras Kis. Room-temperature electrical control of exciton flux in a van der waals heterostructure. *Nature*, 560(7718):340–344, 2018.

[94] Yuanda Liu, Kévin Dini, Qinghai Tan, Timothy Liew, Kostya S Novoselov, and Weibo Gao. Electrically controllable router of interlayer excitons. *Science advances*, 6(41):eaba1830, 2020.

[95] Philipp Nagler, Mariana V Ballottin, Anatolie A Mitioglu, Fabian Mooshammer, Nicola Paradiso, Christoph Strunk, Rupert Huber, Alexey Chernikov, Peter CM Christianen, Christian Schüller, et al. Giant magnetic splitting inducing near-unity valley polarization in van der waals heterostructures. *Nature communications*, 8(1):1551, 2017.

[96] Yu Zhang, Yuyu Yao, Marshet Getaye Sendeku, Lei Yin, Xueying Zhan, Feng Wang, Zhenxing Wang, and Jun He. Recent progress in cvd growth of 2d transition metal dichalcogenides and related heterostructures. *Advanced materials*, 31(41):1901694, 2019.

[97] Dingyi Shen, Yejun Jin, Zucheng Zhang, Rong Song, Miaomiao Liu, Wei Li, Xin Li, Ruixia Wu, Bo Li, Jia Li, et al. Recent advances in spin-coating precursor mediated chemical vapor deposition of two-dimensional transition metal dichalcogenides. *Precision Chemistry*, 2(7):282–299, 2024.

[98] PJ Zomer, MHD Guimarães, JC Brant, N Tombros, and BJ Van Wees. Fast pick up technique for high quality heterostructures of bilayer graphene and hexagonal boron nitride. *Applied Physics Letters*, 105(1), 2014.

[99] Kyounghwan Kim, Matthew Yankowitz, Babak Fallahazad, Sangwoo Kang, Hema CP Movva, Shengqiang Huang, Stefano Larentis, Chris M Corbet, Takashi Taniguchi, Kenji Watanabe, et al. van der waals heterostructures with high accuracy rotational alignment. *Nano letters*, 16(3):1989–1995, 2016.

[100] Kyle DiCamillo, Sergiy Krylyuk, Wendy Shi, Albert Davydov, and Makarand Paranjape. Automated mechanical exfoliation of mos 2 and mote 2 layers for two-dimensional materials applications. *IEEE Transactions on Nanotechnology*, 18:144–148, 2018.

[101] Min Su Kim, Seok Joon Yun, Yongjun Lee, Changwon Seo, Gang Hee Han, Ki Kang Kim, Young Hee Lee, and Jeongyong Kim. Biexciton emission from edges and grain boundaries of triangular ws2 monolayers. *ACS nano*, 10(2):2399–2405, 2016.

[102] Luka Matej Devenica, Zach Hadjri, Jan Kumlin, Runtong Li, Weijie Li, Daniel Suarez Forrero, Valeria Vento, Nicolas Ubrig, Song Liu, James Hone, et al. Signatures of collective photon emission and ferroelectric ordering of excitons near their mott insulating state in a wse _2/ws _2 heterobilayer. *arXiv preprint arXiv:2502.19490*, 2025.

[103] Camille Lagoin, Stephan Suffit, Kirk Baldwin, Loren Pfeiffer, and François Dubin. Mott insulator of strongly interacting two-dimensional semiconductor excitons. *Nature Physics*, 18(2):149–153, 2022.

[104] Richen Xiong, Jacob H Nie, Samuel L Brantly, Patrick Hays, Renee Sailus, Kenji Watanabe, Takashi Taniguchi, Sefaattin Tongay, and Chenhao Jin. Correlated insulator of excitons in wse2/ws2 moiré superlattices. *Science*, 380(6647):860–864, 2023.

[105] Heonjoon Park, Jiayi Zhu, Xi Wang, Yingqi Wang, William Holtzmann, Takashi

Taniguchi, Kenji Watanabe, Jiaqiang Yan, Liang Fu, Ting Cao, et al. Dipole ladders with large hubbard interaction in a moiré exciton lattice. *Nature Physics*, 19(9):1286–1292, 2023.

[106] Xi Wang, Xiaowei Zhang, Jiayi Zhu, Heonjoon Park, Yingqi Wang, Chong Wang, William G Holtzmann, Takashi Taniguchi, Kenji Watanabe, Jiaqiang Yan, et al. Intercell moiré exciton complexes in electron lattices. *Nature Materials*, 22(5):599–604, 2023.

[107] Beini Gao, Daniel G Suárez-Forero, Supratik Sarkar, Tsung-Sheng Huang, Deric Session, Mahmoud Jalali Mehrabad, Ruihao Ni, Ming Xie, Pranshoo Upadhyay, Jonathan Vannucci, et al. Excitonic mott insulator in a bose-fermi-hubbard system of moiré ws2/wse2 heterobilayer. *Nature Communications*, 15(1):2305, 2024.

[108] Zhen Lian, Yuze Meng, Lei Ma, Indrajit Maity, Li Yan, Qiran Wu, Xiong Huang, Dongxue Chen, Xiaotong Chen, Xinyue Chen, et al. Valley-polarized excitonic mott insulator in ws2/wse2 moiré superlattice. *Nature Physics*, 20(1):34–39, 2024.

[109] Hongyuan Li, Shaowei Li, Emma C Regan, Danqing Wang, Wenyu Zhao, Salman Kahn, Kentaro Yumigeta, Mark Blei, Takashi Taniguchi, Kenji Watanabe, et al. Imaging two-dimensional generalized wigner crystals. *Nature*, 597(7878):650–654, 2021.

[110] Weijie Li, Xin Lu, Sudipta Dubey, Luka Devenica, and Ajit Srivastava. Dipolar interactions between localized interlayer excitons in van der waals heterostructures. *Nature materials*, 19(6):624–629, 2020.

[111] Xi Wang, Jiayi Zhu, Kyle L Seyler, Pasqual Rivera, Huiyuan Zheng, Yingqi Wang, Minhao He, Takashi Taniguchi, Kenji Watanabe, Jiaqiang Yan,

et al. Moiré trions in mose2/wse2 heterobilayers. *Nature Nanotechnology*, 16(11):1208–1213, 2021.

[112] Pranshoo Upadhyay, Daniel G Suárez-Forero, Tsung-Sheng Huang, Mahmoud Jalali Mehrabad, Beini Gao, Supratik Sarkar, Deric Session, Kenji Watanabe, Takashi Taniguchi, You Zhou, et al. Giant enhancement of exciton diffusion near an electronic mott insulator. *arXiv preprint arXiv:2409.18357*, 2024.

[113] Li Yan, Lei Ma, Yuze Meng, Chengxin Xiao, Bo Chen, Qiran Wu, Jingyuan Cui, Qingrui Cao, Rounak Banerjee, Takashi Taniguchi, et al. Anomalously enhanced diffusivity of moir\'e excitons via manipulating the interplay with correlated electrons. *arXiv preprint arXiv:2410.11734*, 2024.

[114] Niclas Götting, Frederik Lohof, and Christopher Gies. Moiré-bose-hubbard model for interlayer excitons in twisted transition metal dichalcogenide heterostructures. *Physical Review B*, 105(16):165419, 2022.

[115] Jan Kumlin, Ajit Srivastava, and Thomas Pohl. Superradiance of strongly interacting dipolar excitons in moir\'e quantum materials. *arXiv preprint arXiv:2410.08891*, 2024.

[116] Alejandro R-P Montblanch, Dhiren M Kara, Ioannis Paradisanos, Carola M Purser, Matthew SG Feuer, Evgeny M Alexeev, Lucio Stefan, Ying Qin, Mark Blei, Gang Wang, et al. Confinement of long-lived interlayer excitons in ws2/wse2 heterostructures. *Communications Physics*, 4(1):119, 2021.

[117] Bastian Miller, Alexander Steinhoff, Borja Pano, Julian Klein, Frank Jahnke, Alexander Holleitner, and Ursula Wurstbauer. Long-lived direct and indirect interlayer excitons in van der waals heterostructures. *Nano letters*, 17(9):5229–5237, 2017.

[118] Luis A Jauregui, Andrew Y Joe, Kateryna Pistunova, Dominik S Wild, Alexander A High, You Zhou, Giovanni Scuri, Kristiaan De Greve, Andrey Sushko, Che-Hang Yu, et al. Electrical control of interlayer exciton dynamics in atomically thin heterostructures. *Science*, 366(6467):870–875, 2019.

[119] Junho Choi, Matthias Florian, Alexander Steinhoff, Daniel Erben, Kha Tran, Dong Seob Kim, Liuyang Sun, Jiamin Quan, Robert Claassen, Somak Majumder, et al. Twist angle-dependent interlayer exciton lifetimes in van der waals heterostructures. *Physical Review Letters*, 126(4):047401, 2021.

[120] Galan Moody, John Schaibley, and Xiaodong Xu. Exciton dynamics in monolayer transition metal dichalcogenides. *Journal of the Optical Society of America B*, 33(7):C39–C49, 2016.

[121] Xiao-Xiao Zhang, Yumeng You, Shu Yang Frank Zhao, and Tony F Heinz. Experimental evidence for dark excitons in monolayer wse 2. *Physical review letters*, 115(25):257403, 2015.

[122] Neil R Wilson, Paul V Nguyen, Kyle Seyler, Pasqual Rivera, Alexander J Marsden, Zachary PL Laker, Gabriel C Constantinescu, Viktor Kandyba, Alexei Barinov, Nicholas DM Hine, et al. Determination of band offsets, hybridization, and exciton binding in 2d semiconductor heterostructures. *Science advances*, 3(2):e1601832, 2017.

[123] Dawei Zhang, Peggy Schoenherr, Pankaj Sharma, and Jan Seidel. Ferroelectric order in van der waals layered materials. *Nature Reviews Materials*, 8(1):25–40, 2023.

[124] Michel Gross and Serge Haroche. Superradiance: An essay on the theory of collective spontaneous emission. *Physics reports*, 93(5):301–396, 1982.

[125] Weijie Li, Zach Hadjri, Luka M Devenica, Jin Zhang, Song Liu, James Hone, Kenji Watanabe, Takashi Taniguchi, Angel Rubio, and Ajit Srivastava. Quadrupolar–dipolar excitonic transition in a tunnel-coupled van der waals heterotrilayer. *Nature Materials*, 22(12):1478–1484, 2023.

[126] Leo Yu, Kateryna Pistunova, Jenny Hu, Kenji Watanabe, Takashi Taniguchi, and Tony F Heinz. Observation of quadrupolar and dipolar excitons in a semiconductor heterotrilayer. *Nature materials*, 22(12):1485–1491, 2023.

[127] Qingjun Tong, Mingxing Chen, Feiping Xiao, Hongyi Yu, and Wang Yao. Interferences of electrostatic moiré potentials and bichromatic superlattices of electrons and excitons in transition metal dichalcogenides. *2D Materials*, 8(2):025007, 2020.

[128] Yevgeny Slobodkin, Yotam Mazuz-Harpaz, Sivan Refaely-Abramson, Snir Gazit, Hadar Steinberg, and Ronen Rapaport. Quantum phase transitions of trilayer excitons in atomically thin heterostructures. *Physical Review Letters*, 125(25):255301, 2020.

[129] Ss Schmitt-Rink, DS Chemla, and David AB Miller. Theory of transient excitonic optical nonlinearities in semiconductor quantum-well structures. *Physical Review B*, 32(10):6601, 1985.

[130] G Rochat, C Ciuti, V Savona, C Piermarocchi, A Quattropani, and P Schwendimann. Excitonic bloch equations for a two-dimensional system of interacting excitons. *Physical Review B*, 61(20):13856, 2000.

[131] Jie Gu, Valentin Walther, Lutz Waldecker, Daniel Rhodes, Archana Raja, James C Hone, Tony F Heinz, Stéphane Kéna-Cohen, Thomas Pohl, and Vinod M Menon. Enhanced nonlinear interaction of polaritons via excitonic rydberg states in monolayer wse2. *Nature communications*, 12(1):2269, 2021.

[132] Long Zhang, Fengcheng Wu, Shaocong Hou, Zhe Zhang, Yu-Hsun Chou, Kenji Watanabe, Takashi Taniguchi, Stephen R Forrest, and Hui Deng. Van der waals heterostructure polaritons with moiré-induced nonlinearity. *Nature*, 591(7848):61–65, 2021.

[133] Li Bing Tan, Ovidiu Cotlet, Andrea Bergschneider, Richard Schmidt, Patrick Back, Yuya Shimazaki, Martin Kroner, and Ataç İmamoğlu. Interacting polaron-polaritons. *Physical Review X*, 10(2):021011, 2020.

[134] M Sammon and Boris I Shklovskii. Attraction of indirect excitons in van der waals heterostructures with three semiconducting layers. *Physical Review B*, 99(16):165403, 2019.

[135] Fabian Pichler, Mohammad Hafezi, and Michael Knap. Purely electronic model for exciton-polaron formation in moir\'e heterostructures. *arXiv preprint arXiv:2503.07712*, 2025.

[136] Tsung-Sheng Huang, Yu-Xin Wang, Yan-Qi Wang, Darrick Chang, Mohammad Hafezi, and Andrey Grankin. Collective optical properties of moir\'e excitons. *arXiv preprint arXiv:2407.19611*, 2024.

[137] Natasha Kiper, Haydn S Adlong, Arthur Christianen, Martin Kroner, Kenji Watanabe, Takashi Taniguchi, and Atac İmamoğlu. Confined trions and mott-wigner states in a purely electrostatic moiré potential. *Physical Review X*, 15(1):011049, 2025.

[138] Feng-Ren Fan, Tixuan Tan, Chengxin Xiao, and Wang Yao. Magnetic and nematic order of bose-fermi mixtures in moir\'e superlattices of 2d semiconductors. *arXiv preprint arXiv:2407.10767*, 2024.

[139] Fateme Mahdikhanysarvejahany, Daniel N Shanks, Matthew Klein, Qian Wang, Michael R Koehler, David G Mandrus, Takashi Taniguchi, Kenji Watanabe,

Oliver LA Monti, Brian J LeRoy, et al. Localized interlayer excitons in mose2–wse2 heterostructures without a moiré potential. *Nature communications*, 13(1):5354, 2022.

[140] Fa-Yueh Wu. The potts model. *Reviews of modern physics*, 54(1):235, 1982.

[141] Honglie Ning and Nuh Gedik. Visualizing the moiré of moiré. *Nature Materials*, 23(12):1606–1607, 2024.

[142] Steven J Byrnes. Multilayer optical calculations. *arXiv preprint arXiv:1603.02720*, 2016.

[143] Georg Kresse and Jürgen Furthmüller. Efficient iterative schemes for ab initio total-energy calculations using a plane-wave basis set. *Physical review B*, 54(16):11169, 1996.

[144] John P Perdew, Kieron Burke, and Matthias Ernzerhof. Generalized gradient approximation made simple. *Physical review letters*, 77(18):3865, 1996.

[145] Jiří Klimeš, David R Bowler, and Angelos Michaelides. Van der waals density functionals applied to solids. *Physical Review B—Condensed Matter and Materials Physics*, 83(19):195131, 2011.